Department of Applied Physics

Impact-Parameter Convergent Close-Coupling Approach to Antiproton-Atom Collisions

Ilkhom Abdurakhmanov

This thesis is presented for the Degree of
Doctor of Philosophy
of
Curtin University

December, 2011

Declaration

To the best of my knowledge and belief this thesis contains no material previously published by any other person except where due acknowledgment has been made.

This thesis contains no material which has been accepted for the award of any other degree or diploma in any university.

Signature

date

Contents

Summary

This thesis is devoted to extension of the convergent close-coupling (CCC) method to heavy projectiles and its application to the theoretical studies of antiproton scattering on the hydrogen and helium targets.

The thesis is organized in the following way:

In the Introduction (Chapter 1) the motivation for the study and the current status of antiproton scattering on hydrogen and helium are presented. Other theoretical methods that previously have been applied to these problems are reviewed and their limitations are indicated. The extension of the fully quantum-mechanical CCC method to ion-atom collisions is presented in Chapter 2. The derivations of the momentum-space coupled-channel Lippmann-Schwinger integral equations from the exact Schrödinger equation is given in detail. Transition matrix elements are derived in momentum-space. In Chapter 3 a direct method for solving multi-dimensional Lippmann-Schwinger integral equations without recourse to partial-wave expansion or any other transformation scheme will be described. A direct method has been applied to the antiproton-hydrogen as well as to the proton-hydrogen collisions. In Chapter 4 we solve the full multichannel problem by transforming the coupled-channel integral equations into the impact-parameter representation. The scattering amplitude necessary to calculate the differential and total cross sections will be derived from the transition matrix elements. The results of the CCC calculations for antiproton scattering from

atomic hydrogen and helium are presented and compared with available experimental data and the results of other calculations in Chapter 5 and Chapter 6, respectively. Finally, in Chapter 7, we draw conclusions arising from this work and indicate future directions for the research.

Main results of this work

- The convergent close-coupling method has been extended to heavy projectiles and applied to antiproton scattering on atomic hydrogen and helium.
- For the first time, the relative motion of the heavy particles in antiproton collisions with atomic hydrogen and helium has been treated quantum-mechanically.
- A direct method to solving the three-dimensional momentum-space coupled-channel Lippmann-Schwinger integral equations has been developed.
- A scheme for transforming the three-dimensional Lippmann-Schwinger integral equations into the impact-parameter representation has been developed. The fully off-shell transition matrix elements in the impact-parameter space have been derived.
- For the first time, the fully quantum mechanical calculations of the cross sections for all the major channels of interest in antiproton collisions with hydrogen and helium have been performed over a wide range of scattering energies.
- The total ionization cross sections for the H target has been calculated. The results are in excellent agreement with the available experiment. An overall agreement of the present results with the semiclassical calculations

by other groups has practically confirmed the validity of the semiclassical approximation imposed on the relative heavy particle motion.

- The total cross section for the He single ionization has been calculated using frozen-core (FC) and multi-configuration (MC) approximation for the target. As opposed to rather sophisticated and rigorous MC calculations the FC results agree with the experimental data at a wider energy range.

- For the first time, based on the fully quantum-mechanical treatment of the problem the triple differential cross sections have been calculated for antiproton scattering on both H and He.

- The $\bar{p}-H$ results for the various differential ionization cross sections agree reasonably well with the results of the semiclassical close-coupling and the continuum-distorted-wave-eikonal-initial-state (CDW-EIS) approaches, particularly at high energies.

- The longitudinal ejected electron and recoil-ion momentum distributions for the single ionization of helium have been calculated. The results are in good agreement with the available experimental data.

List of publications

Five peer-reviewed papers have been published on the results presented in this thesis. They are listed below in chronological order.

- A. S. Kadyrov, I. B. Abdurakhmanov, I. Bray, and A. T. Stelbovics, **Three-dimensional integral-equation approach to proton- and antiproton-hydrogen collisions.** Physical Review A **80**, 022704 (2009).

- A. S. Kadyrov, I. B. Abdurakhmanov, R. Utamuratov, A. V. Lugovskoy, D. V. Fursa, I. Bray, and A. T. Stelbovics, **convergent close-coupling approach to positron and antiproton collisions with atoms.** Journal of Physics: Conference Series **262**, 012028 (2011).

- I. B. Abdurakhmanov, A. S. Kadyrov, I. Bray and A. T. Stelbovics, **Coupled-channel integral-equation approach to antiproton-hydrogen collisions.** Journal of Physics B: Atomic, Molecular and Optical Physics **44**, 075204 (2011).

- I. B. Abdurakhmanov, A. S. Kadyrov, I. Bray and A. T. Stelbovics, **Differential ionization in antiproton-hydrogen collisions within the convergent-close-coupling approach.** Journal of Physics B: Atomic, Molecular and Optical Physics **44**, 165203 (2011).

- I. B. Abdurakhmanov, A. S. Kadyrov, I. Bray and A. T. Stelbovics, **Convergent close-coupling calculations of single ionization of helium by antiproton impact.** Physical Review A, **84**, 062708 (2011).

Acknowledgments

First of all I owe my deepest gratitude to my supervisor, Dr Alisher Kadyrov for proposing the interesting topic to me as well as for his supervision during my time as a PhD student. Without his constant support and encouragement this thesis would not have been possible.

Also, I am deeply grateful to my co-supervisor Professor Igor Bray for his invaluable advices and immense expertise in the field. I also thank Associate Professor Dmitry Fursa for sharing his codes with me and contributing to this research. I am indebted to Professor Andris Stelbovics for his assistance and constructive advices during the project.

I would like to thank all members of the Institute of Theoretical Physics for the pleasant atmosphere and for all the discussions on physics as well as on many other topics which helped me to broaden my horizon.

Furthermore, I would like to acknowledge the open, friendly and stimulating correspondences with Prof. Helge Knudsen, Prof. Michael Pindzola and Dr habil. Alexander Voitkiv including also the exchange of published, as well as unpublished data.

I am very much obliged to the Curtin University International Postgraduate Research Scholarship and the Centre of Excellence for Matter-antimatter Studies for the financial support.

I would like to thank my parents for their long-lasting support from the very first moment. Finally, my love goes to my wife Gulnoza and to my son Komron who was born during the time of my PhD project.

Chapter 1

Introduction

Studying various scattering processes has led to many major discoveries in physics, the list of which starts with the famous Rutherford scattering phenomena observed in collisions of alpha particles with gold nuclei in early 1911 [1]. These discoveries gave birth to a vast number of practical applications that we directly use or encounter in our daily life. Most of modern diagnostic equipment in medicine, analysing and designing tools in material science, many aspects of the lighting industry, video projection technologies in cinematography and many others can complement this list. However, some discoveries, despite being significant, have no immediate direct applications. They serve as an intermediary for subsequent discoveries.

Ion-atom collisions play a significant role in scattering studies. They have evolved from a subject of fundamental research to a subject with significant importance for various applications. Accurate knowledge of all involved processes, like ionization and excitation of target atoms, transfer of electrons between the target and the projectile, and the energy loss of the projectile while traversing the target medium, is essential to many other subjects, namely the physics of the atmosphere, astrophysics, radiation physics, quantum chemistry, biophysics, and even medicine, where it is used for precise construction and design of cancer

therapy equipment employing ion-atom collisions.

We have developed a new fully quantum mechanical approach to describing ion collisions with atoms. From the theoretical point of view the simplest reaction of this kind is antiproton-hydrogen collisions. In this thesis we present full details of our approach and its application to antiproton scattering on hydrogen and helium targets. Furthermore, throughout the text we give a clear scheme for the extension of the method to consider more complex collision systems.

We have a number of reasons for choosing the antiproton as a projectile. Since the antiproton has a negative charge, in contrast to the collisions with protons, there is no electron-transfer channel. Instead there is an antiprotonic atom formation in case of helium [2]. Presently antiprotons can be decelerated down to low keV energies. Therefore, antiproton scattering studies are of a particular importance in this energy region. Above the keV region formation of protonium or other stable system containing antiproton is negligible [2, 3]. Consequently, in this region antiproton collisions with atoms are essentially a single-centre problem. This fact greatly simplifies theoretical calculations and makes the reaction with participation of antiprotons an ideal ground for testing various theoretical models without complications associated with two-centre problems. In addition, owing to the unique properties of antiprotons (i) effects of different masses can be studied if the obtained results are compared with the relevant data for electron scattering; (ii) if compared against the proton scattering data effects occurring due to the difference in the charge sign can be investigated.

Experimental and theoretical progress in the field of antiproton-impact-induced ionization of atoms and molecules has very recently been reviewed by Kirchner and Knudsen [4]. Antiproton impact ionization of H and He has

been studied both experimentally and theoretically. The amount exceeds the number of experimental investigations since the production of antiproton beams suitable for scattering experiments is very challenging. We will highlight the current situation of studies of antiproton scattering for both targets separately.

1.1 The hydrogen target

In antiproton scattering studies atomic hydrogen plays an important role, since in such collisions there are no complications for the theory due to the incomplete knowledge of the static-target wave function or the dynamic correlations among the target electrons as in the case of multielectron targets. Therefore, this system is an ideal starting point for testing new theoretical models. Whereas a similar three-body Coulomb scattering problem, but with electron as a projectile, has a complete practical solution [5–7], collisions of heavy projectiles with atomic hydrogen still present significant challenges.

In antiproton-hydrogen collisions, depending on the impact energy of the projectile, various processes can occur during the interaction of the antiproton and atomic hydrogen. At energies of the projectile lower than a certain value, only the elastic channel is open. As the energy increases, various inelastic channels become accessible, including excitation and ionization of the target. Above the ionization threshold, which is at 13.6 eV in the laboratory system of reference, the projectile is able to ionize the target. The ionization process itself can follow two different channels: (i) in the final state all three particles fly away from each other; (ii) the target electron flies away while the antiproton forms a bound state with the target proton which is called protonium. The latter channel is significant only at sufficiently low energies [3]. For this energy region studies are limited to only a few publications [3, 8–10]. This is due to the failure

at very low energies of the semiclassical approximation which is usually applied to the relative motion of heavy particles in ion-atom collision studies.

Assuming that above the energy of 1 keV the semiclassical approximation mentioned above is applicable and ignoring the possibility of protonium formation a considerable number of theoretical calculations [3, 8, 9, 11–25] have been performed for the elastic, excitation and ionization cross sections. As far as the total ionization is concerned the situation is unclear at low incident projectile energies. While most of the existing theories are in a good agreement with experimental measurements [26] at high energies there are still questions at low energies. In particular, none of the known approaches appears to be capable of describing ionization near the threshold in accordance with the Fermi-Teller limit [3].

In contrast to the investigation of the total cross section, studying differential cross sections in general can shed more light on the collision dynamics. For example, a seemingly settled question about the role of the heavy particle interaction in ion-atom collisions has reemerged [27] due to recent experimental measuments of differential ionization [28, 29]. The triply differential cross sections (TDCS) reveal the collision dynamics at the most detailed level and, therefore, their exploration should provide the strictest test of theory. Other differential cross sections differential in electron and/or projectile variables are also of major importance as they are very sensitive to the collision dynamics. However, most available theories of antiproton-hydrogen scattering do not provide a kinematically complete picture of the process on a wide range of collision energies. Very few of them are capable [23–25, 30–35]. Unfortunately, validity of these results can not be directly verified due to the absence of experimental data. As different methods lead to somewhat different differential ionization cross sections, more experimental support would be highly beneficial.

1.2 The helium target

Atomic helium is attractive to theorists since it is the simplest target where one can investigate the electron correlation effects on the probabilities of processes occurring in collisions with antiprotons. In the development of early approaches it was assumed that single particle processes, like single atomic excitation and ionization, do not involve electron-electron correlations. Consequently, many approaches employing the independent electron model of the target have been developed. However, recent rather complicated studies suggest the importance of correlation effects. Additionally, since the incoming antiproton is not involved in the spin-orbit interaction with the target, the total spin of He is conserved during the collision. This fact greatly simplifies the theoretical modeling. Specifically, for the problem description only the spatial part of the He wave function may be used. Its spin-part has no effect on the collision dynamics whatsoever, and thus, can be disregarded. From the experimental perspective among collisions involving the incident antiproton, investigations of antiproton-helium scattering is less difficult because it is relatively easy to create a target of helium. For this reason, besides the measurements of the total ionization cross section over a quite wide energy range [36–38], there is also an experiment on differential ionization [39].

From the theoretical point of view the antiproton-helium scattering system is a quantum-mechanical four-body problem, which cannot be solved analytically. At sufficiently high energies simple first-order perturbation methods, namely, the first Born approximation (FBA) and continuum distorted-wave eikonal initial-state (CDW-EIS) approaches can produce reliable total ionisation cross sections. At lower impact energies various nonperturbative theoretical approaches have been applied. Depending on the energy range there are some discrepancies be-

tween the various theoretical approaches, and with experiment, and it is still unclear if there is something missing in the theory that is responsible for remaining discrepancies.

There are several approximations that may be applied to the antiproton-helium collision problem. First, the antiproton motion can be treated classically by means of straight line trajectories. This approximation is well-accepted in ion-atom collisions and its ability to reproduce correct integrated cross sections for all processes involved in antiproton-hydrogen collisions above 1 keV has recently been demonstrated [40]. However, it is still unclear if this approximation is equally satisfactory for calculation of differential cross sections over a wide incident energy range. A second approximation is applied in order to avoid complications that arise from a complete description of He wave functions. Ideally, the antiproton-helium scattering must be treated as a four-body problem and the target wave functions should be obtained by diagonalizing a full three-body target Hamiltonian. The transition amplitudes in the resulting coupled equations would carry indices describing quantum states of each of the target electrons. This is far from practical even with present-day computational resources. For this reason an often used approximation is to treat helium as a hydrogen-like target, and consequently consider only single ionization processes. These can be classified into two categories. The earliest ones employed the independent electron approximation in the description of He assuming that the single-electron process can be described with sufficient accuracy even without the inclusion of electron correlation effects [41–44]. More complex approaches [24, 43, 45, 46] assumed the static correlation of the outer electron with the inner one constrained in the 1s orbital (frozen-core approximation), yielded significantly different results especially at low energies. This by itself already clearly indicated the importance of electron correlation effects. With further advancement of computing

technology new sophisticated calculations by Guan and Bartschat [16], Igarashi et al. [43], Foster et al. [47] and Pindzola et al. [48] became available where multiple configurations were allowed for both the target electrons. This modification improved the He wave functions and yielded an ionization potential of the ground state which is much closer to its experimental value. The resultant ionization cross sections also significantly changed from the values obtained in the frozen-core approximation. We also adopt the multiconfiguration model of the He target. The idea of including double-continuum states in the description of He structure is not feasible since in that case one runs into the problem of mixing of single and double ionization channels. This issue was addressed in [49] where the effects of double ionization channels on the single ionization cross section were investigated.

Lastly, the accuracy of model results might also depend on the way how the ionization states are represented. Most of the existing nonperturbative models use different bases of pseudostates to represent the continuum. Some of them allow one to increase the size of the employed basis to an arbitrary large number so that one can check the convergence of the final results. However, the diagonalization of the target Hamiltonian using some bases, like the Slater one, leads to linear dependence problems if the basis is too large, resulting in an ill conditioned set of He coupled equations. This prevents demonstrable convergence of the final results.

In the following section, a brief review of different methods used in theoretical modelling of ion-atom collisions is given for the example of antiproton scattering on atomic hydrogen. Most of the listed approaches have been applied to antiproton-helium collisions as well, since the scattering equations remain the same regardless of the target. The only modification is applied to the description of the He target. We have already addressed different structure models of

atomic helium.

1.3 Overview of existing antiproton-hydrogen scattering theories

All theoretical models developed so far can be classified into three categories: classical-trajectory Monte-Carlo (CTMC) models, first order quantum-mechanical perturbation models, and nonperturbative methods which are based on the solution of the approximate time-dependent Schrödinger equation (TDSE) using either close-coupling or grid based schemes. The TDSE which is the usual starting point for the nonperturbative methods is derived from the exact stationary Schrödinger equation as a result of the semiclassical approximation (SCA) [4]. In the SCA, the heavy-particle motion assumed to be along a straight-line trajectory $\boldsymbol{R}(t) = \boldsymbol{b} + \boldsymbol{v}_p t$, where $\boldsymbol{b}$ is the impact parameter and $\boldsymbol{v}_p$ is the constant projectile velocity. Experimental study on the total ionization of hydrogen by antiproton impact has been carried out by Knudsen et al. [26]. Apart from the CTMC, most of the calculations agree well with the experimental results at high energies. However, there still exists some discrepancies among different theories at low energies where no measurements are available.

1.3.1 Classical Trajectory Monte-Carlo technique

Cohen [8, 50], Schultz et al. [3], and Olson et al. [51] utilized the classical trajectory Monte-Carlo (CTMC) technique to study antiproton- and proton-hydrogen scattering. This method starts with Hamilton's equations of motion for the three-body system consisting of the target nucleus, an electron initially bound to the target, and the projectile. A large ensemble of projectile-target configurations is sampled in order to simulate the collision. It generally consists

of three steps: (i) initialization of the projectile-target configuration; (ii) calculation of the classical trajectories; and (iii) a final-state test for reaction. In the first step the active electron is randomly initialized in its orbit according to a micro-canonical distribution, so that its position and momentum on average initiate the quantum mechanical position and momentum distributions. The impact parameter is randomly distributed between 0 and some $b_{\max}$. In the second step, $6N$ coupled differential equations, representing the Hamiltonian equations of motion for the N bodies in the collision, are integrated numerically from some large initial projectile-target separation, through the collision, and continuing to some large final separation. After integration, the relative energies between the particles are found and what reactions, if any, have occurred is established. The main advantage of this method is that it can describe dynamic effects occurring during the collision and give a fully kinematic picture of the scattering. For a detailed description of the method interested reader may refer to the work of Olson and Salop [52].

Using this method Schultz et al. [3], Cohen [8] gave estimations for ionization and protonium formation processes. Their studies show that the protonium formation becomes significant only at energies below the ionization threshold $E < I$ ($I = 13.6$ eV). Cohen [8] also reported that the protonium can be formed only in very high orbitals. Consequently, the fully quantal calculations are expected to be complicated. On the other hand, it is not certain if the CTMC method is accurate enough even to estimate the possibility of protonium formation. The CTMC predictions for the total ionization underestimate the experiment [26] at high energies.

1.3.2 First order perturbation methods: The Born and distorted wave approximations

The first theoretical description of the antiproton-hydrogen scattering was introduced by Bates and Griffing [12] in early 1954. The Born method is based on the assumption that the wavefunction for the scattering system can be expanded in a rapidly convergent series. This approximation uses plane-waves to describe the projectile and Coulomb waves for the description of product particles. The Born approximation is a good approach when the scattering potential is relatively small compared to the incident energy, and thus is applicable only at high energies. The method fails as far as the study of mass or charge effects are concerned. Born calculations for the scattering of particles with the same absolute charge, i.e. electrons, positrons, protons, antiprotons etc., on atomic hydrogen yields the results that are different only by a factor. However, there are some advantages of the method. The availability of the explicit analytic formula to describe the scattering amplitude is one of the nice features of the method. Various sophisticated models which allow a switch to the Born mode can be tested using this expression. So, presently this approximation is mainly used to help develop new more advanced theories.

1.3.3 Continuum Distorted Wave-Eikonal Initial State (CDW-EIS)

It is well known that in the presence of a projectile, the atomic cloud is distorted. In early 1983 Crothers and McCain [53] proposed the approach for treatment of the ionization of hydrogen by multi-charged fully-stripped ions which considered this distortion effect. In this approach the distortion in the entrance channel is accounted for via the eikonal approximation. At the same time the exit channel is treated in the Continuum Distorted-Wave approximation. The transition

amplitude is calculated in the post form. The effective perturbation is described by a scalar product of the electron momentum operators, one of these momenta is with respect to the projectile and the other with respect to the projectile. Knowing the transition amplitude one can find cross sections of the elastic, excitation and ionization channels. However the results of Crothers and McCain [53] showed disagreement with the simple first Born calculations even at high energies.

Later this approach was reexamined by Igarashi and Shirai [54]. The authors were able to resolve the discrepancy with the first Born approximation at high energies. As opposed to the work of Crothers and McCain [53], the approach of Igarashi and Shirai [54] treats more accurately the Coulomb-distortion of the initial and final target states. The reduction of the total cross section due to the distortion of the initial state and its increase due to the distortion of the final state compensate each other and yield results which are in line with the first Born approximation at energies above 100 keV/amu.

The total cross sections for the antiproton-impact ionization of hydrogen calculated in the CDW-EIS approximation are in good agreement with the experiment [26], but at lower energies, rapidly drop compared to other nonperturbative calculations.

Apart from the total cross sections the CDW-EIS approach also allows calculation of differential cross sections [34, 35]. In contrast to the first Born approximation, the differential cross sections calculated in the CDW-EIS approximation mimic the effects occurring due to the post-collisional interactions.

1.3.4 Direct-solution methods

There are approaches based on the direct numerical solution of the time-dependent Schrödinger equation. Initially TDSE method was introduced by Maruhn-Rezwani et al. [55] for the proton-hydrogen collisions. To include the rearrangement channel in a correct way the approach was further developed by Kulander et al. [56], Bottcher [57], Gavras et al. [58]. Later, in 1996, for the first time it was implemented for antiproton-hydrogen collisions by Schultz et al. [3] and Wells et al. [59]. The authors discretized the electronic wave function and the Hamiltonian operator on a large three dimensional Cartesian spatial lattice of points using well-known pseudospectral methods. The initial ground state of hydrogen evolves in time during the interaction with the projectile which moves along a classical constant-velocity straight-line trajectory. Through calculating the overlap between the time-evolved state and lattice eigenstates the reaction probabilities, and consequently the ionization cross sections are determined. The results from the direct-solution method for the ionization cross section is in reasonable agreement with the experiment. In order to check the validity of the straight-line approximation at low energy regime the projectile trajectory bending effects were investigated. To this end the trajectory of the projectile was numerically computed by solving Hamilton's equations for the antiproton moving in the ground-state potential-energy curve of the antiproton-hydrogen system. Since in a wide energy range calculations of this kind are challenging and time consuming, only one incident energy of 0.2 keV was considered. The discrepancy between the ionization probabilities at a fixed impact parameter calculated using the straight-line and the curved-line approximations was only 3%. The conclusion from this work is that at the considered energy range (0.2 - 500 keV) the straight-line approximation used for the projectile motion is acceptable.

Another approach which is based on the direct numerical solution of the TDSE has been developed by Sakimoto [9, 60]. The method treats only the radial distance between antiproton and hydrogen classically while the other degrees of freedom are considered quantum mechanically. Thus, the conservation of the total angular momentum is taken into account which makes the method able to treat the bending effect of trajectories of relative motion. The idea itself is similar to that of Wells et al. [59]. However, in contrast to [59], Sakimoto solves the TDSE in the polar coordinates [61–63]. A good agreement between the results of Wells et al. [59] obtained utilizing the Cartesian coordinates and those of Sakimoto [9, 60] obtained utilizing the polar coordinates indicates that a sufficient discretization of the spatial variables has been done in both calculations. A similar method has been applied to study chemical reaction and dissociation in molecular collisions by many authors [64–69]. Later, Sakimoto [70] carried out the fully quantum mechanical calculations for total ionization in $\bar{p}$ + H at very low energies, and compared with his previous semiclassical results. The difference between the two results was shown to be very small. Considering that the semiclassical method for the calculation of the total ionization cross section is satisfactory even at low energies, the author suggested that it should work at intermediate energies as well.

1.3.5 Close-coupling approximations

The most commonly used and rather complicated method is the close-coupling scheme, which is based on the expansion of the total wave function using the target-state wave functions. Most of the close-coupling approaches used in ion-atom collisions substitute this expansion into the approximate time-dependent Schrödinger equation (TDSE) and obtain coupled integro-differential equations in the coordinate space. As already mentioned the TDSE in these approaches is

approximate in the sense that they are derived from the exact time-independent Schrödinger equation as a result of certain semiclassical approximations. In particular, relative motion of the heavy particles is separated as free motion. In addition, the kinetic energy operator corresponding to this motion has no effect on the electronic wavefunction. In fact, within the approximations used in these approaches, one can demonstrate that the interaction between the antiproton and the proton does not contribute to the integrated cross sections [71]. One of the implementations of the close-coupling approach to the study of antiproton scattering on hydrogen was carried out by Hall et al. [18]. They used a single-centred expansion (SCE) in a finite Hilbert basis set (FHBS) method. The size of the underlying basis, for these FHBS calculations, was increased until an acceptable convergence was obtained. As a function of the angular momentum l, associated with the target-centred basis, the cross sections for antiproton collisions converged more rapidly than those for proton collisions calculated by Ford et al. [72]. Their results represent calculations using 273 states with $l \leq 5$. All the reported cross sections are convergent to within 5% for energies less than 10 keV, and 1% for energies above. Later Igarashi et al. [25] applied a similar single-centred approach with larger basis sets. The radial wave function was expanded using the Sturmian functions. They performed calculations utilizing four different basis sets: 263 states for $l = 0 - 5$, 477 states for $l = 0 - 8$, 699 states for $l = 0 - 8$, and 478 states for $l = 0 - 12$. For the first 3 sets all allowed azimuthal components were considered, while for the last set the latter was restricted up to $m = 2$. Results of Igarashi et al. [25] and Hall et al. [18] are in a good agreement. Another single-centred expansion approach was introduced by Azuma et al. [21]. In contrast to the other traditional single-centre expansion CC approaches where the target wave function is expanded in the Sturmian basis, these authors expressed the later by superposition of piecewise B-spline

functions. This allowed them to depict the fine structures of electron distribution near the antiproton more flexibly than employing the Sturmian functions. Hence they were able to express the continuum wave functions more accurately than the traditional pseudostate representation and consequently come closer to the experimental measurements of the ionization cross section.

Toshima [22] has also developed a two-center CC approach to calculate ionization of hydrogen by antiproton impact. In his calculations, Toshima expressed the total time-dependent two-center electronic wave function by superposition of the target (hydrogen) and the projectile (antiproton) atomic orbitals. Using such a basis set the CC scheme was applied. According to his results the two-center effects are not negligible at low energies. Toshima's results show that at the energy of 0.1 keV, the two-center cross section is larger than the one-center one by a factor of 1.4.

Advantages of the above-mentioned close-coupling approaches are in their ability to handle many scattering channels simultaneously and they are relatively less time-consuming as opposed to the fully quantum-mechanical treatment of the problem, however, they are all semiclassical.

Chapter 2

Coupled-channel integral-equation approach to ion-atom collisions

Our main goal is to develop a fully quantum mechanical method to calculate scattering of heavy projectiles on one- and two-electron atoms at non-relativistic energies. In the stationary formulation the total scattering wave function of such collision systems satisfies the time-independent Schrödinger equation where interactions among all involved particles are expressed explicitly. Following the atomic orbital close-coupling scheme we expand the total scattering wave function using a basis made of the target states. If the correct boundary conditions are implemented and resulting equations are solved without approximation, the close-coupling scheme should, in principle, provide a complete description of the scattering process. After expansion the Schrödinger equation for the total wave function is transformed to coupled-channel Lippmann-Schwinger-type integral equations for transition amplitudes in momentum space. The momentum-space integral-equation method in scattering theory is intrinsically powerful for a number of reasons. First of all, the method deals directly with scattering amplitudes. This feature allows to generate the full, as well as various differential cross sec-

tions of all major processes involved. In addition, when formulated rigorously the method implicitly incorporates the correct asymptotic boundary conditions for the scattering problem of interest.

In this chapter we describe our basic formalism, which starts from the full time-independent Schrödinger equation, to treat collisions of heavy projectiles on atomic targets. First, we demonstrate a technique which is used for the description of the total scattering wave-function of the collision system. Then we give the sequence of algebraic derivations which are used to obtain a set of multidimensional integral equations starting from the Schrödinger equation. Finally, we give a brief overview of earlier methods developed for solving the Lippmann-Schwinger integral equations. We use atomic units throughout unless otherwise specified.

2.1 Time-independent Schrödinger equation

We start from a general problem where a structureless projectile of mass m_p and charge Z_P is incident with velocity $\boldsymbol{v}_P$ upon a neutral atom with one active electron. Such a system consists of effectively three particles: projectile, residual ion[1] and active electron. Index α (β) will denote a quantum state in the channel where projectile (residual ion) is free and the other two form a bound state, while index e will be used for the channel where all three particles are free. The total three-body scattering wavefunction at a total energy E is a solution to

$$(H - E)\Psi = 0, \tag{2.1}$$

where

$$H = H_0 + v_\alpha + v_\beta + v_e \equiv H_0 + v, \tag{2.2}$$

[1]In the case of the hydrogen target it is just a proton

H_0 is the free-three-particle Hamiltonian, and v_i is the Coulomb interaction between particles of pair i ($i = \alpha, \beta, e$).

We emphasize that H_0 includes the kinetic energy operator of the projectile. Often in semiclassical treatments of ion-atom collisions this term is ignored. Those approaches use certain semiclassical approximations and derive the equation where the term responsible for the heavy-particle interaction can be transformed into an overall phase factor. Consequently, in the calculations for the integrated cross sections this interaction has no effect whatsoever. Our approach which starts from the full Schrödinger equation (2.1) allows us to test this approximation.

2.2 Expansion of the total scattering wave function

During the collision with a target a projectile can (i) scatter without energy loss leaving the target intact or excite the active electron into higher orbitals; (ii) form a bound state with the active electron or with the target nucleus depending on the sign of its charge. Therefore generally the problem must be treated as having two centers, one associated with the target atom and the other with the system emerged from projectile binding. The most natural way of building the total scattering wavefunction Ψ with proper boundary conditions would be expanding it in terms of states of all asymptotic channels, i.e.

$$\Psi \approx \sum_{\alpha} F_\alpha(\boldsymbol{\rho}_\alpha)\psi_\alpha(\boldsymbol{r}_\alpha) + \sum_{\beta} F_\beta(\boldsymbol{\rho}_\beta)\psi_\beta(\boldsymbol{r}_\beta) + \int de F_e(\boldsymbol{\rho}_e)\psi_e(\boldsymbol{r}_e), \quad (2.3)$$

where ψ_α (ψ_β) is a bound state wavefunction of the target atom (system emerged from projectile binding) in channel α (β), ψ_e is the regular Coulomb function describing the continuum state of the residual ion and projectile pair, with $F_i(\boldsymbol{\rho}_i)$

being the associated weight function. The Jacobi variable $\boldsymbol{r}_i$ is the relative position of particles in pair i and $\boldsymbol{\rho}_i$ is the position of particle i relative to the center of mass (c.m.) of pair i ($i = \alpha, \beta, e$). See Fig. 2.1.

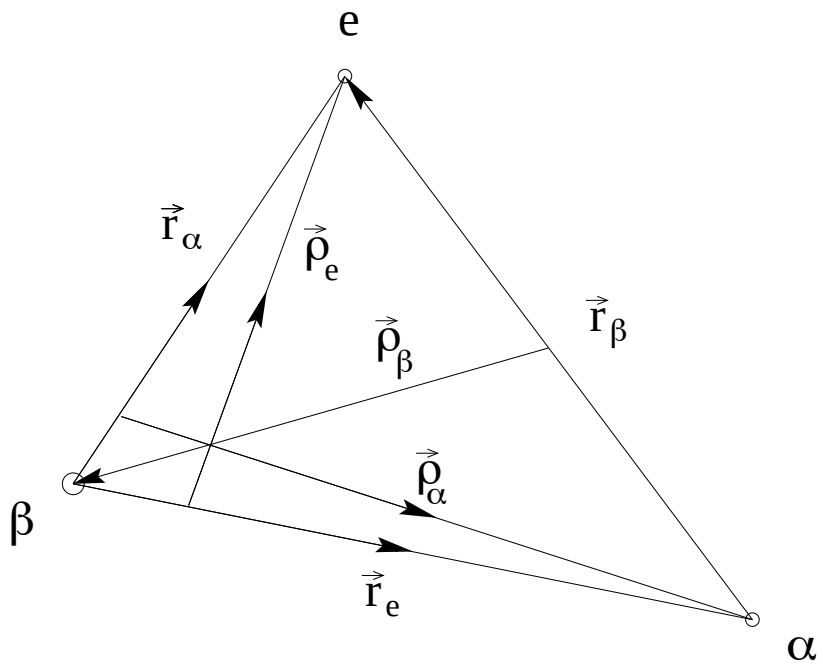

Figure 2.1: Jacobi coordinates for a system of three particles: projectile (α), residual ion (β), and active electron (e).

We expand the total scattering wavefunction using the full sets of functions (i.e. both bound and continuum) of pairs α and β, thereby representing the effect of states in channel e by continuum states of pairs α and β. Namely,

$$\Psi \approx \left\{\sum_\alpha + \int d\alpha\right\} F_\alpha(\boldsymbol{\rho}_\alpha)\psi_\alpha(\boldsymbol{r}_\alpha) + \left\{\sum_\beta + \int d\beta\right\} F_\beta(\boldsymbol{\rho}_\beta)\psi_\beta(\boldsymbol{r}_\beta). \quad (2.4)$$

In principle, it is possible to keep the continuum part only for one of the pairs. This would greatly reduce computational requirements. However, for some collision systems it is important to have an expansion of type (2.4), with the continuum parts for both centers, in order to be able to obtain convergent results [73–76].

The usage of true continuum functions is computationally too difficult. Therefore, we replace them with Laguerre-based pseudostates, as in electron scattering on atomic hydrogen [77]. Accordingly, (2.4) becomes

$$\begin{aligned}\Psi &\approx \sum_{\alpha}^{N_\alpha} F_\alpha(\boldsymbol{\rho}_\alpha)\psi_\alpha^{(N_\alpha)}(\boldsymbol{r}_\alpha) + \sum_{\beta}^{N_\beta} F_\beta(\boldsymbol{\rho}_\beta)\psi_\beta^{(N_\beta)}(\boldsymbol{r}_\beta) \\ &\equiv \sum_{\gamma}^{N_\alpha+N_\beta} F_\gamma(\boldsymbol{\rho}_\gamma)\psi_\gamma(\boldsymbol{r}_\gamma), \end{aligned} \tag{2.5}$$

where the index γ ranges over all α and β. N_α and N_β are the numbers of states of pairs α and β, respectively.

2.3 Momentum-space coupled-channel Lippmann-Schwinger equations

There are a number of ways to find function Ψ in the form (2.5) to best satisfy Eq. (2.1). The simplest way consists in using the Bubnov-Galerkin (BG) principle [78] (a scattering analogue of the Ritz method widely used in bound state problems in quantum mechanics). Substituting the expansion (2.5) into Eq. (2.1) according to the BG principle we require the result to be orthogonal to all ($\gamma' = 1, \ldots, N_\alpha + N_\beta$) basis states

$$\langle\psi_{\gamma'}|(H-E)|\sum_{\gamma}^{N_\alpha+N_\beta} F_\gamma\psi_\gamma\rangle_{\boldsymbol{\rho}_{\gamma'}} \;=\; 0. \tag{2.6}$$

In this equation index $\boldsymbol{\rho}_{\gamma'}$ denotes integration over all variables except $\boldsymbol{\rho}_{\gamma'}$, i.e. the result of the integration is a function of $\boldsymbol{\rho}_{\gamma'}$. The total Hamiltonian can also be expressed in the following way

$$H = H_\gamma + \frac{q_{\gamma'}^2}{2M_{\gamma'}} + U_{\gamma'\gamma}, \tag{2.7}$$

where H_γ is the Hamiltonian of the bound pair in channel γ and $U_{\gamma'\gamma}$ is the interaction potential of the incoming particle γ' with the bound system. Now

taking into account the following identities $\langle\psi_{\gamma'}|\psi_\gamma\rangle = \delta_{\gamma'\gamma}$ and $\langle\psi_{\gamma'}|H_\gamma|\psi_\gamma\rangle = \delta_{\gamma'\gamma}\epsilon_{\gamma'}$ we can write Eq. (2.6) in the following form:

$$\left(E - \epsilon_{\gamma'} - \frac{q_{\gamma'}^2}{2M_{\gamma'}}\right) F_{\gamma'}(\boldsymbol{\rho_{\gamma'}}) = \sum_{\gamma=1}^{N_\alpha+N_\beta} \langle\psi_{\gamma'}|U_{\gamma'\gamma}|\psi_\gamma\rangle\, F_\gamma(\boldsymbol{\rho_\gamma}), \tag{2.8}$$

where $M_{\gamma'}$ is the reduced mass of the two fragments in channel γ' with $M_\alpha = m_\alpha(m_\beta + m_e)/(m_\alpha + m_\beta + m_e)$, $M_\beta = m_\beta(m_\alpha + m_e)/(m_\alpha + m_\beta + m_e)$ and $M_e = m_e(m_\alpha + m_\beta)/(m_\alpha + m_\beta + m_e)$. The potential operators $U_{\gamma'\gamma}$ are given by

$$U_{\alpha,\alpha} = v - v_\alpha, \quad U_{\beta,\beta} = v - v_\beta, \quad U_{\alpha,\beta} = U_{\beta,\alpha} = H_0 + v - E. \tag{2.9}$$

The condition imposed above in Eq. (2.8) is a system of integrodifferential equations for unknown weight functions $F_\gamma(\boldsymbol{\rho_\gamma})$. These functions carry information on the scattering amplitudes. Following [79] we transform these equations for the weight functions to a set of coupled effective two-body Lippmann-Schwinger-type integral equations for transition amplitudes $T_{\gamma'\gamma}$.

By defining the operator of the Green's function

$$\widehat{G}_\gamma = \left(E - \epsilon_\gamma - \frac{q_\gamma^2}{2M_\gamma}\right)^{-1} \tag{2.10}$$

we can write the formal solution of the differential equation (2.8) in the form of

$$\tilde{F}_{\gamma'} = \tilde{F}_0 + \widehat{G}_{\gamma'} \sum_\gamma \langle\psi_{\gamma'}|U_{\gamma'\gamma}|\psi_\gamma\rangle\, \tilde{F}_\gamma, \tag{2.11}$$

where $\tilde{F}_0$ is a solution of Eq. (2.8) when the right hand side is 0, i.e. $\widehat{G}_\gamma^{-1}\tilde{F}_0 = 0$. The latter is a plane wave $|\boldsymbol{q}_\gamma\rangle$ of the relative motion and is an eigenfunction of $\widehat{G}_\gamma^{-1}$

$$G_\gamma^{-1}|\boldsymbol{q}_\gamma\rangle = \left(E - \epsilon_\gamma - \frac{q_\gamma^2}{2M_\gamma}\right)|\boldsymbol{q}\rangle, \tag{2.12}$$

where the plane wave is normalized according to

$$\langle\boldsymbol{q}_\gamma|\boldsymbol{q}_{\gamma'}\rangle = (2\pi)^3\delta(\boldsymbol{q}_\gamma - \boldsymbol{q}_{\gamma'}).$$

Therefore, we can write

$$G_{\gamma'} = \int \frac{d\boldsymbol{q}_{\gamma''}}{(2\pi)^3} \frac{|\boldsymbol{q}_{\gamma''}\rangle \langle \boldsymbol{q}_{\gamma''}|}{E - \epsilon_{\gamma'} - \frac{q^2_{\gamma''}}{2M_{\gamma'}} \pm i0}. \tag{2.13}$$

The above integral contains a singular point at $\frac{q^2_{\gamma'}}{2M_{\gamma'}} = E - \epsilon_{\gamma'}$. The addition of $\pm i0$ defines the integration path around the singularity point at $q_{\gamma'} = \sqrt{2M_{\gamma'}(E - \epsilon_{\gamma'})}$ and, depending on its sign, corresponds to outgoing (+) or incoming (−) wave boundary conditions.

The formal solution of Eq. (2.8) is then

$$|\tilde{F}_{\gamma'}\rangle = |\boldsymbol{q}_{\gamma'}\rangle + \sum_{\gamma} \int \frac{d\boldsymbol{q}_{\gamma''}}{(2\pi)^3} \frac{|\boldsymbol{q}_{\gamma''}\rangle}{E - \epsilon_{\gamma'} - \frac{q^2_{\gamma''}}{2M_{\gamma'}} \pm i0} \langle \boldsymbol{q}_{\gamma''}| \langle \psi_{\gamma'}|U_{\gamma'\gamma}|\psi_{\gamma}\rangle |\tilde{F}_{\gamma}\rangle. \tag{2.14}$$

For the collision channel with initial target state i and incoming wave $|\boldsymbol{q}_i\rangle$ the outgoing-wave (with $+i0$) asymptotes of $F_\gamma(x)$ (where x is $\boldsymbol{\rho}_\alpha$ for α channel, $\boldsymbol{\rho}_\beta$ for β channel and $\boldsymbol{\rho}_e$ for e channel) at $x \to \infty$ must be

$$\tilde{F}_{\gamma'}(x \to \infty) = \delta_{\gamma',i} e^{i\boldsymbol{q}_i \boldsymbol{x}} + f(\boldsymbol{q}_\gamma, \boldsymbol{q}_i) \frac{e^{iq_{\gamma'}x}}{x} \tag{2.15}$$

where $f(\boldsymbol{q}_\gamma, \boldsymbol{q}_i)$ is a scattering amplitude and $q_{\gamma'} = \sqrt{2M_{\gamma'}(E - \epsilon_{\gamma'})}$. On the other hand we can find the asymptotic form of (2.14) corresponding to outgoing-wave boundary conditions [80]. By using the contour integration technique to calculate the integral with a singularity at $\frac{1}{2M_{\gamma'}} q^2_{\gamma''} = E - \epsilon_{\gamma'}$ we get

$$\tilde{F}_{\gamma'}(x \to \infty) = \delta_{\gamma',i} e^{i\boldsymbol{q}_i \boldsymbol{x}} - \frac{M_{\gamma'}}{(2\pi)} \sum_{\gamma} \langle \boldsymbol{q}'| \langle \psi_{\gamma'}|U_{\gamma'\gamma}|\psi_{\gamma}\rangle |\tilde{F}_{\gamma}\rangle \frac{e^{iq_{\gamma'}x}}{x}. \tag{2.16}$$

Comparing the last two we find that

$$f_{\gamma' i}(\boldsymbol{q}_{\gamma'}, \boldsymbol{q}_i) = -\frac{M_{\gamma'}}{(2\pi)} \sum_{\gamma} \langle \boldsymbol{q}_{\gamma'}| \langle \psi_{\gamma'}|U_{\gamma'\gamma}|\psi_{\gamma}\rangle |\tilde{F}^i_{\gamma}\rangle. \tag{2.17}$$

Then from the definition of the on-shell T-matrix

$$T_{\gamma'\gamma}(\boldsymbol{q}_\gamma, \boldsymbol{q}_\gamma) = -\frac{1}{(2\pi)^2 M_{\gamma'}} f_{\gamma'\gamma}(\boldsymbol{q}_\gamma, \boldsymbol{q}_\gamma)$$

it follows that

$$T_{\gamma' i}(\boldsymbol{q}_{\gamma'}, \boldsymbol{q}_i) = \frac{1}{(2\pi)^3} \sum_{\gamma} \langle \boldsymbol{q}_{\gamma'}| \langle \psi_{\gamma'}|U_{\gamma'\gamma}|\psi_\gamma\rangle |\tilde{F}^i_\gamma\rangle. \tag{2.18}$$

Therefore, Eq. (2.14) can be written as

$$|\tilde{F}_{\gamma'}\rangle = \delta_{\gamma',i}|\boldsymbol{q}_i\rangle + \int d\boldsymbol{q}_{\gamma'} \frac{|\boldsymbol{q}_\gamma\rangle}{E - \epsilon_\gamma - \frac{1}{2M_{\gamma'}} q^2_\gamma + i0} T_{\gamma'\gamma}(\boldsymbol{q}_{\gamma'}, \boldsymbol{q}_\gamma). \tag{2.19}$$

Using Eq. (2.19) in Eq. (2.14) we get the Lippmann-Schwinger type equations for the T-matrices

$$\begin{aligned} T_{\gamma'\gamma}(\boldsymbol{q}_{\gamma'}, \boldsymbol{q}_\gamma) =& V_{\gamma'\gamma}(\boldsymbol{q}_{\gamma'}, \boldsymbol{q}_\gamma) \\ &+ \sum_{\gamma''}^{N_\alpha+N_\beta} \int \frac{d\boldsymbol{q}_{\gamma''}}{(2\pi)^3} V_{\gamma'\gamma''}(\boldsymbol{q}_{\gamma'}, \boldsymbol{q}_{\gamma''}) G_{\gamma''}(q^2_{\gamma''}) T_{\gamma''\gamma}(\boldsymbol{q}_{\gamma''}, \boldsymbol{q}_\gamma), \end{aligned} \tag{2.20}$$

where $\boldsymbol{q}_\gamma$ is the momentum of free particle γ relative to c.m. of the bound pair in channel γ. The effective two-body free Green's function is defined as

$$G_{\gamma''}(q^2_{\gamma''}) = (E + i0 - q^2_{\gamma''}/2M_{\gamma''} - \epsilon_{\gamma''})^{-1}, \tag{2.21}$$

and describes the free relative motion of particle γ'' and bound pair γ'' with binding energy $\epsilon_{\gamma''}$.

The effective potentials are given by

$$\begin{aligned} V_{\alpha\alpha}(\boldsymbol{q}_{\alpha'}, \boldsymbol{q}_\alpha) =& \langle \boldsymbol{q}_{\alpha'}|\langle \psi_{\alpha'}|v - v_\alpha|\psi_\alpha\rangle|\boldsymbol{q}_\alpha\rangle, \\ V_{\beta\beta}(\boldsymbol{q}_{\beta'}, \boldsymbol{q}_\beta) =& \langle \boldsymbol{q}_{\beta'}|\langle \psi_{\beta'}|v - v_\beta|\psi_\beta\rangle|\boldsymbol{q}_\beta\rangle, \\ V_{\beta\alpha}(\boldsymbol{q}_\beta, \boldsymbol{q}_\alpha) =& \langle \boldsymbol{q}_\beta|\langle \psi_\beta|H_0 + v - E|\psi_\alpha\rangle|\boldsymbol{q}_\alpha\rangle. \end{aligned} \tag{2.22}$$

2.4 Numerical methods to solve the Lippmann-Schwinger equations

There are number of ways of solving the fully off-shell Lippmann-Schwinger integral equations for the T matrix. In the 1960s, when computational facilities

did not allow one to perform calculations which require a large memory allocation, most approaches were based on the iterative solution of the Lippmann-Schwinger-type equations. In the iterative method the integral equations of type (2.20) can be converted into the Neumann series with infinite number of terms. If the scattering potential is much smaller than the incident energy of projectile, a relatively small number of Neumann terms can yield convergent results. This condition can be met at sufficiently high energies. At lower energies the Neumann series becomes divergent and a straightforward summing of terms does not produce any sensible result. Many methods have been developed to accelerate the convergence of the Neumann series [81–84]. One of them is the Padé method [85]. Theoretically, Pade summation of the Neumann series should converge (if the series is summed up not at the pole, where the result is infinite). However, the Neumann series may be diverging so badly that even tiny numerical inaccuracies in evaluating individual terms a_i may prevent the Pade convergence or at least limit its accuracy. The divergence of the Neumann series is known to be worse at low energies (see, e.g.,[85]). We have done calculations of cross sections for the antiproton elastic scattering on atomic hydrogen using the Pade summation method. The conclusion was that the Pade method is capable of yielding accurate results over a wider range of incident energies than the Born approximation. However, it fails below 50 keV, where the effective scattering potential of the target is so large that the velocities of the orbiting electron and the projectile are comparable.

With further increasing capabilities of high-performance computational facilities, in 1980s, practical solution of large linear matrix equations became possible. This gave birth to a number of approaches which solve the integral equations by transforming them into the set of linear equations using quadrature discretization techniques. However, the available computer resources still did not

allow the direct solution of multichannel three-dimensional integral equations, like (2.20). There was necessity to reduce the complexity of Eq (2.20). This was achieved by expanding the Lippmann-Schwinger equations in partial waves. The spherical symmetry of the collision system allows the wavefunction of the projectile to be expanded in spherical harmonics. This, coupled with the central potentials often found in atomic collision problems, allows one to compute scattering quantities on a partial-wave basis. Although the partial-wave expansion is in principle infinite, for the scattering of electrons or positrons on atoms, the expansion may be truncated after a relatively small number of terms, depending on the energy in question. These facts have allowed partial-wave expansions to be used successfully in the investigation of many electron- and positron-impact processes, such as elastic scattering, excitation and ionization [74, 75, 77, 86–97]. These methods are also readily applied to photon-atom interactions, where similar partial-wave expansions are utilized. In contrast, in collisions in which the projectile is a heavy ion, partial-wave expansions of the wavefunction of the projectile have not been commonly used. This is due to the much heavier mass of an incoming ion (for example, the lightest ion projectile, the proton, has a mass of 1836 that of an electron). Approximate scaling arguments [98] for the number of partial waves required ($J_{\max}$) to fully describe an interaction lead to $J_{\max} \sim ka$, where a is a measure of the range of the atomic potential, and k is the momentum. Since the momentum of an incoming ion is usually much greater than the momentum of an incoming electron, this scaling implies that thousands of partial waves may be required to fully treat an ion-atom collision. This makes the partial wave method inefficient as far as ion-atom collisions are concerned.

Recently we have developed a simple non-partial-wave approach [99–101] to solve momentum-space integral equations (2.20) directly. Using this method we

have been able to calculate elastic cross sections for proton- as well as antiproton-hydrogen collisions. For the full treatment of multichannel ion-atom scattering we have developed an approach which transforms the Lippmann-Schwinger equations into the impact parameter representation [40, 102]. The following chapters describe the formalism for solving the Lippmann-Schwinger equations using the direct-integration and impact-parameter methods.

2.5 Chapter summary

In this chapter we have presented the basic formalism of our fully quantum-mechanical approach to ion-atom collisions. The approach starts from the time-independent Schrödinger equation where interactions among all involved particles are expressed explicitly. Following the close-coupling scheme the total scattering wave function has been expanded in terms of states of all asymptotic channels. After expansion of the wave function the Schrödinger equation has been transformed into the coupled-channel Lippmann-Schwinger integral equations in momentum space. Different numerical methods to solve the Lippmann-Schwinger integral equations developed in the past have been briefly discussed. In the next chapters, we present our recently developed direct integration and impact-parameter approaches to solving these equations.

Chapter 3

A direct solution of the Lippmann-Schwinger integral equations

In this chapter we explore the alternative approach to solving scattering equations (2.20) directly without recourse to a partial-wave expansion or any other transformation scheme. We study the most fundamental ion-atom collision processes - scattering of a proton and an antiproton on the ground state of a hydrogen atom. We adopt the close-coupling scheme and expand the total scattering wave function in terms of channel functions. However, for the sake of simplicity we truncate this expansion and consider here a model that retains only the ground state of the atom. The direct approach to solving multidimensional momentum-space integral equations provide a base for the development of the fully quantal method not only to ion-atom collisions but also to many other scattering processes since similar equations are widely used in other branches of scattering theory as well. Three-dimensional momentum-space integral equations emerge, for example, in approaches like the close-coupling approach to electron-atom scattering [103] and positronium formation [75].

3.1 Two-channel momentum-space integral equations

Below we give details of our approach to solve the Lippmann-Schwinger integral equations (2.20) directly in the examples of proton and antiproton scattering on a hydrogen atom in the ground state. We concentrate in the projectile energy range from 100 eV to 1 MeV. In the case of an incident proton there could be direct scattering of the proton or the proton may leave the reaction zone having captured the electron of the atom. At energies 100 eV and above we can treat the protons as distinguishable particles. In the case of the antiproton the rearrangement channel leads to formation of protonium, a bound state of antiproton and proton. However, in the energy range of our interest the probability of protonium formation is negligible [3]. We describe the formalism for the proton as a projectile. When the projectile is an antiproton we simply neglect the rearrangement channel. In order to simplify the problem and make calculations feasible we construct the total scattering wave function using only the ground states of atomic hydrogen in the direct and rearrangement channels. This is equivalent to the truncation of Eq. (2.5) leaving only two bound states. In this case the scattering equation (2.20) is a set of the following two integral equations

$$\begin{cases} T_{\alpha\alpha}(\boldsymbol{q}'_\alpha,\boldsymbol{q}_\alpha) = & V_{\alpha\alpha}(\boldsymbol{q}'_\alpha,\boldsymbol{q}_\alpha) + \int d\boldsymbol{q}\dfrac{V_{\beta\alpha}(\boldsymbol{q}_\beta,\boldsymbol{q})T_{\alpha\alpha}(\boldsymbol{q},\boldsymbol{q}_\alpha)}{(q_\alpha^2/2M - q^2/2M + i0)} \\ & + \int d\boldsymbol{q}\dfrac{V_{\beta\beta}(\boldsymbol{q}_\beta,\boldsymbol{q})T_{\beta\alpha}(\boldsymbol{q},\boldsymbol{q}_\alpha)}{(q_\alpha^2/2M - q^2/2M + i0)}, \\ T_{\beta\alpha}(\boldsymbol{q}_\beta,\boldsymbol{q}_\alpha) = & V_{\beta\alpha}(\boldsymbol{q}_\beta,\boldsymbol{q}_\alpha) + \int d\boldsymbol{q}\dfrac{V_{\beta\alpha}(\boldsymbol{q}_\beta,\boldsymbol{q})T_{\alpha\alpha}(\boldsymbol{q},\boldsymbol{q}_\alpha)}{(q_\alpha^2/2M - q^2/2M + i0)} \\ & + \int d\boldsymbol{q}\dfrac{V_{\beta\beta}(\boldsymbol{q}_\beta,\boldsymbol{q})T_{\beta\alpha}(\boldsymbol{q},\boldsymbol{q}_\alpha)}{(q_\alpha^2/2M - q^2/2M + i0)}, \end{cases} \tag{3.1}$$

where $\boldsymbol{q}$ is the momentum of a freely traveling proton relative to the c.m. of the hydrogen atom in the final channel, $M = m(m+1)/(2m+1)$ is the reduced mass of the two fragments and m is the mass of the proton. The transition am-

plitudes $T_{\alpha\alpha}$ and $T_{\beta\alpha}$ describe elastic scattering and electron capture processes, respectively.

Conventional approaches use expansions of $V_{\beta\alpha}(\boldsymbol{q}_\beta, \boldsymbol{q}_\alpha)$ and $T_{\beta\alpha}(\boldsymbol{q}_\beta, \boldsymbol{q}_\alpha)$ into partial waves. Then Eq. (3.1) transforms into a sum of one-dimensional integral equations for each partial-wave amplitude. With today's computer power, accurate solution of a large set of one-dimensional integral equations is a routine task [103]. This method is very effective for collisions of light particles such as electron and positron scattering from atoms. In these cases a small number of partial waves (as a rule less than 20 in a wide energy range) give the main contribution to the sum. This result can be reliably extrapolated to incorporate the contribution from all remaining partial waves. Therefore, all important atomic states (eigen and pseudo) can easily be included into the scheme. However, here we have a situation where the contribution from a thousand or more partial waves is significant. Though the partial-wave approach is still valid, it is impractical. Firstly, too many partial-wave amplitudes need to be calculated. Secondly, possible numerical precision problems in evaluating large angular-momentum Clebsch-Gordon coefficients make inclusion of higher partial waves problematic. At the same time progress in high-performance computing has reached the stage where direct solution of the three-dimensional momentum space integral equations (3.1) is possible.

In order to solve Eq. (3.1) directly in three-dimensional momentum space we first calculate the effective potentials in closed form. This will be given in the next section.

3.2 Effective potentials: Direct transition

Following the formal definition of effective potentials (2.22) we can write the direct transition elements as

$$V_{\alpha\alpha}(\boldsymbol{q}'_\alpha, \boldsymbol{q}_\alpha) = \int\int d\boldsymbol{\rho}_\alpha d\boldsymbol{r}_\alpha e^{-i\boldsymbol{q}'_\alpha\boldsymbol{\rho}_\alpha}\psi^*_\alpha(\boldsymbol{r}_\alpha)(v_\beta + v_\gamma)\psi_\alpha(\boldsymbol{r}_\alpha)e^{i\boldsymbol{q}_\alpha\boldsymbol{\rho}_\alpha}. \quad (3.2)$$

Here the Jacobi variable $\boldsymbol{r}_\alpha$ is the position of the electron of the atom and $\boldsymbol{\rho}_\alpha$ is the position of the incident proton relative to the atom. v_i is the Coulomb interaction between particles of pair i ($i = \alpha, \beta$). See Fig. 2.1. In the model considered the function ψ_α is the ground state wave function of atomic hydrogen

$$\psi_\alpha(\boldsymbol{r}_\alpha) = \frac{1}{\sqrt{4\pi}} 2e^{-r_\alpha}. \quad (3.3)$$

Calculation of the $V_{\alpha\alpha}(\boldsymbol{q}'_\alpha, \boldsymbol{q}_\alpha)$ for the off-shell case is easy and the result is similar to the on-shell one

$$V_{\alpha\alpha}(\boldsymbol{q}'_\alpha, \boldsymbol{q}_\alpha) = 4\pi \frac{\Delta^2_{\alpha\alpha}(1 - 1/m^4) + 8(1 - 1/m^2)}{(\Delta^2_{\alpha\alpha}/4m^2 + 1)^2(\Delta^2_{\alpha\alpha} + 4)^2}, \quad (3.4)$$

where $\Delta_{\alpha\alpha} = |\boldsymbol{q}_\alpha - \boldsymbol{q}'_\alpha|$ is the momentum transfer.

3.3 Effective potentials: Rearrangement

Calculation of the effective potential for the rearrangement transition (electron transfer) is relatively more involved. The effective potential for rearrangement $\alpha \to \beta$ transition is defined as

$$\begin{aligned} V_{\beta\alpha}(\boldsymbol{q}_\beta, \boldsymbol{q}_\alpha) &= \langle \boldsymbol{q}_\beta | \langle \psi_\beta | H_0 + v_\alpha + v_\beta + v_\gamma - E | \psi_\alpha \rangle | \boldsymbol{q}_\alpha \rangle \\ &= \int\int d\boldsymbol{\rho}_\beta d\boldsymbol{r}_\beta e^{-i\boldsymbol{q}_\beta\boldsymbol{\rho}_\beta}\psi^*_\beta(\boldsymbol{r}_\beta) \\ &\times (H_0 + v_\alpha + v_\beta + v_\gamma - E)\psi_\alpha(\boldsymbol{r}_\alpha)e^{i\boldsymbol{q}_\alpha\boldsymbol{\rho}_\alpha}. \end{aligned} \quad (3.5)$$

We apply the operator $H_0 - E$ on the initial state wave function and denote the result by $\mathcal{E}(\boldsymbol{q}_\beta, \boldsymbol{q}_\alpha)$:

$$q_\alpha^2/2M_\alpha + p_\alpha^2/2M_\alpha - E \equiv \mathcal{E}(\boldsymbol{q}_\beta, \boldsymbol{q}_\alpha). \tag{3.6}$$

We could apply this operator on the final state wave function to get the result $q_\beta^2/2M_\beta + p_\beta^2/2M_\beta - E$. Clearly, $q_\alpha^2/2M_\alpha + p_\alpha^2/2M_\alpha = q_\beta^2/2M_\beta + p_\beta^2/2M_\beta$. Here $\boldsymbol{p}_\gamma$ is the momentum of the internal relative motion of the particles of pair γ, a canonical conjugate of the Jacobi variable $\boldsymbol{r}_\gamma$:

$$\boldsymbol{p}_\beta = \boldsymbol{q}_\alpha - a\boldsymbol{q}_\beta \text{ and } \boldsymbol{p}_\alpha = a\boldsymbol{q}_\alpha - \boldsymbol{q}_\beta, \tag{3.7}$$

where $a = m/(m+1)$.

Let us split $V_{\beta\alpha}(\boldsymbol{q}_\beta, \boldsymbol{q}_\alpha)$ into two parts:

$$\begin{aligned} V_{\beta\alpha}(\boldsymbol{q}_\beta, \boldsymbol{q}_\alpha) =& \int\int d\boldsymbol{\rho}_\beta d\boldsymbol{r}_\beta e^{-i\boldsymbol{q}_\beta\boldsymbol{\rho}_\beta}\psi_\beta^*(\boldsymbol{r}_\beta)(\mathcal{E}(\boldsymbol{q}_\beta, \boldsymbol{q}_\alpha) + v_\alpha + v_\beta)\psi_\alpha(\boldsymbol{r}_\alpha)e^{i\boldsymbol{q}_\alpha\boldsymbol{\rho}_\alpha} \\ &+ \int\int d\boldsymbol{\rho}_\beta d\boldsymbol{r}_\beta e^{-i\boldsymbol{q}_\beta\boldsymbol{\rho}_\beta}\psi_\beta^*(\boldsymbol{r}_\beta)v_e\psi_\alpha(\boldsymbol{r}_\alpha)e^{i\boldsymbol{q}_\alpha\boldsymbol{\rho}_\alpha} \\ \equiv& V_{\beta\alpha}^{(I)}(\boldsymbol{q}_\beta, \boldsymbol{q}_\alpha) + V_{\beta\alpha}^{(II)}(\boldsymbol{q}_\beta, \boldsymbol{q}_\alpha). \end{aligned} \tag{3.8}$$

Evidently,

$$V_{\beta\alpha}^{(I)}(\boldsymbol{q}_\beta, \boldsymbol{q}_\alpha) = \mathcal{E}(\boldsymbol{q}_\beta, \boldsymbol{q}_\alpha)\widetilde{\psi}_\beta^*(\boldsymbol{p}_\beta)\widetilde{\psi}_\alpha(\boldsymbol{p}_\alpha) + \widetilde{\psi}_\beta^*(\boldsymbol{p}_\beta)\widetilde{g}_\alpha(\boldsymbol{p}_\alpha) + \widetilde{g}_\beta^*(\boldsymbol{p}_\beta)\widetilde{\psi}_\alpha(\boldsymbol{p}_\alpha) \tag{3.9}$$

and

$$V_{\beta\alpha}^{(II)}(\boldsymbol{q}_\beta, \boldsymbol{q}_\alpha) = \int \frac{d\boldsymbol{p}}{(2\pi)^3}\widetilde{\psi}_\beta^*(\boldsymbol{p} - \boldsymbol{p}_\beta)\frac{4\pi}{p^2}\widetilde{\psi}_\alpha(\boldsymbol{p} + \boldsymbol{p}_\alpha), \tag{3.10}$$

where the momentum space wave function $\widetilde{\psi}_\nu(\boldsymbol{q})$ and formfactor $\widetilde{g}_\nu$ in the ground state are defined as

$$\widetilde{\psi}_\nu(\boldsymbol{q}) = \frac{1}{\sqrt{4\pi}}\int_0^\infty 2e^{-r_\alpha}j_0(qr_\alpha)rdr = \frac{16\pi}{(q^2+1)^2}, \tag{3.11}$$

and

$$\widetilde{g}_\nu(\boldsymbol{q}) = \frac{1}{\sqrt{4\pi}} \int\limits_0^\infty 2e^{-r_\alpha} j_0(qr_\alpha) dr = \frac{8\pi}{q^2+1}, \tag{3.12}$$

respectively.

The term $V^{(I)}_{\beta\alpha}(\boldsymbol{q}_\beta, \boldsymbol{q}_\alpha)$ in the on-shell case was evaluated by Oppenheimer [104] and Brinkman and Kramers [105]. The fully off-shell amplitude which we need in our integral equations is different and given as

$$V^{(I)}_{\beta\alpha}(\boldsymbol{q}_\beta, \boldsymbol{q}_\alpha) \;\; = \;\; \frac{32\pi a^5 (q_\alpha^2/M_\alpha - q_0^2/M_\alpha - p_\beta^2/a - a)}{(p_\beta^2 + a^2)^2 (p_\alpha^2 + a^2)^2}, \tag{3.13}$$

or, equivalently,

$$V^{(I)}_{\beta\alpha}(\boldsymbol{q}_\beta, \boldsymbol{q}_\alpha) \;\; = \;\; \frac{32\pi a^5 (q_\beta^2/M_\alpha - q_0^2/M_\alpha - p_\alpha^2/a - a)}{(p_\beta^2 + a^2)^2 (p_\alpha^2 + a^2)^2}. \tag{3.14}$$

On the energy shell both forms reduce to the Oppenheimer-Brinkman-Kramers amplitude.

The term $V^{(II)}_{\beta\alpha}(\boldsymbol{q}_\beta, \boldsymbol{q}_\alpha)$ in the on-shell case was evaluated by Jackson and Schiff [106]. The fully off-shell amplitude which we need in our integral equations is quite different

$$V^{(II)}_{\beta\alpha}(\boldsymbol{q}_\beta, \boldsymbol{q}_\alpha) = \frac{32a^5}{\pi} \int \frac{d\boldsymbol{p}}{p^2} \frac{1}{(|\boldsymbol{p} - \boldsymbol{p}_\beta|^2 + a^2)^2 (|\boldsymbol{p} + \boldsymbol{p}_\alpha|^2 + a^2)^2}. \tag{3.15}$$

In the on-shell case (i.e., when $p_\beta = p_\alpha$) the last integral has been calculated [106] using the Feynman parametrisation technique. We calculate it for the general

off-shell case (i.e., when $p_\beta \neq p_\alpha$) in a similar way to get

$$
\begin{aligned}
V^{(II)}_{\beta\alpha}(\boldsymbol{q}_\beta, \boldsymbol{q}_\alpha) = \frac{16\pi a^5}{s^5}\Bigg\{ & a(P_\alpha + P_\beta)\left[\frac{2a^2(P_\alpha - P_\beta)^2}{P_\alpha P_\beta} + \Delta^2_{\beta\alpha}\right] s \\
& - \left[4a^4(P_\alpha - P_\beta)^2 + 2a^2\left(P^2_\alpha - P_\alpha P_\beta + P^2_\beta\right)\Delta^2_{\beta\alpha} - P_\alpha P_\beta \Delta^4_{\beta\alpha}/2\right] t \\
& + \Big[2(P_\alpha + P_\beta)\left(12a^4(P_\alpha - P_\beta)^2 + a^2(P_\alpha - P_\beta)^2\Delta^2_{\beta\alpha} + 2P_\alpha P_\beta \Delta^4_{\beta\alpha}\right) s \\
& - 3aP_\alpha(P_\alpha - P_\beta)^2 P_\beta (4a^2 + \Delta^2_{\beta\alpha})^2 t\Big] / [2a(4a^2 + \Delta^2_{\beta\alpha})^2] \\
& - 2a\frac{8a^2(P_\alpha - P_\beta)^2 + (3(P_\alpha - P_\beta)^2 - 4P_\alpha P_\beta)\,\Delta^2_{\beta\alpha}}{4a^2 + \Delta^2_{\beta\alpha}} s \\
& + (P_\alpha + P_\beta)(2a^2(P_\alpha - P_\beta)^2 + P_\alpha P_\beta \Delta^2_{\beta\alpha}) t\Bigg\},
\end{aligned}
\tag{3.16}
$$

where

$$
s = \sqrt{(P_\alpha - P_\beta)^2 - P_\alpha P_\beta \Delta^2_{\beta\alpha}}, \tag{3.17}
$$

$$
t = \log\left[\frac{P_\alpha}{P_\beta}\right] + \log\left[\frac{2(P_\alpha - P_\beta) + 2s - P_\beta \Delta^2_{\beta\alpha}}{2(P_\alpha - P_\beta) + 2s + P_\alpha \Delta^2_{\beta\alpha}}\right] \tag{3.18}
$$

and $P_\alpha = a^2 + p^2_\alpha$, $P_\beta = a^2 + p^2_\beta$, $\Delta_{\beta\alpha} = |\boldsymbol{q}_\alpha + \boldsymbol{q}_\beta|$. On the energy shell this amplitude reduces to the Jackson-Schiff amplitude [106].

3.4 Details of Calculations

The system of equations (3.1) is solved directly in three-dimensional space. From a practical point of view it is convenient to make the following transformation: $\boldsymbol{q}_\beta \to -\boldsymbol{q}_\beta$. Then we can introduce a combined amplitude $T(\boldsymbol{q}', \boldsymbol{q}) = \{T_{\alpha\alpha}(\boldsymbol{q}', \boldsymbol{q}), T_{\beta\alpha}(\boldsymbol{q}', \boldsymbol{q})\}$ and effective potential $V(\boldsymbol{q}', \boldsymbol{q}) = \{V_{\alpha\alpha}(\boldsymbol{q}', \boldsymbol{q}), V_{\beta\alpha}(\boldsymbol{q}', \boldsymbol{q})\}$. We use the spherical coordinate system $\boldsymbol{q} = \{q, \theta, \varphi\}$. The z-axis is set along the incident momentum and a compact notation $T(q', \theta', \varphi') \equiv T(q', \theta', \varphi';\, q, 0, 0)$ is used. Then in spherical coordinates Eq. (3.1) is written as

$$
\begin{aligned}
T(q', \theta', \varphi') = & V(q', \theta', \varphi'; q, 0, 0) + \int_0^\infty dq'' \int_0^\pi d\theta'' \int_0^{2\pi} d\phi'' \\
& \times \frac{2Mq''^2 \sin\theta''}{(2\pi)^3} \frac{V(q', \theta', \varphi'; q'', \theta'', \varphi'') T(q'', \theta'', \varphi'')}{q^2 - q''^2 + i0}.
\end{aligned}
\tag{3.19}
$$

The integral in Eq. (3.19) is singular. Application of the Cauchy principal-value (PV) formulae for this integral leads to

$$\begin{aligned} T(q',\theta',\varphi') =& V(q',\theta',\varphi';q,0,0) \\ &+ \mathrm{PV}\int_0^\infty \frac{dq''}{q-q''}\int_0^\pi d\theta''\int_0^{2\pi} d\phi'' K(q',\theta',\varphi';q'',\theta'',\varphi'')T(q'',\theta'',\varphi'') \\ &- i\pi\int_0^\pi d\theta''\int_0^{2\pi} d\phi'' K(q,\theta',\varphi';q,\theta'',\varphi'')T(q,\theta'',\varphi''), \end{aligned} \tag{3.20}$$

where

$$K(q',\theta',\varphi';q'',\theta'',\varphi'') = \frac{2Mq''^2\sin\theta''}{(2\pi)^3}\frac{V(q',\theta',\varphi';q'',\theta'',\varphi'')}{q+q''} \tag{3.21}$$

is the kernel of the equation.

Recently in [99] three-dimensional integral equation (3.20) for scattering amplitude $T(q,\theta,\varphi)$ have been solved for electron-hydrogen collisions using a three-dimensional quadrature. It was explicitly demonstrated that the result (when it has converged and is correct) did not depend on variable φ. Here we take advantage of this fact to substantially reduce the complexity of the problem. Since $T(q,\theta,\varphi)$ does not depend on variable φ we can simply set $\varphi = 0$. Then from Eq. (3.20) we obtain

$$\begin{aligned} T(q',\theta',0) =& V(q',\theta',0;q,0,0) + \mathrm{PV}\int_0^\infty \frac{dq''}{q-q''}\int_0^\pi d\theta'' D(q',\theta';q'',\theta'')T(q'',\theta'',0) \\ &- i\pi\int_0^\pi d\theta'' D(q,\theta';q,\theta'')T(q,\theta'',0), \end{aligned} \tag{3.22}$$

where

$$D(q',\theta';q'',\theta'') = \int_0^{2\pi} d\varphi'' K(q',\theta',0;q'',\theta'',\varphi''). \tag{3.23}$$

Thus instead of the three-dimensional integral equation we have got effectively a two-dimensional one. Integration over φ'' is performed inside the new kernel D. As a consequence computer memory and CPU requirements drastically reduce. This idea has been first tested in the on-shell case where the principle-value

integral has been neglected [100]. This time we have applied it without approximations. It has been carefully checked that solutions of Eq. (3.20) and Eq. (3.22) do in fact yield the same results. The advantage is that the latter required much less computation due to effectively being two-dimensional. The reason why Eq. (3.22) can be used was given in [100]. The point is that, in addition to $T(q,\theta,\varphi)$ being independent of φ, effective potential $V(\boldsymbol{q}';\boldsymbol{q}'')$ entering Eq. (3.20) depends only on q', q'' and $\boldsymbol{q}'\cdot\boldsymbol{q}''$. Since $\boldsymbol{q}'\cdot\boldsymbol{q}'' = q'q''[\cos\theta'\cos\theta''+\sin\theta'\sin\theta''\cos(\varphi'-\varphi'')]$ we see that $V(\boldsymbol{q}';\boldsymbol{q}'')$ is a periodic function of $\varphi'-\varphi''$. Consequently, if variable φ'' goes over the full period the value of φ' is irrelevant. In other words, in our approach we have in fact a system of two-dimensional singular integral equations. This system of equations is solved using the standard Gauss-Legendre quadrature.

The standard Gauss-Legendre quadrature has been used in order to discretize integrals over variables φ and θ. For the principal-value integral over q-variable a composite mesh has been used. The mesh included a subquadrature consisting of an even number of Gauss-Legendre points, symmetrically distributed around the singular point. This subquadrature was designed to ensure a high accuracy for the principal-value integral.

After applying the quadrature rules to Eq. (3.22) and evaluating the result at the mesh points we obtain

$$\begin{aligned} T(q_{i_q},\theta_{i_\theta},0) =& V(q_{i_q},\theta_{i_\theta},0;q_0,0,0) + \sum_{j_q=0}^{N_q}\sum_{j_\theta=1}^{N_\theta}\tilde{D}(q_{i_q},\theta_{i_\theta};q_{j_q},\theta_{j_\theta}) \\ & \times T(q_{j_q},\theta_{j_\theta},0), \end{aligned} \tag{3.24}$$

with

$$\tilde{D}(q_{i_q},\theta_{i_\theta};q_{j_q},\theta_{j_\theta}) \;=\; ((1-\delta_{j_q0}) - i\pi\delta_{j_q0})w_{j_q}u_{j_\theta}D(q_{i_q},\theta_{i_\theta};q_{j_q},\theta_{j_\theta}), \tag{3.25}$$

where q_{j_q}, θ_{j_θ} and w_{j_q}, u_{j_θ} are the mesh points and associated weights, N_q and

N_θ are the number of points in the q and θ quadratures, respectively. Index 0 is assigned to the on-shell momentum and w_0 is set equal to 1. In the matrix form Eq. (3.24) is written as

$$(\mathbf{1} - \tilde{\boldsymbol{D}}) \cdot \boldsymbol{T} \;=\; \boldsymbol{V}, \tag{3.26}$$

where $\boldsymbol{V}$ and $\boldsymbol{T}$ are N-dimensional vectors and $\tilde{\boldsymbol{D}}$ is a $N \times N$ matrix with $N = (N_q + 1)N_\theta$.

3.5 Results of numerical calculations

The off-shell effects in three-body equations for electron transfer in ion-atom collisions were evaluated in Ref. [107] using an iterative method. The contribution of principal-value integrals was considered as a correction and the zeroth- (i.e., on-shell) and first-order results were compared. In the energy range from 200 eV to 500 keV in the laboratory frame the contribution from the off-shell effects to the first-order total electron transfer cross section ($\sigma^1_{\beta\alpha}$) in proton-hydrogen collisions was somewhere between 5.8% down to 0.0%. The conclusion was that the off-shell effects were small. We have calculated the total electron transfer ($\sigma_{\beta\alpha}$) and elastic scattering cross sections ($\sigma_{\alpha\alpha}$) for proton collisions with H($1s$) at the incident projectile energies from 100 eV to 2 MeV. The scattering amplitudes have been obtained by solving Eq. (3.26) where the contribution of the off-shell effects is fully taken into account. Table 3.1 shows the relative contribution of the off-shell effects in comparison with the first-order results of Ref. [107]. The on-shell cross sections ($\sigma^{\rm on}_{\beta\alpha}$ and $\sigma^{\rm on}_{\alpha\alpha}$) are taken from Ref. [100].

The first calculations at 100 eV show that the off-shell effects only slightly increase the total electron transfer cross section. At 200 eV the change is 5.4% which is close to 3.8% predicted in Ref. [107]. However, the change is in the opposite direction. The off-shell effects continue having a negative effect on the

Table 3.1: Relative contribution of the off-shell effects (in %) in electron-capture and elastic-scattering cross sections for p + H($1s$) collisions.

Energy (keV)	$\frac{\sigma_{\beta\alpha}-\sigma^{\rm on}_{\beta\alpha}}{\sigma^{\rm on}_{\beta\alpha}}$	$\frac{\sigma^{\rm I}_{\beta\alpha}-\sigma^{\rm on}_{\beta\alpha}}{\sigma^{\rm on}_{\beta\alpha}}$ (Ref. [107])	$\frac{\sigma_{\alpha\alpha}-\sigma^{\rm on}_{\alpha\alpha}}{\sigma^{\rm on}_{\alpha\alpha}}$
0.1	0.5		-27.5
0.2	-5.4	3.8	-13.9
0.5	-12.9		15.9
1	-15.8	1.0	26.3
2	-13.3		35.3
5	-3.4		76.8
10	36.9		72.9
20	62.9	5.8	75.3
50	63.3	4.0	53.5
100	65.7	0.5	28.5
200	77.4		14.2
500	106	0.0	6.1
1000	103		3.3
2000	101		1.8

cross section up to 5 keV decreasing it by 16% around 1 keV. Starting from 10 keV the off-shell effects only add to the cross section and the contribution quickly rising with energy. At high energies as much as a half of the total electron-transfer cross section comes from the off-shell effects. This is somewhat surprising and contradicts the aforementioned classical and iterative estimates which predict these effects to be small. The off-shell effects are small only at about 150 eV and 6 keV where their contribution goes through zero to change its sign. Otherwise they are always significant and cannot be neglected.

The question is why these effects remain so strong even at high energies? Before we try to answer this question, let us first look at the situation with elastic scattering. Table 3.1 also shows the off-shell contribution to the total elastic cross section. Here again it can both increase or decrease the cross sections substantially depending on energy reaching the maximum of 77% at about 5

keV. However, this time the significance of the off-shell effects does fall at high energies to a few-percent level.

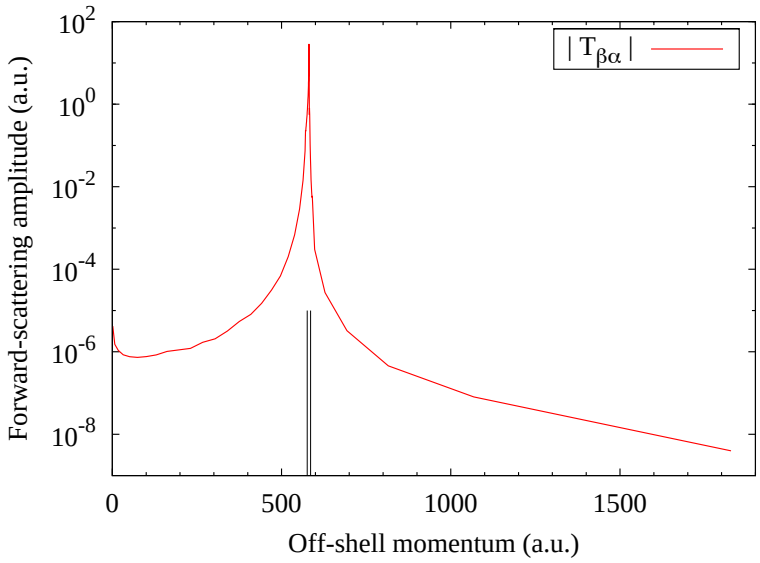

Figure 3.1: Magnitude of amplitude for electron capture in p + H($1s$) collisions.

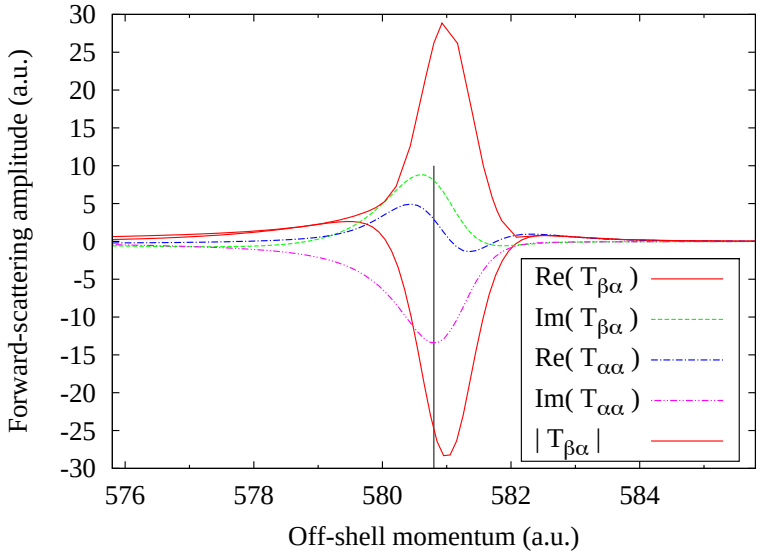

Figure 3.2: Amplitude for electron capture and elastic scattering in p + H($1s$) collisions.

Fig. 3.1 shows the magnitude of the half-off-shell amplitude for electron

transfer in the forward direction, $|T_{\beta\alpha}(q,0,0)|$, at 10 keV, as an example of a typical behavior. It has a spike-like dependence as a function of the magnitude of off-shell momentum (we emphasize that the Y-axis is logarithmic). However, this is not a δ-function which the on-shell approximation assumes. That is why the off-shell effects are significant. There is a small maximum at zero momentum, however the main physics is concentrated in the close neighborhood of the on-shell momentum. The absolute magnitude of the half-off-shell amplitude for elastic scattering in the forward direction, $|T_{\alpha\alpha}(q,0,0)|$, behaves in a very similar way. Two vertical bars show a narrow region around the on-shell point. The half-off-shell amplitudes for electron transfer and elastic scattering in the forward direction at 10 keV in this region are depicted in Fig. 3.2. The vertical line in Fig. 3.2 goes through the on-shell momentum. As one can see, the maximum of the amplitude is close but not exactly at the on-shell point. As energy increases this deviation becomes larger for $|T_{\beta\alpha}(q,0,0)|$ but stays almost the same for $|T_{\alpha\alpha}(q,0,0)|$. At lower energies the amplitudes have more oscillations near the on-shell point. A similar, but less pronounced picture is observed for other scattering angles. The behavior of the scattering amplitudes as functions of q indicates existence of a pole singularity in a complex-q plane close to the physical region. That pole should correspond to a resonance state in the two proton-one electron system.

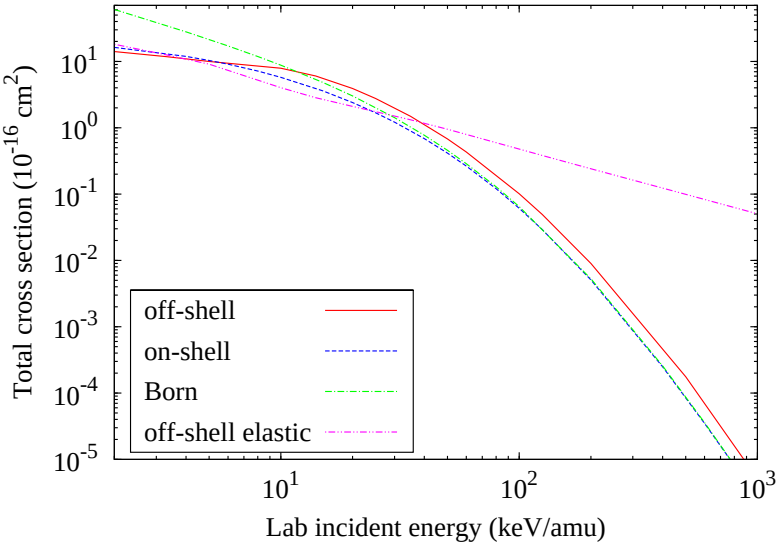

Figure 3.3: Total cross sections for electron capture in p + H($1s$) collisions. Present results for elastic scattering are also given.

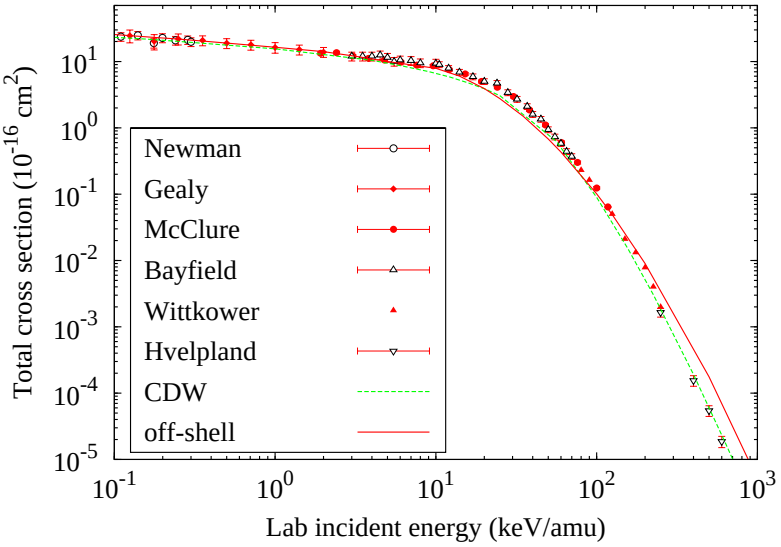

Figure 3.4: Total cross sections for electron capture in p + H($1s$) collisions. The symbols indicate experimental measurements of Newman et al. [108], Gealy and Van Zyl [109], McClure [110], Bayfield [111], Wittkower et al. [112], Hvelpland and Andersen [113], while the lines show the present off-shell results and the CDW calculations of Ferreira da Silva and Serrão [114].

We can try to understand the reason why the off-shell effects in electron

transfer remain strong even at high energies from Fig. 3.3, which shows the corresponding total cross section in comparison with the on-shell and Born calculations. The on-shell cross section merges with the Born cross section at high energies as expected. Also shown in Fig. 3.3 is the off-shell elastic scattering cross section which, at high energies, is a few orders of magnitude larger than the electron-transfer cross section. It is the strong coupling (through the off-shell equations) of the transfer amplitude to the dominant direct-scattering amplitude that makes the off-shell contributions remain so large even at high energies. The calculated cross section converges towards Born result only provided the dominant direct channel is decoupled. (To confirm this point we performed electron-transfer calculations neglecting the direct-scattering channel at 1, 10, 100 keV and 1 MeV. This reduced the off-shell effects to -13.1, 22.0, 4.54 and 0.015%, respectively.) With inclusion of excitation and ionization channels we expect that the electron-transfer cross section will move back towards the experiment at high energies. We emphasize that our model is unitary and distributes the particle flux between the included channels through coupling. This is verified by the fact that the optical theorem is satisfied to at least four-digit accuracy at all energies considered.

Fig. 3.4 shows our results for electron-capture cross sections in comparison with the CDW calculations [114] and experimental data [108–113]. The agreement between our results and the experimental data is generally good though not as good as for CDW ones. The agreement has improved in comparison with the on-shell calculations. The present electron-capture cross sections overestimate the data above 200 keV. This is because here the ionization channel becomes dominant. To give a rough idea why inclusion of this channel is important we note that, e.g. at 500 keV the total ionization cross section is expected to be at least three orders of magnitude larger than the electron-transfer cross section.

Presently, a part of the ionization flux goes to the electron-transfer channel.

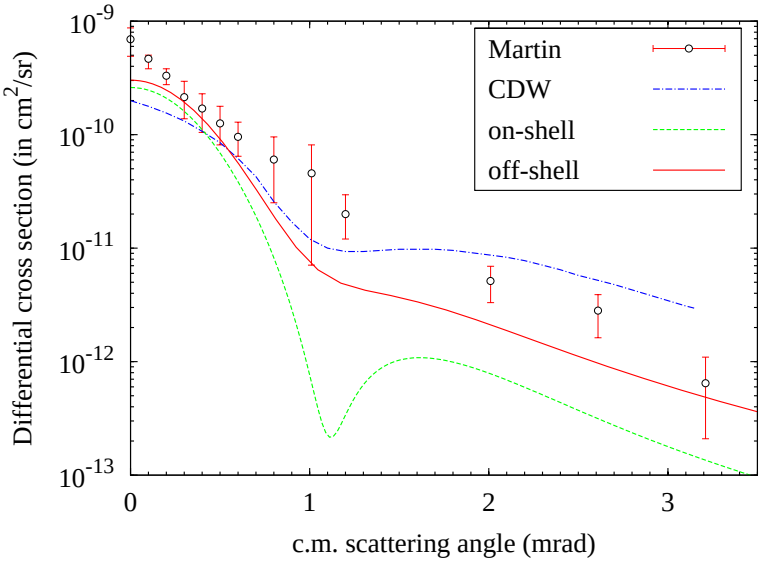

Figure 3.5: Differential cross sections for electron capture in $p + \mathrm{H}(1s)$ collisions at 25 keV. The symbols indicate experimental measurements of Martin et al. [115] while the lines show the present on-shell and off-shell results and the CDW calculations of [116].

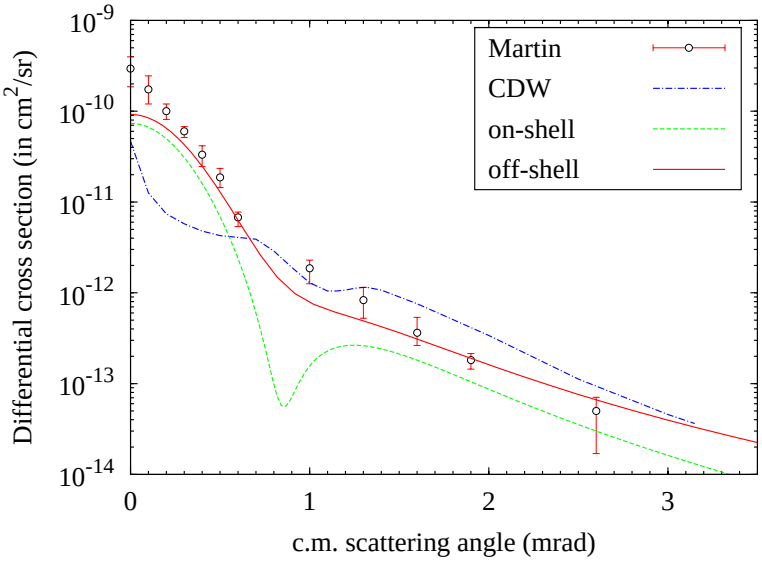

Figure 3.6: The same as in Fig. 3.5 but for 60 keV.

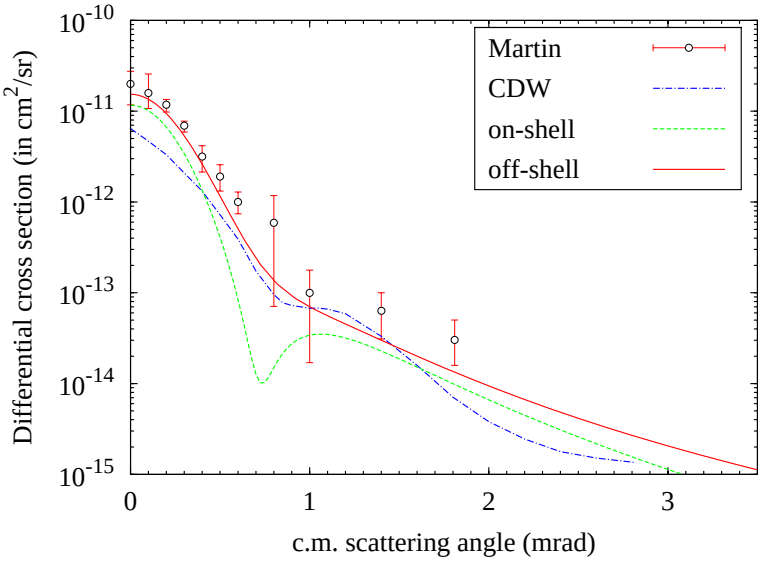

Figure 3.7: The same as in Fig. 3.5 but for 125 keV.

The differential cross sections for electron capture at 25, 60 and 125 keV are shown in Figs. 3.5-3.7, respectively, and compared with those from CDW calculations [116] and experimental measurements of Martin et al. [115]. It appears that our approach leads, on the whole, to a more realistic scattering amplitude, and consequently to a better reproduction of the experimental data.

We have also calculated total elastic-scattering cross sections for antiproton collisions with H($1s$). These are shown in Table 3.2 together with the relative contribution of the off-shell effects. Also shown in the table is the ratio of the total elastic cross sections of proton and antiproton on H($1s$). As we can see from the table, again the off-shell effects can both decrease and increase the cross section. The contribution can change from -15% at 100 eV to 20% at 20 keV. It is interesting to compare these results with corresponding results for elastic scattering of protons from Table 3.1. We can conclude that the off-shell effects are less significant for antiprotons than for protons. However, the off-shell contribution falls to a few-percent level at the MeV-region as it was the case for

protons. The table also suggests that there is practically no difference between the cross sections for proton and antiproton scattering above 200 keV per amu.

The total cross sections for elastic scattering of antiprotons are shown in Fig. 3.8 and compared with the corresponding results for protons. Above 200 keV there is practically no difference between the cross sections for the proton and antiproton. The off-shell effects for the antiproton are generally smaller than those for the elastic scattering of protons. The differential cross sections for scattering of antiprotons are shown in Fig. 3.9 also at 25, 60 and 125 keV.

Table 3.2: Relative contribution of the off-shell effects in $\overline{p} + \mathrm{H}(1s) \rightarrow \overline{p} + \mathrm{H}(1s)$ scattering.

Energy (keV)	$\sigma_{\alpha\alpha}$ (10^{-16} cm^2)	$\frac{\sigma_{\alpha\alpha}-\sigma^{\mathrm{on}}_{\alpha\alpha}}{\sigma^{\mathrm{on}}_{\alpha\alpha}}$ (%)	$\frac{\sigma^{p}_{\alpha\alpha}}{\sigma^{\overline{p}}_{\alpha\alpha}}$
0.1	9.44	-14.8	5.47
0.2	8.01	-11.4	5.96
0.5	6.28	-6.2	6.69
1	5.11	-1.5	5.83
2	4.05	3.5	4.49
5	2.84	10.9	3.20
10	2.06	16	1.96
20	1.41	19.9	1.49
50	0.753	19	1.26
100	0.432	15.5	1.10
200	0.234	10.9	1.03
500	0.0988	5.8	1.00
1000	0.0504	3.5	1.00
2000	0.0254	1.7	1.00

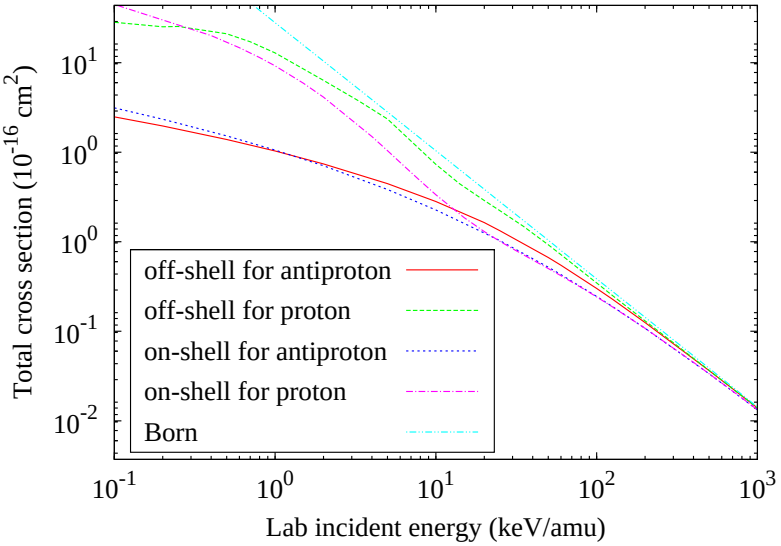

Figure 3.8: Total cross sections for $\overline{p}$ + H($1s$) $\rightarrow$ $\overline{p}$ + H($1s$) scattering. Present results for p + H($1s$) $\rightarrow$ p + H($1s$) scattering are also shown.

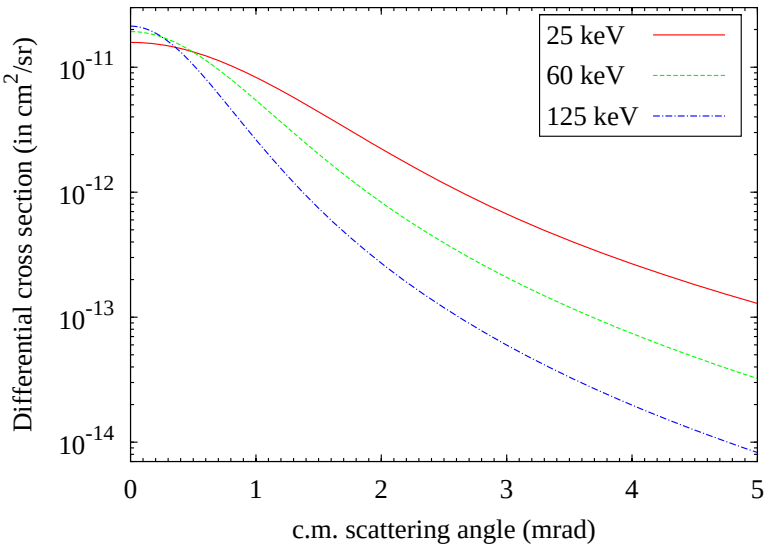

Figure 3.9: Differential cross sections for $\overline{p}$ + H($1s$) $\rightarrow$ $\overline{p}$ + H($1s$) scattering.

3.6 Extension of the method to the multichannel case

In previous sections we have investigated proton and antiproton scattering on atomic hydrogen with the assumption that the target remains in its ground state (1s) throughout the collision. For this simplified, however approximate case, we have practically demonstrated that the direct solution of the emerging Lippmann-Schwinger integral equations is a feasible task. Also, symmetry properties of the 1s-1s transition amplitudes allowed us to reduce the dimensionality of these equations. From comparison of calculated electron-capture cross sections with the experiment it became clear that to achieve better agreement it is important to include ionization channels. The inclusion of ionization requires a multichannel treatment of the problem. Let us explore the possibility to extend the direct method to the multichannel case. In contrast to the just considered two-channel case, in the multichannel case the general transition amplitudes $T_{\gamma'\gamma}(\boldsymbol{q}_{\gamma'}, \boldsymbol{q}_{\gamma})$ (the same is applicable for $V_{\gamma'\gamma}(\boldsymbol{q}_{\gamma'}, \boldsymbol{q}_{\gamma})$) depend on the azimuthal angle φ of the projectile in the initial and final states. The φ-dependance can, however, be singled out as a phase factor

$$T_{\gamma'\gamma}(\boldsymbol{q}_{\gamma'}, \boldsymbol{q}_{\gamma}) = \tilde{T}_{\gamma'\gamma}(\boldsymbol{q}_{\gamma'}, \boldsymbol{q}_{\gamma}; p_{\perp}) \exp(i\Delta\varphi_p), \tag{3.27}$$

where $\Delta m = m - m'$, $m(m')$ is the magnetic quantum number of the active electron in the $\gamma(\gamma')$ channel, φ_p is the azimuthal angle of the the momentum transfer vector $\boldsymbol{p} = \boldsymbol{q}_{\gamma} - \boldsymbol{q}_{\gamma'}$. In some approaches, like the first Born and distorted wave perturbative models, this factor is irrelevant in calculations of integrated cross sections, and therefore can be dropped. Here it is not possible. The phase of the kernel of Eq. (2.20) is a complicated function

$$\varphi_p = \arctan\left(\frac{q_{\gamma''}\sin\varphi''\sin\theta'' - q_{\gamma'}\sin\varphi'\sin\theta'}{q_{\gamma''}\cos\varphi''\sin\theta'' - q_{\gamma'}\cos\varphi'\sin\theta'}\right) \tag{3.28}$$

and it is not periodic with respect to the intermediate φ''. This fact does not allow us to reduce the dimension (associated with the azimuthal angle φ) of the three-dimensional integral equations (2.20) as it is done previously for the two-channel case. Consequently, the direct solution of Eq. (2.20) requires discretization of all spatial variables. The complexity of the problem drastically increases and this is especially the case when many channels are included. Let us calculate the storage requirement for the matrix emerging from discretization of Eq. (2.20). Denoting the number of channels with N_{ch} and the number of points in the q, θ and ϕ quadratures with N_q, N_θ and N_φ, respectively, the total storage (bytes) can be estimated to be in the order of $8(N_{ch}N_qN_\theta N_\varphi)^2$. From our experience with the two-channel case the convergent results can be obtained with $N_q = 100$, $N_\theta = 200$ and $N_\varphi = 30$ at least. For the full treatment of the problem at least thousand channels needs to be coupled. With this the required memory storage becomes well beyond currently available. To overcome the memory problem we have applied the iterative method using the Pade approximants for the solution of Eq. (2.20). However, the Padé method failed below 50 keV where the scattering potential of the target is much larger than the incident projectile energy. In addition to the constraints associated with memory requirements there is also a problem with p^{-2} singularities in effective potentials for some transitions. These singularities must be somehow handled in order to prevent ill-conditioning in the emerging matrix equation. In order to overcome these difficulties we have developed an alternative approach to ion-atom collisions which will be described in the next chapter.

3.7 Chapter summary

In this chapter we have investigated proton and antiproton collisions with atomic hydrogen using the atomic-orbital close-coupling method. To simplify the problem and make calculations feasible we constructed the total scattering wave function using only the ground states of atomic hydrogen in the direct and rearrangement channels. The method leads to coupled three-dimensional momentum-space integral equations for the off-shell scattering amplitudes. Symmetry properties of the transition amplitudes allowed us to reduce the dimensionality of these equations. The resulting two-dimensional equations are solved directly without partial-wave expansion or any other transformation scheme. We have presented the total and differential cross sections for electron transfer in proton collisions with the ground-state of atomic hydrogen. The contribution of off-shell effects is fully taken into account and shown to be significant. We find that the off-shell effects can both increase and reduce the cross sections substantially depending on energy. At high energies as much as a half of the total electron-transfer cross section comes from the off-shell effects. This contradicts classical and iterative estimates which predict the off-shell effects to be non-essential. The significance of the off-shell effects in elastic scattering of protons falls with increasing energy to the estimated levels. The calculated cross section results agree well with experiment over a wide energy range. The total and differential cross sections for elastic scattering of antiprotons are also calculated and compared with the corresponding results for protons. Above 200 keV there is practically no difference between the cross sections for the proton and antiproton. The off-shell effects for the antiproton are generally smaller than those for the elastic scattering of protons.

The present method which is based on fully quantal non-partial-wave and

fully off-shell formulation of the atomic-orbital close-coupling can be developed into a multi-channel wide-energy approach to ion-atom collisions. Such an extension of the method, which effectively includes the ionization channel through a square-integrable pseudo-basis, can be considered when the adequate computational resources become available. Meanwhile for the full treatment of ion-atom collisions we use our recently developed impact-parameter transformation approach which is discussed in the next chapter.

Chapter 4

Transformation of Lippmann-Schwinger integral equations into impact-parameter representation

In this chapter the momentum-space coupled-channel Lippmann-Schwinger equations (2.20) will be transformed into the impact-parameter representation. However, despite the usage of the impact-parameter representation no semiclassical limitations will be imposed on the relative motion of the heavy particles. The latter will be treated fully quantum-mechanically. The relative motion will not be limited to a constant velocity. We emphasise that the impact-parameter representation as used in the present approach is merely a transformation from the momentum-transfer space into the mathematically equivalent impact-parameter space. The momentum-transfer (with or without partial-wave expansion) and impact-parameter representations are complementary and, in principle, transform into each other without any limitations or approximations (see Refs. [117–120] and references therein). We do, however, assume in the present work that the main contribution comes when the heavy projectile is scattered into small angles, which is indeed the case.

Once the scattering equations in impact-parameter space are derived, we

next turn to their practical applications. We will consider antiproton scattering on atomic hydrogen and helium. The full multichannel treatment of these problems, capable of describing the target excitation and ionization, require knowledge of the target structure. For the target description we follow the ideas of the convergent close coupling (CCC) method. The CCC method has demonstrated great success in dealing with light projectiles in examples of collisions of electrons [77] and positrons [75] with hydrogen and positrons with helium [76, 121].

The main idea behind CCC is to expand the total wave function using a sufficiently large orthogonal Laguerre basis in order to obtain converged amplitudes for the possible atomic excitation and ionization processes. The target atom Hamiltonian is diagonalized in this basis yielding both negative- and positive-energy pseudostates. For the hydrogen target this procedure is straightforward. In the case of the two-electron target of helium we use the configuration-interaction approach of Fursa and Bray [122] and assume that one of the electrons (which is not involved in single ionization) is allowed to occupy a limited number of orbitals while the other is free to be in any orbital necessary for convergence of the final results. When the inner electron is limited to just the 1s orbital of He^+ we have a frozen-core (FC) approximation, and when several inner orbitals are allowed we have a multiconfiguration (MC) description. We emphasize here that both FC and MC descriptions of the target explicitly account for the electron correlation effects. With increasing basis size the negative-energy pseudo states converge to the true discrete eigenstates, while the positive-energy states provide an increasingly dense discretization of the continuum. Convergence in the cross sections of interest, is obtained by simply increasing the basis size.

Lastly, we describe how the fully and partially differential cross sections in

the variables of both the projectile and the ejected electron are derived from the T matrix elements.

4.1 Impact-parameter transformation

In previous chapters we have discussed a few methods that may be used to solve the scattering equation (2.20). It was mentioned that the partial wave expansion method which is optimal for processes with light projectiles, in the case of heavy projectiles (ion-atom collisions), becomes inefficient as several thousand partial waves can contribute to the solution of the problem. The direct method (Chapter 3 and also Refs. [99–101]) of solving three-dimensional equations without recourse to partial-wave expansions also turned out to be inefficient when many channels are coupled. In this chapter, we use the impact-parameter representation which is widely used for solving problems of this kind in atomic physics. We write the momentum transfer $\boldsymbol{p} = \boldsymbol{q}_\gamma - \boldsymbol{q}_{\gamma'}$ as a sum of two components

$$\boldsymbol{p} = \boldsymbol{p}_\perp + \boldsymbol{p}_\parallel, \tag{4.1}$$

where $\boldsymbol{p}_\perp$ is the transverse component of the momentum transfer perpendicular to the direction of the projectile velocity $\boldsymbol{v}$ which we set to be along the z-axis. For convenience, below we write the scattering amplitudes and effective potentials as functions of the transverse components of the momentum transfer $\boldsymbol{p}_\perp$. They also depend on $\boldsymbol{p}_\parallel$ which we show through arguments $q_{\gamma'}$ and q_γ. We emphasize that we do not assume that the amplitudes and effective potentials depend only on $\boldsymbol{p}_\perp$. From all the effective potentials and amplitudes one can single out the phase factor $\exp(i\Delta m\varphi_{p_\perp})$:

$$V_{\gamma'\gamma}(\boldsymbol{q}_{\gamma'}, \boldsymbol{q}_\gamma) = V_{\gamma'\gamma}(q_{\gamma'}, q_\gamma; \boldsymbol{p}_\perp) = \tilde{V}_{\gamma'\gamma}(q_{\gamma'}, q_\gamma; p_\perp) \exp(i\Delta m\varphi_{p_\perp}), \tag{4.2}$$

$$T_{\gamma'\gamma}(\boldsymbol{q}_{\gamma'}, \boldsymbol{q}_\gamma) = T_{\gamma'\gamma}(q_{\gamma'}, q_\gamma; \boldsymbol{p}_\perp) = \tilde{T}_{\gamma'\gamma}(q_{\gamma'}, q_\gamma; p_\perp) \exp(i\Delta m\varphi_{p_\perp}), \tag{4.3}$$

where $\Delta m = m - m'$, $m(m')$ is the magnetic quantum number of the active electron in the $\gamma(\gamma')$ channel, and $\varphi_{p_\perp}$ is the azimuthal angle of the vector $\boldsymbol{p}_\perp$ in the plane perpendicular to the direction of $\boldsymbol{v}_P$.

Transformation into the impact-parameter space is realized via the following relationship

$$\mathcal{T}_{\gamma'\gamma}(q_{\gamma'}, q_\gamma; \boldsymbol{b}) = \frac{1}{2\pi} \int d\boldsymbol{p}_\perp e^{i\boldsymbol{p}_\perp \boldsymbol{b}} T_{\gamma'\gamma}(q_{\gamma'}, q_\gamma; \boldsymbol{p}_\perp) = \tilde{\mathcal{T}}_{\gamma'\gamma}(q_{\gamma'}, q_\gamma; b) e^{i\Delta m \varphi_b}, \quad (4.4)$$

where

$$\tilde{\mathcal{T}}_{\gamma'\gamma}(q_{\gamma'}, q_\gamma; b) = (-i)^{\Delta m} \int_0^\infty dp_\perp p_\perp \tilde{T}_{\gamma'\gamma}(q_{\gamma'}, q_\gamma; p_\perp) J_{\Delta m}(p_\perp b), \quad (4.5)$$

with $J_{\Delta m}$ being the Bessel function and φ_b is the azimuthal angle determining the position of $\boldsymbol{b}$ in the plane perpendicular to $\boldsymbol{v}$. The inverse transformation is performed according to

$$\begin{aligned} T_{\gamma'\gamma}(q_{\gamma'}, q_\gamma; \boldsymbol{p}_\perp) &= \frac{1}{2\pi} \int d\boldsymbol{b} e^{i\boldsymbol{p}_\perp \boldsymbol{b}} \mathcal{T}_{\gamma'\gamma}(q_{\gamma'}, q_\gamma; \boldsymbol{b}) \\ &= i^{\Delta m} e^{i\Delta m \varphi_p} \int_0^\infty dbb \tilde{\mathcal{T}}_{\gamma'\gamma}(q_{\gamma'}, q_\gamma; b) J_{\Delta m}(p_\perp b). \end{aligned} \quad (4.6)$$

Similar relationships can be written for the effective potentials in the impact-parameter representation $\mathcal{V}_{\gamma'\gamma}(q_{\gamma'}, q_\gamma; \boldsymbol{b})$ in terms of the momentum space effective potentials $V_{\gamma'\gamma}(q_{\gamma'}, q_\gamma; \boldsymbol{p}_\perp)$. With these definitions transformation of the left-hand side and the first term of the right-hand side of our momentum space coupled channel equations (2.20) is straightforward. Transformation of the integral term is more involved. This term can be written as

$$\sum_{\gamma''}^{N_\alpha + N_\beta} \int_0^\infty \frac{dq_{\gamma''} q_{\gamma''}^2 G_{\gamma''}(q_{\gamma''}^2)}{(2\pi)^3} \int d\Omega_{\boldsymbol{q}_{\gamma''}} V_{\gamma'\gamma''}(q_{\gamma'}, q_{\gamma''}; \boldsymbol{p}''_\perp) T_{\gamma''\gamma}(q_{\gamma''}, q_\gamma; \boldsymbol{p}'_\perp), \quad (4.7)$$

where $\boldsymbol{p}'_\perp$ and $\boldsymbol{p}''_\perp$ are the transverse components of vectors $\boldsymbol{p}' = \boldsymbol{q}_\gamma - \boldsymbol{q}_{\gamma''}$ and $\boldsymbol{p}'' = \boldsymbol{q}_{\gamma''} - \boldsymbol{q}_{\gamma'}$, respectively. Since $\boldsymbol{p}'_\perp + \boldsymbol{p}''_\perp = \boldsymbol{p}_\perp$ we denote the integral over directions of the momentum $\boldsymbol{q}_{\gamma''}$ as

$$M_{\gamma'\gamma''}(q_{\gamma'}, q_{\gamma''}, q_\gamma; \boldsymbol{p}_\perp) = \int d\Omega_{\boldsymbol{q}_{\gamma''}} V_{\gamma'\gamma''}(q_{\gamma'}, q_{\gamma''}; \boldsymbol{p}''_\perp) T_{\gamma''\gamma}(q_{\gamma''}, q_\gamma; \boldsymbol{p}'_\perp). \quad (4.8)$$

Eq. (4.8) has a similar structure as Eq. (17) of Avakov et al. [123]. Therefore, in order to transform the integral (4.8) into the impact-parameter representation we follow Ref. [123]. Using transformation (4.6) for amplitudes $V_{\gamma'\gamma''}(\boldsymbol{q}_{\gamma'}, \boldsymbol{q}_{\gamma''})$ and $T_{\gamma''\gamma}(\boldsymbol{q}_{\gamma''}, \boldsymbol{q}_{\gamma})$, we can rewrite the integral term as

$$M_{\gamma'\gamma''}(q_{\gamma'}, q_{\gamma''}, q_{\gamma}; \boldsymbol{p}_\perp) = \int d\Omega_{\boldsymbol{q}_{\gamma''}} \frac{1}{2\pi} \int d\boldsymbol{b}_1 e^{i\boldsymbol{p}''_\perp \boldsymbol{b}_1} \mathcal{V}_{\gamma'\gamma''}(q_{\gamma'}, q_{\gamma''}; \boldsymbol{b}_1) \times \frac{1}{2\pi} \int d\boldsymbol{b}_2 e^{i\boldsymbol{p}'_\perp \boldsymbol{b}_2} \mathcal{T}_{\gamma''\gamma}(q_{\gamma''}, q_{\gamma}; \boldsymbol{b}_2). \tag{4.9}$$

We can write

$$e^{i\boldsymbol{p}''_\perp \boldsymbol{b}_1 + i\boldsymbol{p}'_\perp \boldsymbol{b}_2} = e^{i\boldsymbol{q}_\gamma \boldsymbol{b}_2 - i\boldsymbol{q}_{\gamma'} \boldsymbol{b}_1} e^{i\boldsymbol{q}_{\gamma''}(\boldsymbol{b}_1 - \boldsymbol{b}_2)}. \tag{4.10}$$

Therefore by changing the order of integration and taking into account (4.10), we can write Eq. (4.9) as

$$M_{\gamma'\gamma''}(q_{\gamma'}, q_{\gamma''}, q_{\gamma}; \boldsymbol{p}_\perp) = \frac{1}{(2\pi)^2} \int d\boldsymbol{b}_1 \int d\boldsymbol{b}_2 e^{i\boldsymbol{q}_\gamma \boldsymbol{b}_2 - i\boldsymbol{q}_{\gamma'} \boldsymbol{b}_1} \mathcal{V}_{\gamma'\gamma''}(q_{\gamma'}, q_{\gamma''}; \boldsymbol{b}_1) \times \mathcal{T}_{\gamma''\gamma}(q_{\gamma''}, q_{\gamma}; \boldsymbol{b}_2) \int d\Omega_{\boldsymbol{q}_{\gamma''}} e^{i\boldsymbol{q}_{\gamma''}(\boldsymbol{b}_1 - \boldsymbol{b}_2)}. \tag{4.11}$$

Generally speaking, we can write

$$I(\boldsymbol{b}) = \int d\Omega_{\boldsymbol{q}} e^{i\boldsymbol{q}\boldsymbol{b}} = \int_0^\pi d\theta_{\boldsymbol{q}} \sin\theta_{\boldsymbol{q}} \int_0^{2\pi} d\varphi_{\boldsymbol{q}} e^{iqb\sin\theta_{\boldsymbol{q}}\cos\varphi_{\boldsymbol{q}}} = 2\pi \int_0^\pi d\theta_{\boldsymbol{q}} \sin\theta_{\boldsymbol{q}} J_0(qb\sin\theta_{\boldsymbol{q}}) = 4\pi \int_0^{\pi/2} d\theta_{\boldsymbol{q}} \sin\theta_{\boldsymbol{q}} J_0(qb\sin\theta_{\boldsymbol{q}}), \tag{4.12}$$

where $J_0(x)$ is the zeroth order Bessel function of the first kind. No approximation have been made so far. Now, assuming that the major contribution to the amplitude comes from small scattering angles we set $\sin\theta_{\boldsymbol{q}} \approx \theta_{\boldsymbol{q}}$ and after change of variable $q_\perp = q\theta_{\boldsymbol{q}}$ integral $I(\boldsymbol{b})$ becomes

$$I(\boldsymbol{b}) \approx \frac{4\pi}{q^2} \int_0^{q\pi/2} dq_\perp q_\perp J_0(\boldsymbol{b}\boldsymbol{q}_\perp). \tag{4.13}$$

Since in collisions with a heavy projectile the upper limit of integration, $q\pi/2$ is very large, we can approximate

$$I(\boldsymbol{b}) \approx \frac{4\pi}{q^2} \int_0^\infty dq_\perp q_\perp J_0(\boldsymbol{b}\boldsymbol{q}_\perp) = \frac{4\pi^2}{q^2} \delta(\boldsymbol{b}). \tag{4.14}$$

Such approximation is justified in the electron transfer problem in ion-atom collisions [123, 124]. A detailed test of validity of this approximation will be given in the next chapter where antiproton-hydrogen scattering is considered. Eq. (4.14) allows us to perform one integration in Eq.(4.11) and reduce the integral term to

$$M_{\gamma'\gamma''}(q_{\gamma'}, q_{\gamma''}, q_\gamma; \boldsymbol{p}_\perp) = \frac{1}{q_{\gamma''}^2} \int d\boldsymbol{b} e^{i\boldsymbol{p}_\perp \boldsymbol{b}} \mathcal{V}_{\gamma'\gamma''}(q_{\gamma'}, q_{\gamma''}; \boldsymbol{b}) \mathcal{T}_{\gamma''\gamma}(q_{\gamma''}, q_\gamma; \boldsymbol{b}). \quad (4.15)$$

From (4.15) it follows that in the impact parameter space the integral term becomes

$$\tilde{\mathcal{M}}_{\gamma'\gamma}(q_{\gamma'}, q_{\gamma''}, q_\gamma; b) = \frac{2\pi}{q_{\gamma''}^2} \tilde{\mathcal{V}}_{\gamma'\gamma}(q_{\gamma'}, q_{\gamma''}; b) \tilde{\mathcal{T}}_{\gamma'\gamma}(q_{\gamma''}, q_\gamma; b), \quad (4.16)$$

where

$$\tilde{\mathcal{M}}_{\gamma'\gamma}(q_{\gamma'}, q_{\gamma''}, q_\gamma; b) = (-i)^{\Delta m} \int_0^\infty dp_\perp p_\perp \tilde{M}_{\gamma'\gamma}(q_{\gamma'}, q_{\gamma''}, q_\gamma; p_\perp) J_{\Delta m}(p_\perp b) \quad (4.17)$$

and

$$M_{\gamma'\gamma}(q_{\gamma'}, q_{\gamma''}, q_\gamma; \boldsymbol{p}_\perp) = \tilde{M}_{\gamma'\gamma}(q_{\gamma'}, q_{\gamma''}, q_\gamma; p_\perp) \exp(i\Delta m \varphi_{p_\perp}). \quad (4.18)$$

With these we obtain the impact-parameter form of equation (2.20)

$$\begin{aligned} \tilde{\mathcal{T}}_{\gamma'\gamma}(q_{\gamma'}, q_\gamma; b) =& \tilde{\mathcal{V}}_{\gamma'\gamma}(q_{\gamma'}, q_\gamma; b) \\ &+ \frac{1}{(2\pi)^2} \sum_{\gamma''}^{N_\alpha + N_\beta} \int_0^\infty dq_{\gamma''} \tilde{\mathcal{V}}_{\gamma'\gamma''}(q_{\gamma'}, q_{\gamma''}; b) G_{\gamma''}(q_{\gamma''}^2) \tilde{\mathcal{T}}_{\gamma''\gamma}(q_{\gamma''}, q_\gamma; b). \end{aligned} \quad (4.19)$$

This set takes into account the off-the-energy-shell effects through the integration over intermediate particle's momentum $q_{\gamma''}$. A similar equation but for potential scattering was given by Kamal and Chavda [120]. At sufficiently high energies of the projectile, the interaction between the antiproton and the target proton cannot markedly change the incident velocity of the projectile. In the literature this approximation is known as a constant velocity approximation and

widely used in various close-coupling approaches to ion-atom collisions [71] for the purpose of transforming the time-independent Schrödinger equation for the scattering wave function into an approximate time-dependent equation. In our case, this approximation corresponds to replacing the Green's function G in Eq. (4.19) by the delta function

$$\begin{aligned} G_{\gamma''}(q_{\gamma''}^2) &= (E + i0 - \frac{q_{\gamma''}^2}{2M_{\gamma''}} - \epsilon_{\gamma''})^{-1} \\ &\approx -\frac{i\pi M_{\gamma''}}{\sqrt{2M_{\gamma''}(E-\epsilon_{\gamma''})}}\delta\left(q_{\gamma''} - \sqrt{2M_{\gamma''}(E-\epsilon_{\gamma''})}\right). \end{aligned} \tag{4.20}$$

If we integrate in the right-hand side of (4.19) over $q_{\gamma''}$ using Eq. (4.20) and taking $q_{\gamma''} = M_{\gamma''}v_P$, we get

$$\tilde{\mathcal{T}}_{\gamma'\gamma}(q_{\gamma'}, q_\gamma; b) = \tilde{\mathcal{V}}_{\gamma'\gamma}(q_{\gamma'}, q_\gamma; b) - \frac{i}{4\pi v_P}\sum_{\gamma''}^{N_\alpha^o+N_\beta^o} \tilde{\mathcal{V}}_{\gamma'\gamma''}(q_{\gamma'}, q_{\gamma''}; b)\tilde{\mathcal{T}}_{\gamma''\gamma}(q_{\gamma''}, q_\gamma; b), \tag{4.21}$$

where N_α^o and N_β^o are the number of open states in channels α and β, respectively. In comparison with the original equation (4.19) the latter requires significantly less memory and time to solve as it avoids working with huge matrices. Results obtained for antiproton-hydrogen scattering using the on-shell approximation have been given in Ref. [125]. As it will be shown later this on-shell approximation turns out to be reliable only above 30 keV.

In practice, in order to obtain reliable fully off-shell results one has to couple as many as a few hundred channels, and consequently the numerical solution of (4.19) requires a huge amount of computer resources. By introducing the $\mathcal{K}$-matrix formulation which deals with pure real arithmetic we can reduce the memory requirements almost twice. If we let

$$\tilde{\mathcal{K}}_{\gamma'\gamma}(q_{\gamma'}, q_\gamma; b) = \sum_{\gamma''}^{N_\alpha^o+N_\beta^o} \tilde{\mathcal{T}}_{\gamma'\gamma''}(q_{\gamma'}, q_{\gamma''}; b)(\delta_{\gamma''\gamma} + i\pi q_{\gamma''}\tilde{\mathcal{K}}_{\gamma'\gamma}(q_{\gamma'}, q_\gamma; b)) \tag{4.22}$$

Eq. (4.19) transforms to the following set of equations for the K-matrix amplitudes [77]

$$\tilde{\mathcal{K}}_{\gamma'\gamma}(q_{\gamma'}, q_\gamma; b) = \tilde{\mathcal{V}}_{\gamma'\gamma}(q_{\gamma'}, q_\gamma; b) + \frac{1}{(2\pi)^2} \sum_{\gamma''}^{N_\alpha+N_\beta} \mathrm{PV} \int_0^\infty dq_{\gamma''} \frac{\tilde{\mathcal{V}}_{\gamma'\gamma''}(q_{\gamma'}, q_{\gamma''}; b)}{E - q_{\gamma''}^2/2M_{\gamma''} - \epsilon_{\gamma''}} \tilde{\mathcal{K}}_{\gamma''\gamma}(q_{\gamma''}, q_\gamma; b), \tag{4.23}$$

where the symbol PV indicates that the integral is of the principal value type.

Thus we have derived the scattering equations in the impact parameter space for the full multichannel off-shell treatment of the problem. We will demonstrate its practical application by considering the scattering of antiprotons on different targets. For simplicity we do not consider the possibility of antiproton binding since above keV energies, the energy region of our interest, this effect is negligible [3]. Thus we consider only the direct scattering of the projectile. In this case the sum in Eq. (4.23) involves only pseudostates of the target, i.e. $N_\beta = 0$.

4.2 Impact parameter representation of effective potentials: Direct transition

Since for antiproton-atom collisions we have only the direct scattering channels, to simplify notations in the next expressions let us redefine the position vector of the projectile with capital letter $\boldsymbol{R}$. Small letters $\boldsymbol{r}_i$ will be reserved for spatial coordinates of the target electrons. Direct transition elements are derived from (2.22)

$$\begin{aligned} V_{\alpha'\alpha}(q_{\alpha'}, q_\alpha; \boldsymbol{p}) &\equiv \langle \boldsymbol{q}_{\alpha'} | \langle \psi_{\alpha'} | U_{\alpha'\alpha} | \psi_\alpha \rangle_{\boldsymbol{R}} | \boldsymbol{q}_\alpha \rangle \\ &= \int d\boldsymbol{R} e^{-i\boldsymbol{q}_{\alpha'}\boldsymbol{R}} \langle \psi_{\alpha'} | U_{\alpha'\alpha} | \psi_\alpha \rangle_{\boldsymbol{R}} e^{i\boldsymbol{q}_\alpha \boldsymbol{R}} \\ &= \int d\boldsymbol{R} e^{i\boldsymbol{p}\boldsymbol{R}} I_{\alpha'\alpha}(\boldsymbol{R}), \end{aligned} \tag{4.24}$$

where the quantity $\boldsymbol{p} = \boldsymbol{q}_\alpha - \boldsymbol{q}_{\alpha'}$ is the momentum transfer and the integral $I_{\alpha'\alpha}(\boldsymbol{R})$ is defined as

$$I_{\alpha'\alpha}(\boldsymbol{R}) = \langle \psi_{\alpha'} | U_{\alpha'\alpha} | \psi_\alpha \rangle_{\boldsymbol{R}}. \tag{4.25}$$

Effective potentials in the impact parameter representation can be obtained from Eq. (4.24) after some algebraic manipulations. The vector $\boldsymbol{R}$ in Eq. (4.24) can be written in terms of the impact parameter $\boldsymbol{b}$ and its z component

$$\boldsymbol{R} = \boldsymbol{b} + \boldsymbol{z}, \tag{4.26}$$

where $\boldsymbol{b}$ is perpendicular to $\boldsymbol{z} = z\boldsymbol{v}/v$. After decomposing the momentum transfer into its parallel and perpendicular parts the effective potentials can be written as

$$V_{\alpha'\alpha}(q_{\alpha'}, q_\alpha; \boldsymbol{p}) = \frac{1}{2\pi} \int d\boldsymbol{b} \exp(i\boldsymbol{p}_\perp \boldsymbol{b}) 2\pi \int_{-\infty}^{\infty} dz \exp(ip_\parallel z) I_{\alpha'\alpha}(\boldsymbol{b} + \boldsymbol{z}), \tag{4.27}$$

Using Eq. (4.6) we can extract the effective potential in the impact parameter representation

$$\mathcal{V}_{\alpha'\alpha}(q_{\alpha'}, q_\alpha; \boldsymbol{b}) = 2\pi \int_{-\infty}^{\infty} dz \exp(ip_\parallel z) I_{\alpha'\alpha}(\boldsymbol{b} + \boldsymbol{z}), \tag{4.28}$$

where in the general off-shell case the parallel component of momentum transfer is $p_\parallel = q_\alpha - q_{\alpha'} \cos(\theta) \approx q_\alpha - q_{\alpha'}$. In the on-shell case it reduces to a familiar form

$$p_\parallel = \frac{\epsilon_{\alpha'} - \epsilon_\alpha}{v_P}, \tag{4.29}$$

due to $q_{\alpha'} \approx q_\alpha = M_\alpha v_P$. One can see from Eq. (4.28) that the effective potential in the impact parameter representation is just the Fourier transform of the integral $I_{\alpha'\alpha}(\boldsymbol{b} + \boldsymbol{z})$.

The integral $I_{\alpha'\alpha}$ is different for each collision system. Its calculation requires the knowledge of the structure of the considered target. In the present work we

will consider scattering of antiprotons on atomic hydrogen and helium. First we give our approach to generating the pseudostates for these targets. Then we derive $I_{\alpha'\alpha}$ for each of the collision systems.

4.3 Hydrogen structure

For atomic hydrogen the pseudostates $\psi_\alpha(\boldsymbol{r}) \equiv \psi_{nlm}(\boldsymbol{r})$[1] can be written as

$$\psi_{nlm}(\boldsymbol{r}) = R_{nl}(r)Y_{lm}(\hat{r}), \tag{4.30}$$

where

$$R_{nl}(r) = \sum_{k=1}^{N_l} B^l_{nk}\phi_{kl}(r), \tag{4.31}$$

and the basis $\phi_{kl}(r)$ is made of the orthogonal Laguerre functions

$$\phi_{kl}(r) = N_{kl}(2\lambda_l r)^{l+1}e^{-\lambda_l r}L^{2l+2}_{k-1}(2\lambda_l r), \tag{4.32}$$

with

$$N_{kl} = \left[\frac{2\lambda_l(k-1)!}{(2l+1+k)!}\right]^{1/2}. \tag{4.33}$$

Here $L^{2l+2}_{k-1}(2\lambda_l r)$ are the associated Laguerre polynomials. Expansion coefficients B^l_{nk} are found by diagonalizing the target Hamiltonian ($H_T\psi_\alpha = \epsilon_\alpha\psi_\alpha$). For the hydrogen target the Hamiltonian is

$$H_T = -\frac{1}{2}\nabla^2_r - \frac{1}{r}. \tag{4.34}$$

The diagonalization procedure yields negative and positive energy levels. The results, in principal, do not depend on characteristic fall-off parameter λ_l when converged, however the rate of convergence does. For this reason it will be chosen

[1] n, l and m are, respectively, principal, orbital and magnetic quantum numbers of the state α

on the basis of practical convenience. We will return to the specific choice of parameter λ_l in the next chapter. As the number of pseudostates in each target symmetry increases (with the fixed value of λ_l) the lowest bound states of H become closer to their eigenstates while the positive energy pseudostates yield an increasingly denser discretization of the continuum. This will also help to span a wider continuum range.

Figure 4.1 displays the electron energy levels for atomic hydrogen.

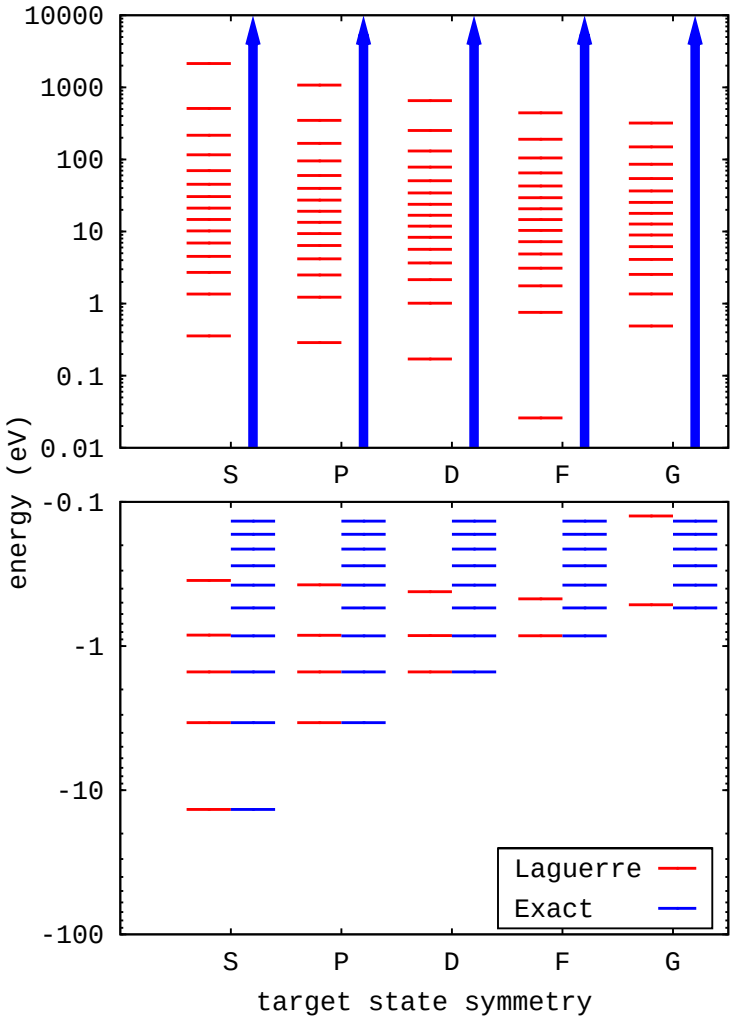

Figure 4.1: Energy levels of atomic hydrogen obtained using the orthogonal Laggerre basis. Exact eigenenergies for $n \leq 10$ are also shown for comparison.

4.4 Direct transition amplitudes for antiproton-hydrogen collisions

Having generated the hydrogen pseudostates we can proceed to derivation of $\mathcal{V}_{\alpha'\alpha}(q_{\alpha'}, q_\alpha; \boldsymbol{b})$ for antiproton-hydrogen collisions according to (4.28). Here inte-

gral $I_{\alpha'\alpha}$ is expressed as follows

$$I_{\alpha'\alpha}(\boldsymbol{R}) \equiv \langle\psi_{\alpha'}|U_{\alpha'\alpha}|\psi_\alpha\rangle_{\boldsymbol{R}} = \int d\boldsymbol{r}\psi^*_{\alpha'}(\boldsymbol{r})\left(-\frac{1}{R}+\frac{1}{|\boldsymbol{R}-\boldsymbol{r}|}\right)\psi_\alpha(\boldsymbol{r}). \tag{4.35}$$

To perform the angular integration of Eq. (4.35) analytically we use the following expansion

$$-\frac{1}{R}+\frac{1}{|\boldsymbol{R}-\boldsymbol{r}|} = 4\pi\sum_{\lambda\mu}\frac{1}{2\lambda+1}\,\mathcal{U}_\lambda(R,r)Y^*_{\lambda\mu}(\widehat{\boldsymbol{R}})Y_{\lambda\mu}(\widehat{\boldsymbol{r}}), \tag{4.36}$$

where

$$\mathcal{U}_\lambda(R,r) = \begin{cases} -\dfrac{\delta_{\lambda 0}}{R}+\dfrac{R^\lambda}{r^{\lambda+1}} & \text{if} \quad R\le r, \\ -\dfrac{\delta_{\lambda 0}}{R}+\dfrac{r^\lambda}{R^{\lambda+1}} & \text{if} \quad R>r. \end{cases} \tag{4.37}$$

Taking hydrogen wave functions given in Eq. (4.30) we can write Eq. (4.35) as

$$\begin{aligned} I_{\alpha'\alpha}(\boldsymbol{R}) =& 4\pi\sum_{\lambda\mu}\frac{Y^*_{\lambda\mu}(\widehat{\boldsymbol{R}})}{2\lambda+1}\int_0^\infty dr r^2 R_{n_{\alpha'}l_{\alpha'}}(r)R_{n_\alpha l_\alpha}(r)\mathcal{U}_\lambda(R,r) \\ &\times\int d\widehat{\boldsymbol{r}}Y^*_{l_{\alpha'}m_{\alpha'}}(\widehat{\boldsymbol{r}})Y_{\lambda\mu}(\widehat{\boldsymbol{r}})Y_{l_\alpha m_\alpha}(\widehat{\boldsymbol{r}}). \end{aligned} \tag{4.38}$$

Here we can use the following formula for the spherical harmonics

$$\int d\widehat{\boldsymbol{r}}\,Y^*_{l_{\alpha'}m_{\alpha'}}(\widehat{\boldsymbol{r}})\,Y_{\lambda\mu}(\widehat{\boldsymbol{r}})\,Y_{l_\alpha m_\alpha}(\widehat{\boldsymbol{r}}) = \frac{1}{\sqrt{4\pi}}\frac{[\lambda]\,[l_\alpha]}{[l_{\alpha'}]}\,C^{l_{\alpha'}0}_{\lambda 0\, l_\alpha 0}\,C^{l_{\alpha'}m_{\alpha'}}_{\lambda\mu\, l_\alpha m_\alpha}, \tag{4.39}$$

where $[l]\equiv\sqrt{2l+1}$. This allows us to further reduce Eq. (4.38) to

$$\begin{aligned} I_{\alpha'\alpha}(\boldsymbol{R}) =& \sqrt{4\pi}\sum_{\lambda\mu}\frac{[l_\alpha]}{[\lambda][l_{\alpha'}]}\,C^{l_{\alpha'}0}_{\lambda 0\, l_\alpha 0}\,C^{l_{\alpha'}m_{\alpha'}}_{\lambda\mu\, l_\alpha m_\alpha}\,Y^*_{\lambda\mu}(\widehat{\boldsymbol{R}}) \\ &\times\int_0^\infty dr r^2 R_{n_{\alpha'}l_{\alpha'}}(r)R_{n_\alpha l_\alpha}(r)\mathcal{U}_\lambda(R,r). \end{aligned} \tag{4.40}$$

4.5 Helium structure

Generating pseudostates for the two-electron target of helium is not as easy as for the case of atomic hydrogen. The helium target Hamiltonian includes the

electron-electron correlation term in addition to the Coulomb interactions of both electrons with atomic nucleus

$$H_{\rm T} = -\frac{1}{2}\nabla_1^2 - \frac{1}{2}\nabla_2^2 - \frac{2}{r_1} - \frac{2}{r_2} + \frac{1}{|\boldsymbol{r}_1 - \boldsymbol{r}_2|}, \tag{4.41}$$

where r_1 and r_2 are the coordinates of the electrons. Because of the electron-electron correlation term, diagonalization of the Hamiltonian is a complicated process with no analytical solution.

Since the total electronic spin of the helium is conserved during the collision, we only need to deal with the spatial part of target wave functions ψ_α. In addition, since only one electron can be excited, we may use the hydrogenic notation nlm to label the quantum state α. To construct those wave functions we use the configuration interaction (CI) approach of Fursa and Bray [122] (see Appendix A), namely,

$$\psi_\alpha(\boldsymbol{r}_1, \boldsymbol{r}_2) = \sum_{a,b} C^\alpha_{a,b} \phi_a(r_1)\phi_b(r_2) \left\{Y_{l_a}(\hat{r}_1) \otimes Y_{l_b}(\hat{r}_2)\right\}_{l_\alpha m_\alpha}. \tag{4.42}$$

Here $C^\alpha_{a,b}$ are the CI coefficients which are found by diagonalizing the target Hamiltonian (4.41). To ensure antisymmetry of the two-electron target states the following symmetry property is satisfied by CI coefficients:

$$C^\alpha_{a,b} = (-1)^{l_a + l_b - l_\alpha} C^\alpha_{b,a}. \tag{4.43}$$

Wavefunctions $\phi_a(r)$ in Eq. (4.42) are the one-electron orbitals which are used to build the two-electron basis. They are made of the orthogonal Laguerre functions (4.32). Lastly, the bipolar harmonics in (4.42) are defined through the spherical harmonics Y_{lm} as

$$\left\{Y_{l_a}(\hat{r}_1) \otimes Y_{l_b}(\hat{r}_2)\right\}_{l_\alpha m_\alpha} = \sum_{m_a m_b} C^{l_\alpha m_\alpha}_{l_a m_a l_b m_b} Y_{l_a m_a}(\hat{r}_1) Y_{l_b m_b}(\hat{r}_2),$$

where $C^{l_\alpha m_\alpha}_{l_a m_a l_b m_b}$ are Clebsch-Gordan coefficients.

Diagonalization of the target Hamiltonian $H_{\rm T}$ using the helium wave functions $\psi_\alpha(\boldsymbol{r}_1, \boldsymbol{r}_2)$ yields negative and positive energy states ϵ_α. In principle, if used in full, as it stands, the equation (4.42) can describe single and double excitation and ionization. Presently, for the purpose of describing single ionization we restrict the upper limit of one of the indices in Eq. (4.42) in order to prevent the inner electron from ejection. To be precise we include only $\{1s, 2s, 2p, 3s, 3p, 3d, 4s, 4p, 4d, 4f\}$ Laguerre orbitals (4.32) for the description of the inner electron excitations. In order to obtain the exact He^+ 1s orbital and accurately take into account the short-range electron-electron correlations in the ground and low-lying energy levels of He, the fall-off parameters of the above orbitals are set equal to 2.0. Fall-off parameters for the remaining orbitals is choosen to be equal to 1.0. To maintain the orthogonality of the basis the Gram-Schmidt orthogonalization is performed. The other index representing the one-electron states of the outer electron can be as large as required to ensure convergence of the results. In this work its upper limit is taken the same as N, i.e., the total basis size $\sum_{l=0}^{l_{\rm max}}(n_{\rm max} - l)$ with $n_{\rm max}$ and $l_{\rm max}$ being the maximum principal and orbital quantum numbers, respectively. As the basis size increases, the negative energy states become closer to their eigenstates while the positive energy ones provide an increasingly dense discretization of the continuum. A basis with $n_{\rm max} = 20$ and $l_{\rm max} = 5$ was sufficiently large to obtain convergent results for the cross sections presented in this work. With this basis we obtain an ionization potential of the helium ground state of 24.544 eV which is very close to the measured value of 24.586 eV. In what follows we refer to this way of constructing the wave function as the multiconfiguration (MC) description. Figure 4.2 shows the energies of helium pseudostates obtained in the multiconfigurational description. We see that the MC model gives very accurate energies not only for the ground state but also for the low-lying excited states.

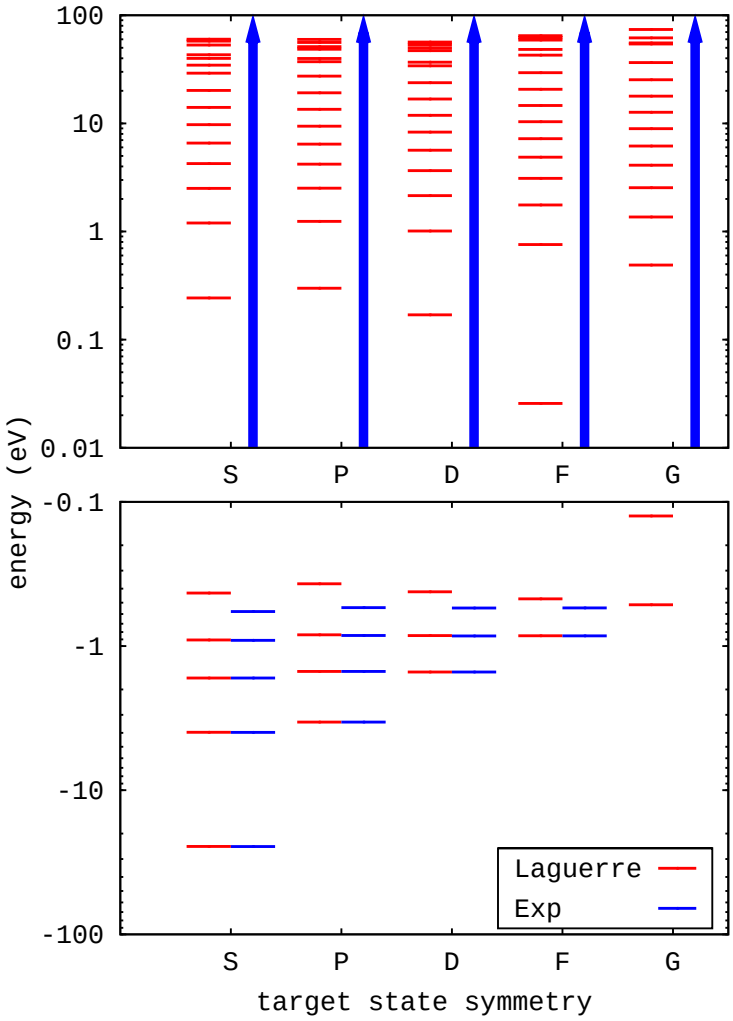

Figure 4.2: Energy levels of atomic helium obtained in the multiconfigurational description of the target. The experimentally measured values are due to the combination of [126–134]

.

In order to demonstrate the effect of the inner electron excitations on the single ionization we also perform calculations assuming the frozen-core (FC) approximation. As already mentioned, in this approximation the inner electron is always assumed to be in its 1s orbital, i.e., the upper limit of the index b in Eq. (4.42) is equal to 1. The ionization potential of the ground state in the FC

approximation is 23.736 eV.

4.6 Direct transition amplitudes for antiproton-helium collisions

For antiproton-helium collisions the direct transition amplitudes $\mathcal{V}_{\alpha'\alpha}(q_{\alpha'}, q_\alpha; \boldsymbol{b})$ in the impact-parameter space are also found through integrals $I_{\alpha'\alpha}$. The integrals $I_{\alpha'\alpha}$ for this scattering process are written as

$$\begin{aligned} I_{\alpha'\alpha}(\boldsymbol{R}) &\equiv \langle\psi_{\alpha'}|U_{\alpha'\alpha}|\psi_\alpha\rangle_{\boldsymbol{R}} \\ &= \int d\boldsymbol{r}_1 d\boldsymbol{r}_2 \psi^*_{\alpha'}(\boldsymbol{r}_1, \boldsymbol{r}_2) \left(-\frac{2}{R} + \frac{1}{|\boldsymbol{R}-\boldsymbol{r}_1|} + \frac{1}{|\boldsymbol{R}-\boldsymbol{r}_2|}\right) \psi_\alpha(\boldsymbol{r_1}, \boldsymbol{r_2}). \end{aligned} \tag{4.44}$$

Considering the symmetry with respect to interchanging r_1 and r_2 we can rewrite it as

$$I_{\alpha'\alpha}(\boldsymbol{R}) = 2\int d\boldsymbol{r}_1 d\boldsymbol{r}_2 \psi^*_{\alpha'}(\boldsymbol{r}_1, \boldsymbol{r}_2) \left(-\frac{1}{R} + \frac{1}{|\boldsymbol{R}-\boldsymbol{r}_1|}\right) \psi_\alpha(\boldsymbol{r_1}, \boldsymbol{r_2}). \tag{4.45}$$

With the He wave functions as given in Eq. (4.42) $I_{\alpha'\alpha}(\boldsymbol{R})$ becomes

$$\begin{aligned} I_{\alpha'\alpha}(\boldsymbol{R}) =& 2\sum_{a,b} C^{\alpha'}_{a,b} \sum_{m_a m_b} C^{l_{\alpha'} m_{\alpha'}}_{l_a m_a l_b m_b} \sum_{c,d} C^{\alpha}_{c,d} \sum_{m_c m_d} C^{l_\alpha m_\alpha}_{l_c m_c l_d m_d} \\ &\times \int d\boldsymbol{r}_1 d\boldsymbol{r}_2 \phi_a(r_1)\phi_b(r_2) Y^*_{l_a m_a}(\widehat{\boldsymbol{r}}_1) Y^*_{l_b m_b}(\widehat{\boldsymbol{r}}_2) \\ &\times \left(-\frac{1}{R} + \frac{1}{|\boldsymbol{R}-\boldsymbol{r}_1|}\right) \phi_c(r_1)\phi_d(r_2) Y_{l_c m_c}(\widehat{\boldsymbol{r}}_1) Y_{l_d m_d}(\widehat{\boldsymbol{r}}_2). \end{aligned} \tag{4.46}$$

Using the orthogonality of the spherical harmonics

$$\int d\widehat{\boldsymbol{r}}_2 \, Y^*_{l_b m_b}(\widehat{\boldsymbol{r}}_2) \, Y_{l_d m_d}(\widehat{\boldsymbol{r}}_2) = \delta_{l_b l_d} \delta_{m_b m_d} \tag{4.47}$$

we perform the integration over angular coordinates of the second electron to get

$$\begin{aligned} I_{\alpha'\alpha}(\boldsymbol{R}) =& 2\sum_{a,b} C^{\alpha'}_{a,b} \sum_{c,d} C^{\alpha}_{c,d} \sum_{m_a m_b m_c} C^{l_{\alpha'} m_{\alpha'}}_{l_a m_a l_b m_b} C^{l_\alpha m_\alpha}_{l_c m_c l_b m_b} \langle b|d\rangle \\ &\times \int d\boldsymbol{r}_1 \phi_a(r_1) Y^*_{l_a m_a}(\widehat{\boldsymbol{r}}_1) \left(-\frac{1}{R} + \frac{1}{|\boldsymbol{R}-\boldsymbol{r}_1|}\right) \phi_c(r_1) Y_{l_c m_c}(\widehat{\boldsymbol{r}}_1). \end{aligned} \tag{4.48}$$

Here

$$\langle b|d\rangle = \int dr_2 r_2^2 \phi_b(r_2)\phi_d(r_2) \tag{4.49}$$

is an overlap between two orbitals. The angular part of the remaining integral in Eq. (4.48) can be taken analytically just like in the case of antiproton-hydrogen collisions (§4.4)

$$\begin{aligned}&\int d\boldsymbol{r}_1 \phi_a(r_1) Y^*_{l_a m_a}(\widehat{\boldsymbol{r}}_1)\left(-\frac{1}{R}+\frac{1}{|\boldsymbol{R}-\boldsymbol{r}_1|}\right)\phi_c(r_1)Y_{l_c m_c}(\widehat{\boldsymbol{r}}_1)\\ &=\sqrt{4\pi}\sum_{\lambda\mu}\frac{[l_c]}{[\lambda][l_a]}\,C^{l_a 0}_{\lambda 0\, l_c 0}\,C^{l_a m_a}_{\lambda\mu\, l_c m_c}Y^*_{\lambda\mu}(\widehat{\boldsymbol{R}})\int_0^\infty dr_1 r_1^2 \phi_a(r_1)\phi_c(r_1)\mathcal{U}_\lambda(R,r_1).\end{aligned} \tag{4.50}$$

With this

$$\begin{aligned}I_{\alpha'\alpha}(\boldsymbol{R}) =&2\sqrt{4\pi}\sum_{a,b,c,d,\lambda,\mu}\frac{[l_c]}{[\lambda][l_a]}C^{\alpha'}_{ab}C^{\alpha}_{cd}C^{l_a 0}_{\lambda 0 l_c 0}Y^*_{\lambda\mu}(\widehat{\boldsymbol{R}})\langle b|d\rangle\\ &\times\int_0^\infty dr_1 r_1^2\phi_a(r_1)\phi_c(r_1)\mathcal{U}_\lambda(R,r_1)\sum_{m_a m_b m_c}C^{l_{\alpha'}m_{\alpha'}}_{l_a m_a l_b m_b}C^{l_\alpha m_\alpha}_{l_c m_c l_b m_b}C^{l_a m_a}_{\lambda\mu l_c m_c}.\end{aligned} \tag{4.51}$$

In (4.51) we take the sum over projections m_a, m_b and m_c to get

$$\sum_{m_a m_b m_c}C^{l_{\alpha'}m_{\alpha'}}_{l_a m_a l_b m_b}C^{l_\alpha m_\alpha}_{l_c m_c l_b m_b}C^{l_a m_a}_{\lambda\mu l_c m_c} =(-1)^{l_a+l_b+l_\alpha+\lambda}[l_\alpha][l_a]\left\{\begin{array}{ccc} l_b & l_a & l_{\alpha'}\\ \lambda & l_\alpha & l_c\end{array}\right\}, \tag{4.52}$$

where the braces denote the $6j$ symbol of the first kind [135]. Finally we arrive at

$$\begin{aligned}I_{\alpha'\alpha}(\boldsymbol{R}) =&2\sqrt{4\pi}\sum_{a,b,c,d,\lambda,\mu}\frac{[l_\alpha][l_c]}{[\lambda]}C^{\alpha'}_{ab}C^{\alpha}_{cd}C^{l_{\alpha'}m_{\alpha'}}_{l_\alpha m_\alpha\lambda\mu}C^{l_a 0}_{l_c 0\lambda 0}Y^*_{\lambda\mu}(\hat{\boldsymbol{R}})(-1)^{l_a+l_b+l_\alpha+\lambda}\\ &\times\langle b|d\rangle\left\{\begin{array}{ccc} l_b & l_a & l_{\alpha'}\\ \lambda & l_\alpha & l_c\end{array}\right\}\int_0^\infty dr_1 r_1^2\mathcal{U}_\lambda(R,r_1)\phi_a(r_1)\phi_c(r_1).\end{aligned} \tag{4.53}$$

4.7 Experimental observables

In scattering experiments the main observables of interest are differential and integrated cross sections for various transitions including elastic, target excitation and ionization. In the impact parameter representation the integrated cross

section for the individual transition from the initial state (which is the ground state) to the final state nlm is given by

$$\sigma_{nlm} = 2\pi \int_0^\infty dbbP_{nlm}(b), \tag{4.54}$$

where the transition probability at a fixed value of the impact parameter b, $P_{nlm}(b)$ is related to the amplitude $\tilde{\mathcal{T}}_{nlm}(q_{\alpha'}, q_{\alpha''}; b)$ by

$$P_{nlm}(b) = \frac{1}{(2\pi v)^2} \left| \tilde{\mathcal{T}}_{nlm}(q_{\alpha'}, q_{\alpha''}; b) \right|^2. \tag{4.55}$$

The transition amplitudes $\tilde{\mathcal{T}}_{nlm}(q_{\alpha'}, q_{\alpha''}; b)$ are found from solving Eq. (4.19). The sum and the weighted sum of all partial probabilities yield the total and the total ionization probabilities

$$P_{\rm tot}(b) = \sum_{nlm} P_{nlm}(b), \tag{4.56}$$

$$P_{\rm ion}(b) = \sum_{nlm} g_{nlm} P_{nlm}(b). \tag{4.57}$$

The total and the total ionization cross sections can then be found in the same way as in Eq.(4.54). In Eq.(4.57) g_{nlm} is the overlap of the pseudostate nlm with the true continuum. In order to calculate the total ionization cross section the original CCC method suggests summing up only those partial cross sections which correspond to transitions into the positive energy states. However, generally speaking, all partial cross sections for excitation of the generated pseudostates can contribute to the latter with different weights [24]. These weights represent the fraction of the particular state nlm lying in the continuum and are calculated as

$$g_{nlm} = \int \left| \langle \varphi^-_{\boldsymbol{\kappa}} | \psi_{nlm} \rangle \right|^2 d\boldsymbol{\kappa}, \tag{4.58}$$

where $\varphi^-_{\boldsymbol{\kappa}}$ is the pure Coulomb wave function describing the true continuum. Calculations show that this improves the convergence as the total ionizaton

cross section defined this way converges monotonically with increasing principal quantum number n. For the hydrogen target having written the overlap g_{nlm} as

$$\int \left|\left\langle \varphi_{\boldsymbol{\kappa}}^{-}|\psi_{nlm}\right\rangle\right|^2 d\boldsymbol{\kappa} = \int_0^\infty f_{nl}(\kappa)d\kappa \tag{4.59}$$

McGovern et al. [24] investigated properties of

$$f_{nl}(\kappa) = \frac{2\kappa^2}{\pi}\left|b_{nl}(\kappa)\right|^2 \tag{4.60}$$

where

$$b_{nl}(\kappa) = \left|\int_0^\infty U_l(\kappa, r)R_{nl}(r)r^2 dr\right|^2, \tag{4.61}$$

is the overlap between the radial Coulomb wave $U_l(\kappa, r)$ and the radial pseudostate $R_{nl}(r)$. On the basis of calculations they suggested, without proof, that at a momentum $\kappa_{n'l}$ corresponding to a pseudostate energy $\epsilon_{n'l}$ ($\kappa_{n'l}^2/2 = \epsilon_{n'l}$) the distribution $f_{nl}(\kappa_{n'l})$ might be identically zero unless $n' = n$, i.e.

$$f_{nl}(\kappa_{n'l}) = 0, \text{ for } n' \neq n. \tag{4.62}$$

This important feature can be proven using the results obtained by Stelbovics [136], Yamani and Reinhardt [137]. We give the proof in the Appendix (B).

To be able to calculate various differential cross sections we have to determine the scattering amplitude $T(\boldsymbol{q}_f, \boldsymbol{q}_i)$. The scattering amplitude is written in terms of Ψ_i^+ as [138]

$$T(\boldsymbol{q}_f, \boldsymbol{q}_i) = \langle \Phi_f^-|\overleftarrow{H} - E|\Psi_i^+\rangle, \tag{4.63}$$

where Φ_f^- is the asymptotic wave function describing the final state and the arrow over the Hamiltonian operator indicates the direction of its action. Eq. (4.63) is general and applicable for both excitation and breakup of the target. It is also valid for rearrangement channels, however, in the present work we neglect them. If the result of the scattering is excitation of the target then Φ_f^-

is given as a product of a plane wave describing the scattered projectile and a bound state wave function of the target in the final state. If the collision leads to ionization of the target then Φ_f^- is a three-body Coulomb asymptotic state consisting in incoming waves representing the three unbound particles in the final state [139–141].

As already mentioned our approach is based on the expansion of Ψ_i^+ in terms of a set of N square-integrable pseudostates ψ_α which are obtained by diagonalizing the hydrogen Hamiltonian using orthogonal Laguerre functions. With these we form a projection operator

$$I^N = \sum_{\alpha=1}^{N} |\psi_\alpha\rangle\langle\psi_\alpha|. \tag{4.64}$$

The main idea of the CCC approach to scattering consists in the following replacement [142]:

$$T(\boldsymbol{q}_f, \boldsymbol{q}_i) \to \lim_{N\to\infty} \langle \Phi_f^- I^N | \overleftarrow{H} - E | I^N \Psi_i^+ \rangle \equiv \lim_{N\to\infty} T^N(\boldsymbol{q}_f, \boldsymbol{q}_i). \tag{4.65}$$

The action of the projection operator limits the target space and replaces the full set of target states (including the non-square-integrable continuum) with a set of square-integrable states. This effectively screens the Coulomb interaction between the projectile and target, even when ionized. In other words, we have

$$T^N(\boldsymbol{q}_f, \boldsymbol{q}_i) = \langle \Phi_f^- I^N | \overleftarrow{H} - E | I^N \Psi_i^+ \rangle = \langle \boldsymbol{q}_f \varphi_f I^N | \overleftarrow{H} - E | I^N \Psi_i^+ \rangle, \tag{4.66}$$

where $\boldsymbol{q}_f$ is the momentum of the scattered projectile and φ_f is any given state from the full set of the target eigenstates $\{\varphi_{nlm}, \varphi_{\boldsymbol{\kappa}}^-\}$. Here $\varphi_{\boldsymbol{\kappa}}^-$ is the pure incoming Coulomb wave representing the continuum state of the ejected electron with the momentum $\boldsymbol{\kappa}$. We note that when $\varphi_f = \varphi_{nlm}$ amplitude $T^N(\boldsymbol{q}_f, \boldsymbol{q}_i)$ converges to the exact scattering amplitude $T(\boldsymbol{q}_f, \boldsymbol{q}_i)$ for excitation of the final nlm state as $N \to \infty$. At the same time when $\varphi_f = \varphi_{\boldsymbol{\kappa}}^-$ amplitude $T^N(\boldsymbol{q}_f, \boldsymbol{q}_i)$

converges to

$$\tilde{T}(\boldsymbol{q}_f, \boldsymbol{q}_i) = \langle \boldsymbol{q}_f \varphi_\kappa^- | \overleftarrow{H} - E | \Psi_i^+ \rangle, \tag{4.67}$$

rather than to the exact amplitude of Eq. (4.63) for breakup. However, it has been recently demonstrated [143] that in this case the only difference between the exact amplitude of Eq. (4.63) and much simpler approximate ionization amplitude of Eq. (4.67) is a phase factor, i.e. $|T(\boldsymbol{q}_f, \boldsymbol{q}_i)| = |\tilde{T}(\boldsymbol{q}_f, \boldsymbol{q}_i)|$. Therefore, for the purpose of calculating cross sections it is sufficient to know only magnitude of $T^N(\boldsymbol{q}_f, \boldsymbol{q}_i)$ at sufficiently large N [1] .

We expand (4.66) and write

$$\begin{aligned} T^N(\boldsymbol{q}_f, \boldsymbol{q}_i) &= \sum_{\alpha=1}^{N} \langle \varphi_f | \psi_\alpha \rangle \langle \boldsymbol{q}_f \psi_\alpha | \overleftarrow{H} - E | I^N \Psi_i^+ \rangle \\ &= \sum_{\alpha=1}^{N} \langle \varphi_f | \psi_\alpha \rangle \langle \boldsymbol{q}_f \psi_\alpha | T | \psi_i \boldsymbol{q}_i \rangle \equiv \sum_{\alpha=1}^{N} \langle \varphi_f | \psi_\alpha \rangle T_{\alpha i}(\boldsymbol{q_f}, \boldsymbol{q_i}). \end{aligned} \tag{4.68}$$

Thus both excitation and ionization amplitudes are obtained upon calculation of transition matrix elements $T_{\alpha i}(\boldsymbol{q_f}, \boldsymbol{q_i})$ which are related to the impact-parameter space transition amplitudes as follows

$$\begin{aligned} T_{\alpha i}(\boldsymbol{q}_f, \boldsymbol{q}_i) &= \frac{1}{2\pi} \int d\boldsymbol{b} e^{i\boldsymbol{p}_\perp \boldsymbol{b}} \mathcal{T}_{\alpha i}(q_f, q_i; \boldsymbol{b}) \\ &= i^{\Delta m} e^{i \Delta m \varphi_p} \int_0^\infty dbb \tilde{\mathcal{T}}_{fi}(q_f, q_i; b) J_{\Delta m}(p_\perp b), \end{aligned} \tag{4.69}$$

where $\boldsymbol{p} = \boldsymbol{q}_i - \boldsymbol{q}_f$.

For the antiproton-impact ionization of hydrogen we write the overlap coefficient in Eq. (4.68) in the form

$$\langle \varphi_{\boldsymbol{\kappa}}^- | \psi_\alpha \rangle = \sqrt{\frac{2}{\pi}} (-i)^l e^{i\sigma_l} b_{nl}(\kappa) Y_{lm}(\hat{\boldsymbol{\kappa}}), \tag{4.70}$$

[1] Converged cross sections presented below indicate convergence of $|T^N(\boldsymbol{q}_f, \boldsymbol{q}_i)|$. As far as the phase of $T^N(\boldsymbol{q}_f, \boldsymbol{q}_i)$ is concerned in the CCC method it converges too, from which the phase of $T(\boldsymbol{q}_f, \boldsymbol{q}_i)$ can be recovered. This procedure has been demonstrated in the example of a model electron-impact ionization problem [144].

where the overlap $b_{nl}(\kappa)$ is already defined in Eq. (4.61) and σ_l and Y_{lm} are the Coulomb phase shift and spherical harmonics, respectively.

If the pseudostates are constructed in such a way that for some $\overline{n}$, $\kappa_{\overline{n}l} = \kappa_{\overline{n}l'} = \kappa_{\overline{n}}$ ($\kappa_{nl} = \sqrt{2\epsilon_{nl}}$), i.e. all l symmetries of the states with $n = \overline{n}$ are aligned to have the momentum $\kappa_{\overline{n}}$, then using Eq. (4.70) and the already mentioned fact that $f_{nl}(\kappa_{\overline{n}l}) = 0$ for $n \neq \overline{n}$ (see Appendix B), it is possible to further simplify Eq. (4.68) to (indicating the momentum of the ejected electron $\boldsymbol{\kappa}$ as a subindex)

$$T^N_{\boldsymbol{\kappa}_{\overline{n}}}(\boldsymbol{q}_f, \boldsymbol{q}_i) = \sum_{l=0}^{l_{\max}} \sum_{m=-l}^{l} \sqrt{\frac{2}{\pi}} (-i)^l e^{i\sigma_l} b_{\overline{n}l}(\kappa_{\overline{n}}) T_{\{\overline{n}lm\}1\mathrm{s}}(\boldsymbol{q}_f, \boldsymbol{q}_i) Y_{lm}(\hat{\boldsymbol{\kappa}}_{\overline{n}}), \tag{4.71}$$

where $l_{\max}$ is a parameter representing the maximum orbital quantum number. By iterating the characteristic fall-off parameter McGovern et al. [24] constructed such a basis to calculate the ionization amplitude at the ejected electron momentum $\kappa_{\overline{n}}$. However, this is not an efficient procedure as it requires generation of a new set of pseudostates and repeated solution of the associated coupled equations for each ejected electron energy. Therefore we apply an interpolation scheme on $\sqrt{2/\pi}(-i)^l e^{i\sigma_l} b_{nl}(\kappa_{nl}) T_{\{nlm\}1\mathrm{s}}(\boldsymbol{q}_f, \boldsymbol{q}_i)$ in Eq. (4.70) so as to be able to obtain the required amplitudes at any ejected electron energy. As a result we obtain the interpolated functions for each l and m which we denote as $F_{lm}(\boldsymbol{q}_f, \boldsymbol{q}_i, \kappa)$. Finally, the ionization amplitude is written as

$$T^N_{\boldsymbol{\kappa}}(\boldsymbol{q}_f, \boldsymbol{q}_i) = \sum_{l=0}^{l_{\max}} \sum_{m=-l}^{l} F_{lm}(\boldsymbol{q}_f, \boldsymbol{q}_i, \kappa) Y_{lm}(\hat{\boldsymbol{\kappa}}). \tag{4.72}$$

The same technique can be applied to antiproton-helium collisions as well, provided He is considered in the frozen-core approximation, i.e. the inner electron of the target is always in its 1s orbital. The function $b_{nl}(\kappa_{nl})$ in this case is constructed from overlaps between the radial Coulomb wave U_l and the one-

electron orbitals ϕ_{nl}:

$$b_{nl}(\kappa) = \langle\phi_{1s}|\phi_{1s}\rangle \int_0^\infty U_l(\kappa, r)\phi_{nl}(r)r^2 dr + \langle\phi_{1s}|\phi_{nl}\rangle \int_0^\infty U_l(\kappa, r)\phi_{1s}(r)r^2 dr. \quad (4.73)$$

The most detailed observable, the triply differential cross section (TDCS), can be directly calculated using the ionization amplitude defined in the Eq. (4.72) as

$$\frac{d^3\sigma(\boldsymbol{q}_f, \boldsymbol{q}_i, \boldsymbol{\kappa})}{dE d\Omega_e d\Omega_p} = M_\alpha^2 \frac{q_f \kappa}{q_i} |\tilde{T}_{\boldsymbol{\kappa}}(\boldsymbol{q}_f, \boldsymbol{q}_i)|^2. \quad (4.74)$$

This cross section is for the ionized electron being ejected into the solid angle $d\Omega_e$ with the energy in the range E to $E + dE$, when the projectile is incident along the quantization axis z ($\boldsymbol{k}_i \parallel z$) and further scattered into the solid angle $d\Omega_p$.

There are two kinds of double-differential cross sections (DDCS). The first one can be obtained by integrating the TDCS over the spherical coordinates of the scattered projectile:

$$\frac{d^2\sigma(q_f, q_i, \boldsymbol{\kappa})}{dE d\Omega_e} = \int \frac{d^3\sigma(\boldsymbol{q}_f, q_i, \boldsymbol{\kappa})}{dE d\Omega_e d\Omega_p} d\Omega_p = M_\alpha^2 \frac{q_f \kappa}{q_i} \sum_{l=0}^{l_{\max}} \sum_{l'=0}^{l} \sum_{m=-l'}^{l'} \frac{2}{1+\delta_{l'l}} \times Y_{lm}(\hat{\kappa}) Y_{l'm}^*(\hat{\kappa}) \mathrm{Re}\left[\int d\Omega_p F_{lm}(\boldsymbol{q}_f, q_i, \kappa) F_{l'm}^*(\boldsymbol{q}_f, q_i, \kappa)\right]. \quad (4.75)$$

The DDCS defined this way shows the angular and energy distributions of the ejected electrons. Another DDCS can be formed by integrating the TDCS over the spherical coordinates of the ejected electron (this can be done analytically) and is written as

$$\frac{d^2\sigma(\boldsymbol{q}_f, q_i, \kappa)}{dE d\Omega_p} = \int \frac{d^3\sigma(\boldsymbol{q}_f, q_i, \boldsymbol{\kappa})}{dE d\Omega_e d\Omega_p} d\Omega_e = M_\alpha^2 \frac{q_f \kappa}{q_i} \sum_{l=0}^{l_{\max}} \sum_{m=-l}^{l} |F_{lm}(\boldsymbol{q}_f, q_i, \kappa)|^2. \quad (4.76)$$

This cross section is differential in the angular variables of the scattered projectile and the energy of the ejected electron.

Three different single differential cross sections (SDCS) can be defined. The SDCS in the angular variables of the ejected electron $d\sigma/d\Omega_e$, and in the angular variables of the scattered projectile $d\sigma/d\Omega_p$ are calculated as

$$\begin{aligned}\frac{d\sigma(q_f,q_i,\boldsymbol{\kappa})}{d\Omega_e} =& M_\alpha^2\frac{q_f}{q_i}\sum_{l=0}^{l_{\max}}\sum_{l'=0}^{l}\sum_{m=-l'}^{l'}\frac{2}{1+\delta_{l'l}} \\ &\times Y_{lm}(\hat{\kappa})Y^*_{l'm}(\hat{\kappa})\mathrm{Re}\left[\int d\Omega_p\int d\kappa\kappa^2 F_{lm}(\boldsymbol{q}_f,q_i,\kappa)F^*_{l'm}(\boldsymbol{q}_f,q_i,\kappa)\right],\end{aligned} \tag{4.77}$$

and

$$\frac{d\sigma(\boldsymbol{q}_f,q_i,\kappa)}{d\Omega_p} = M_\alpha^2\frac{q_f}{q_i}\sum_{l=0}^{l_{\max}}\sum_{m=-l}^{l}\int d\kappa\kappa^2|F_{lm}(\boldsymbol{q}_f,q_i,\kappa)|^2, \tag{4.78}$$

respectively. The SDCS in the energy of the ejected electron can be calculated in two different ways, by integrating of either Eq. (4.75) over Ω_e or Eq. (4.76) over Ω_p. Integration of Eq. (4.76) over Ω_p gives us

$$\frac{d\sigma(q_f,q_i,\kappa)}{dE} = M_\alpha^2\frac{q_f\kappa}{q_i}\sum_{l=0}^{l_{\max}}\sum_{m=-l}^{l}\int d\Omega_p|F_{lm}(\boldsymbol{q}_f,q_i,\kappa)|^2. \tag{4.79}$$

We refer to this way of calculating $d\sigma/dE$ as an integration method. On the other hand this quantity can also be obtained directly from the integrated cross sections for the transitions to the open positive energy states $\sigma_{nlm}|_{\epsilon_{nl}>0}$ [145]. Let us express the total ionization cross section as a sum of its l components

$$\sigma_{\mathrm{ion}} = \sum_{nlm:\epsilon_{nl}>0}\sigma_{nlm} = \sum_{l=0}^{l_{\max}}\sigma^l_{\mathrm{ion}}, \tag{4.80}$$

where

$$\sigma^l_{\mathrm{ion}} = \sum_{n,\epsilon_{nl}>0}^{N_l}\sum_m\sigma_{nlm} \tag{4.81}$$

with N_l being the basis size of pseudostates for symmetry l. In Eq. (4.81) the sum $\sum_{n,\epsilon_{nl}>0}^{N_l}$ approximates the continuum integral $\int_0^{E_{\max}} dE$ and therefore the quantity $\sum_m \sigma_{nlm}$ can be considered as SDCS of symmetry l divided by its weight w_n^l at the particular continuum energy ϵ_{nl}, i.e.

$$\sum_m \sigma_{nlm} = w_n^l \frac{d\sigma^l}{dE}\bigg|_{E=\epsilon_{nl}}. \tag{4.82}$$

The weights w_n^l used in the calculations are defined according to Simpson's rule

$$w_n^l = \frac{\epsilon_{n+1,l} + \epsilon_{n,l}}{2} - \frac{\epsilon_{n,l} + \epsilon_{n-1,l}}{2}, \tag{4.83}$$

$$w_{\text{first}}^l = \frac{\epsilon_{n_{\text{first}}+1,l} + \epsilon_{n_{\text{first}},l}}{2}, \tag{4.84}$$

$$w_{\text{last}}^l = \epsilon_{\max} - \frac{\epsilon_{n_{\text{last}},l} + \epsilon_{n_{\text{last}}-1,l}}{2}, \tag{4.85}$$

and should satisfy

$$\int_0^{E_{\max}} dE = \sum_n w_n^l = E_{\max}. \tag{4.86}$$

After interpolating the $l-$manifold SDCSs $d\sigma^l/dE$ into some desirable ejection energy grid we can find the total SDCS by summing up the interpolated functions. For the sake of sufficient accuracy of the SDCS, one should require enough open positive energy channels. We refer to this method as a summation method. Agreement between the SDCS extracted using the summation and integration methods is a useful check of the consistency of the current approach to calculating the ionization cross sections.

4.8 Chapter summary

In this chapter we have presented the basic formalism that allows us to solve the momentum-space coupled-channel Lippmann-Schwinger equations for the fully off-shell transition amplitudes (2.20). This has been realised via transformation of (2.20) into the impact-parameter space. The derivation of impact-parameter space scattering equations (4.19) has been given in detail. The developed formalism has been applied to calculate scattering of antiprotons on atomic hydrogen and helium. This required generation of square-integrable Laguerre pseudostates for hydrogen and helium. Whereas the hydrogen pseudostates are calculated relatively easily, pseudostates for the two-electron target of helium required more effort. To describe the electron-electron correlation the configuration-interaction approach of Fursa and Bray [122] has been used. Impact-parameter representation of effective potentials for antiproton-hydrogen and antiproton-helium collisions have been reduced to maximally simple form for practical calculations. A procedure has been developed to extract all major experimental observables from the calculated T matrix elements. Particularly explicit expressions have been derived for various differential cross sections including the triply differential cross section. In the next chapters we will present the results of our numerical calculations for $\bar{p} + \mathrm{H}(1\mathrm{s})$ and $\bar{p} + \mathrm{He}(1^1\mathrm{S})$ scattering.

Chapter 5

Antiproton scattering on the ground state of hydrogen

Experimental studies of antiproton-hydrogen collisions are limited to work by Knudsen et al. [26] where the authors measured the total ionization cross section as a function of antiproton energy. The measurements were performed in the energy range from 30 to 1 MeV. As far as differential cross sections are concerned there are no measured data at all. However, recent advances in experimental techniques have rendered such measurements feasible. The lack of comprehensive measurements is related to the difficulties associated with the preparation of both the high intensity antiproton beam and the hydrogen target itself. The experimental study of antiproton collisions with atomic and molecular targets is one of the main goals of the low-energy antiproton facility at CERN. Some differential measurements of antiproton-helium collisions have already been carried out at this facility using the experimental technique known as cold-target recoil-ion momentum spectroscopy (COLTRIMS) [39]. More detailed experiments are planned for the hydrogen targets as well [146]. In addition, the future international collaborations such as Low-energy Antiproton and Ion Research (FLAIR) [147], and the Facility for Antiproton and Ion Research (FAIR) [148] will be able to provide accurate data for total, as well as various differential cross sections

including the TDCS for slow antiprotons ionizing a variety of targets including atomic hydrogen.

In this chapter we present our theoretical results on antiproton scattering on the ground state of hydrogen. First we test our computer code using various available benchmark results obtained by other groups. Then we demonstrate the convergence of our full results. Finally we compare the converged results with other theoretical calculations and the experiment where available.

5.1 Details of calculations

In order to calculate experimentally measurable quantities one should first calculate the transition amplitudes $\tilde{\mathcal{K}}_{\alpha'\alpha}(q_{\alpha'}, q_{\alpha''}; b)$ and ultimately $\tilde{\mathcal{T}}_{\alpha'\alpha}(q_{\alpha'}, q_{\alpha''}; b)$ for the values of b in a sufficiently long interval. This can be done by solving the system of integral equations (4.23) for a given value of b. With the initial state being the ground state the dimension of the system depends on the number of possible final states taken into account. The number of intermediate states is set equal to the number of final states in order to couple all included channels.

The effective potentials for direct transitions $\tilde{\mathcal{V}}_{\alpha'\alpha}(q_{\alpha'}, q_{\alpha''}; b)$ in Eq. (4.23) are calculated using Eq. (4.28). Their analytical evaluation in a general form is not efficient and may cause numerical inaccuracies especially when the basis size N is very large. Numerical calculation of $\tilde{\mathcal{V}}_{\alpha'\alpha}(q_{\alpha'}, q_{\alpha''}; b)$ requires evaluation of the integral $I_{\alpha'\alpha}(R)$ in Eq (4.25). This can be performed to a desired accuracy by using the calculated values of pseudostates (4.31) on a sufficiently fine radial mesh. The integrand in Eq. (4.28) becomes highly oscillatory when $p_{\alpha'\alpha\|}$ is large. However, these oscillations are periodic and there are standard routines for efficient and accurate calculations of such integrals. Note that the larger $p_{\alpha'\alpha\|}$ for a particular transition, the smaller its relative significance is in comparison

with low-$p_{\alpha'\alpha\|}$ transitions.

Knowing the effective potentials for a given value of the impact parameter we can solve Eq. (4.23) by a standard quadrature method. The kernel of the equations containing principal value integrals is discretized using a Gauss-Legendre quadrature. The problem of channel-dependent singularities is overcome by using a unique quadrature in each channel containing the singularity. Accuracy of the integral in the sense of the principal value was ensured by using a subquadrature consisting of an even number of Gauss-Legendre points, symmetrically distributed in the immediate vicinity of the singular point. This procedure is similar to the widely used subtraction method with the subtraction being numerically zero. Once the $\tilde{\mathcal{K}}_{\alpha'\alpha}(q_{\alpha'}, q_\alpha; b)$ matrix elements are calculated, the physical transition amplitudes $\tilde{\mathcal{T}}_{\alpha'\alpha}(q_{\alpha'}, q_\alpha; b)$ on-the-energy-shell can be extracted following the procedure given in Ref. [77].

In order to test our computer code we have performed the following. By substituting our effective potentials for a direct channel with ones for the exchange channel we can solve the electron-transfer problem in proton collisions with hydrogen. This problem was solved in Ref. [124] by using the true bound hydrogenic eigenstates and the on-shell approximation. If we use a sufficiently large basis size we can construct our basis in such a way that the lowest pseudostates accurately represent the exact hydrogenic eigenstates. Consequently, if we use only those lowest states out of this basis and solve Eq. (4.21) with effective potentials for the exchange channel and turn off the off-shell effects we must be able to obtain results of calculations with 55 states ($n_{\max} = 5, l_{\max} = 4, |m_{\max}| = 4$) reported in Ref. [124]. We have performed such calculations by constructing corresponding pseudobasis and obtained full agreement. This validates our code in terms of channel coupling.

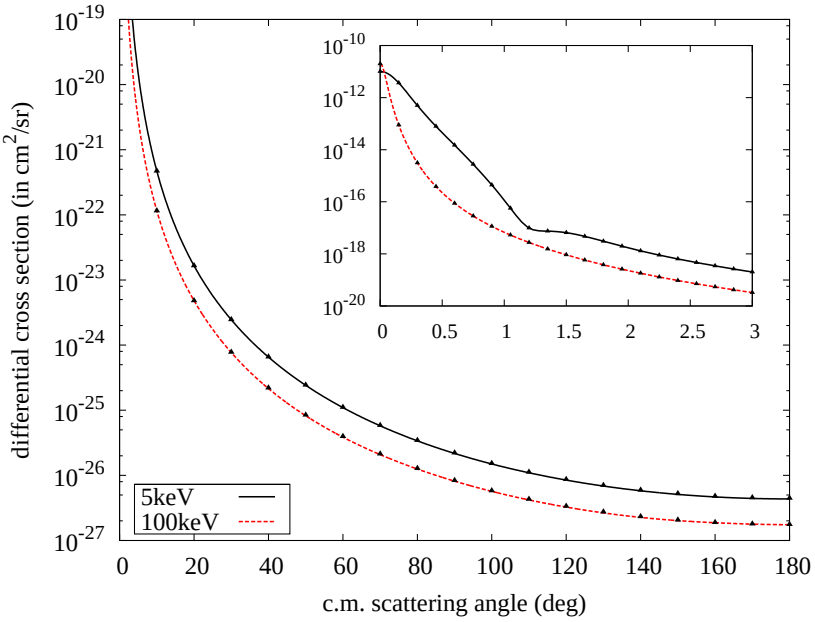

Figure 5.1: The differential cross section for $\bar{p} + H(1s)$ elastic scattering in the angle of the scattered antiproton: curves, results of the three-dimensional integral-equation approach; solid triangles, results of present one state impact-parameter representation calculations. The insert shows the same but for small angles.

Before performing calculations we also test the approximation (4.14) used when we transformed the momentum-space Lippmann-Schwinger equations into impact-parameter representation. Since the integration variable $\theta_{\boldsymbol{q}}$ in Eq. (4.12) goes from 0 to $\pi/2$, one might expect that the approximation $\sin\theta_{\boldsymbol{q}} \approx \theta_{\boldsymbol{q}}$ could adversely affect the accuracy of calculations. However, our calculations show a sharp decay in amplitude $V_{\alpha'\alpha}(\boldsymbol{q}_{\alpha'}, \boldsymbol{q}_{\alpha})$ with the scattering angle $\theta_{\boldsymbol{q}}$. Therefore, the main contribution from the integration over $\theta_{\boldsymbol{q}}$ comes essentially only from the small-angle region. This fact makes the approximation (4.14) reliable in practice (in our particular case). In order to numerically test this claim we have performed one state (only the elastic scattering channel is considered) calculations for the angular differential cross section and compared the results with the results obtained by the three-dimensional integral-equation approach which does

not use approximation (for details of the method see [99–101]). The results are shown in Fig.5.1. The perfect agreement at all scattering angles suggests that the aforementioned approximations used in the present approach can indeed give reliable results. The observed interesting feature of the elastic cross section near 1 degree at 5 keV is the result of the interplay of antiproton interactions with the target electron and nucleus.

5.2 Convergence studies

All pseudostate expansion based methods need to be checked for convergence by increasing the size of the basis. The size of the underlying basis was increased until an acceptable convergence was obtained. As it has already been mentioned, our final convergent results do not depend on characteristic fall-off parameter λ_l of the pseudostate expansion, however, the rate of convergence does. A series of calculations have been performed to study the convergence with increasing Laguerre basis size.

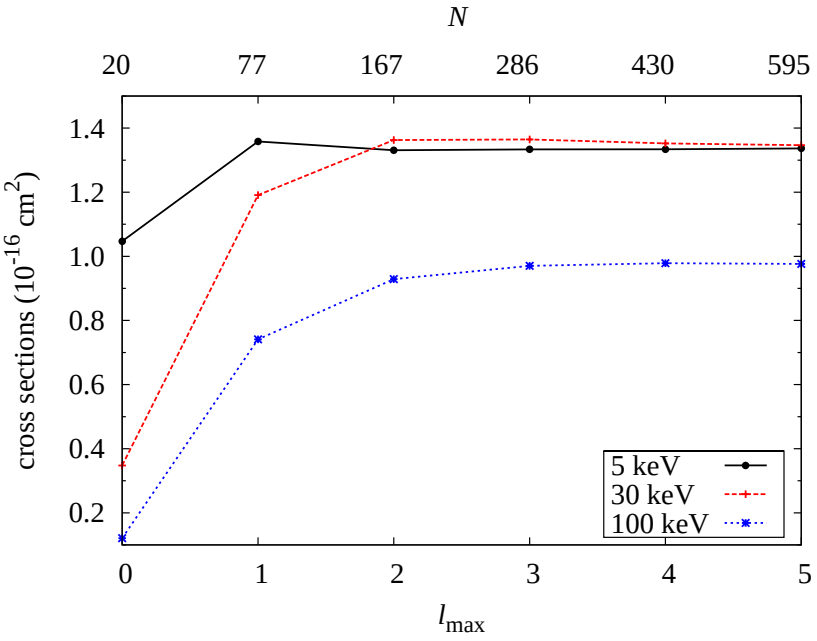

Figure 5.2: Convergence of the total cross section for the ionization of H(1s) by antiproton impact with increasing $l_{\max}$ when $n_{\max} = 20$.

Trial calculations have shown that the convergence is fastest when parameter λ_l is chosen to reproduce the ground state of hydrogen with the fewest basis states. On this basis, in our further calculations this parameter is set equal to 1. Consequently, for convergence studies we need to do calculations with basis sizes $N = \sum_{l=0}^{l_{\max}} (n_{\max} - l)(2l + 1)$ by increasing parameters $n_{\max}$ and $l_{\max}$.

The convergence studies have been carried out in the whole energy region considered in this work. We give typical examples at projectile energies 5, 30 and 100 keV, i.e., at the position of the maximum in the experimentally measured TICS (see below) and at some distance from the maximum on both sides. The results at other energies were similar. First we fix the basis parameter $n_{\max}$ at some large value and systematically increase parameter $l_{\max}$ starting from 0. Fig. 5.2 shows convergence of the total ionization cross section (TICS) with increasing $l_{\max}$, while $n_{\max} = 20$ for each $l-$symmetry. As one can see from the

figure, the convergence with $l_{\max}$ is reached faster at lower energies. For instance, at 5 keV coupling of only S, P and D states gives sufficiently well convergent result, whereas at 30 and 100 keV the maximum angular momentum of included pseudostates must be at least 5 to achieve sufficient convergence. To be specific, at 5, 10 and 100 keV the difference between the TICS with $l_{\max} = 4$ and $l_{\max} = 5$ were 0.22%, 0.44% and 0.23%, respectively. We note that as a function of the angular momentum of included pseudostates the present method leads to more rapid convergence in the total ionization cross sections than the other methods reported in the literature. Thus, from these results one can conclude that $l_{\max} = 5$ is sufficient for all energies of our interest provided $n_{\max} = 20$. However, it has to be noted that such a basis is only sufficient for the convergence of total integrated cross sections. As it will be demonstrated later, the convergence in the fully differential cross sections generally requires inclusion of significantly higher angular momentum states. Next we check whether $n_{\max} = 20$ was sufficiently large in terms of convergence of the cross section as a function of the principal quantum number of included states.

Setting $l_{\max} = 5$ we examine the convergence of TICS with $n_{\max}$. The results are shown in 5.3. At all considered energies TICS increases monotonically before converging. The variations in the cross section when $n_{\max}$ changes from 19 to 20 at energies 5, 30 and 100 keV were 0.37%, 0.07% and 0.15%, respectively. Therefore, we conclude that $n_{\max} = 20$ is sufficient.

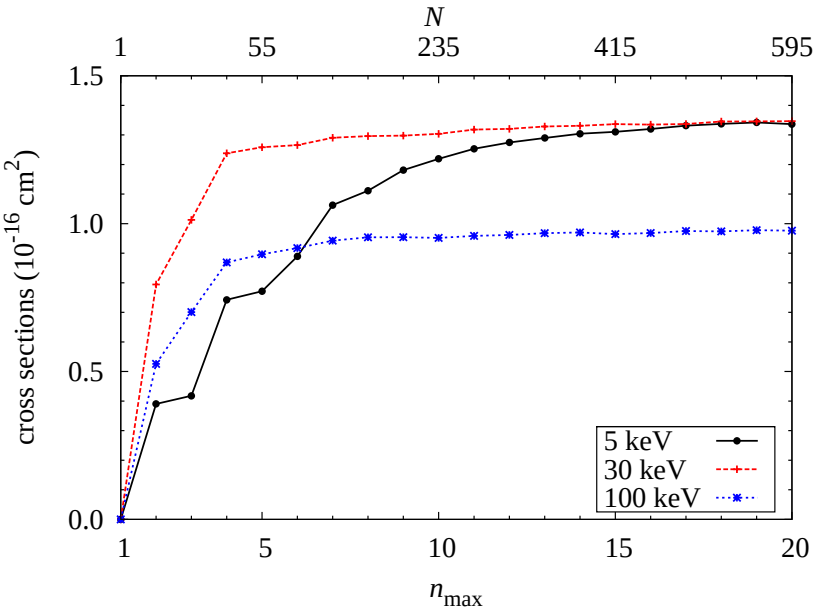

Figure 5.3: Convergence of the total cross section for the ionization of H(1s) by antiproton impact with increasing $n_{\max}$ when $l_{\max} = 5$.

Thus, in terms of the number of included pseudostates and their angluar momenta present calculations have converged to better than half of a percent. Another benchmark for our basis is the first Born results of Bates and Griffing [12] for the ionization cross section obtained in the full wave treatment. Fig. 5.4 shows the Born results obtained in our expansion method. One can see the excellent agreement is achieved with the exact Born results. The comparison between these results are listed in a numerical form in the appendix in Table C.1. This fact indicates that the size of our pseudobasis is sufficiently large to reproduce the physics of the process. Thus, based on our convergence study we conclude that the basis of 595 states ($n_{\max} = 20$ and $l_{\max} = 5$) is suitable for full-scale calculations.

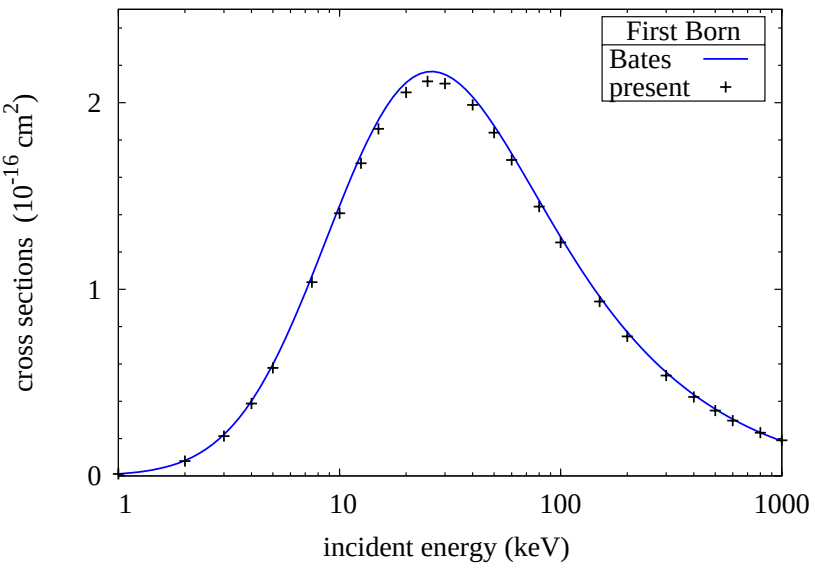

Figure 5.4: Total cross section for the ionization of H(1s) by antiproton impact in the first Born approximation. The exact Born results are due to Bates and Griffing [12].

Finally, a comment is appropriate about the quadrature used for the integration variable in Eq. (4.23). Despite the integral in Eq. (4.23) is semi-infinite, the quadrature points can be generated around the channel dependent on-shell momentum within sufficiently long interval. The length of the latter depends on the properties of the kernel. By systematically increasing the number of points and enlarging the interval the stable solution for the K matrix elements can be achieved. At lower impact energies the kernel becomes slowly decaying with increasing momentum transfer, therefore, in this region longer intervals are required. Consequently, the complexity of the problem grows as we go down to lower impact energies. In our largest calculations the dimension of the system of linear equations emerging after discretization of Eq. (4.23) was over a hundred thousand.

5.3 Integrated cross sections: Comparison with experiment and other theoretical results

In this section, we present our results for the intergated cross sections for the elastic scattering, excitation into a few low-lying states as well as ionization of atomic hydrogen by antiproton impact. We call our results CCC on the basis that they are convergent (within the limits specified in the previous subsection). We note that some coupled-channel approaches mentioned in this work are convergent in terms of the basis size as well (e.g., single-centre expansion approaches by McGovern et al. [24] and Igarashi et al. [25]), however they are semiclassical. A distinct feature of our approach is that it is based on the exact Schrödinger equation and fully quantum mechanical.

The cross sections are calculated for the incident energies ranging from 1 keV to 1 MeV. Our results for the total ionization cross section are shown in Fig. 5.5 in comparison with the experimental data of Knudsen et al. [26] and other calculations. The experimental data is normalized to the first Born cross section of [12] at high energies. The calculated cross sections are in excellent agreement with the experiment, showing a maximum around 10 keV and slowly decreasing as we cross to lower energies. There is a reasonably good agreement between present calculations and semiclassical coupled channel approaches [9, 18, 24, 25]. The results of McGovern et al. [24], Igarashi et al. [25] and Sahoo et al. [20] are shown in Fig 5.5. Despite being based on the same Schrödinger equation as the other semiclassical approaches, the three-dimensional lattice approach of Wells et al. [15] (not shown) gives noticeably larger results than the expansion-based methods. It is argued that for a number of reasons in the approaches utilizing the lattice based direct solution of the Schrödinger equation accumulated errors may reach 10%. For instance, except for states with $n \leq 3$ probabilities for excitation

of all other discrete states are included in the ionization probability. Discussion on the accuracy of the lattice calculations are found in Refs. [15]. While it is expected that the aforementioned CC methods by different groups agree well with each other, a good agreement with the present quantum-mechanical results might be indicating the quality of the semiclassical approximations. The numerical data of the present fully quantum-mechanical calculations are listed in the appendix in Table C.1.

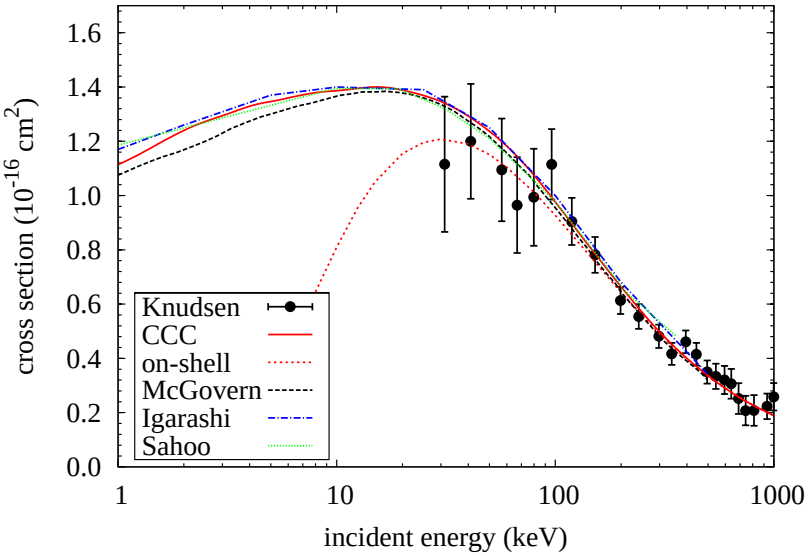

Figure 5.5: Total ionization cross section for antiproton-hydrogen scattering. Experimental data by Knudsen et al. [26], and the various semiclassical impact-parameter close-coupling calculations are due to McGovern et al. [24], Igarashi et al. [25], and Sahoo et al. [20]. Present fully off-shell calculations are denoted by CCC. On-shell only results are also presented.

Comparison with the on-shell results obtained by solving Eq. (4.21) (see also Ref. [125]) shows that the off-shell effects in the ionization channel are extremely important at lower energies. This is in contrast with the results of Ref. [101] where the one-channel problem was solved in the full off-shell mode. There the off-shell effects were found to be 20% or less. When the off-shell effects are neglected cross sections are somewhat similar to those obtained in

the perturbation methods due to weak coupling between channels. A visually better agreement of the on-shell results with the experiment at energies between 30 and 100 keV is just coincidence.

In Fig. 5.6 we present the total (TCS) and elastic (ECS) cross sections in comparison with the results of McGovern et al. [24]. Figure 5.6 shows perfect agreement between our results at all displayed energies. We emphasize that our approach is unitary and distributes the particle flux between the included channels through coupling. This is verified by the fact that the optical theorem is satisfied to at least eight-digit accuracy at all energies considered. Thus as far as the total cross section and its dominant elastic-scattering component are concerned there is almost one-to-one agreement between the fully quantum-mechanical and semiclassical methods.

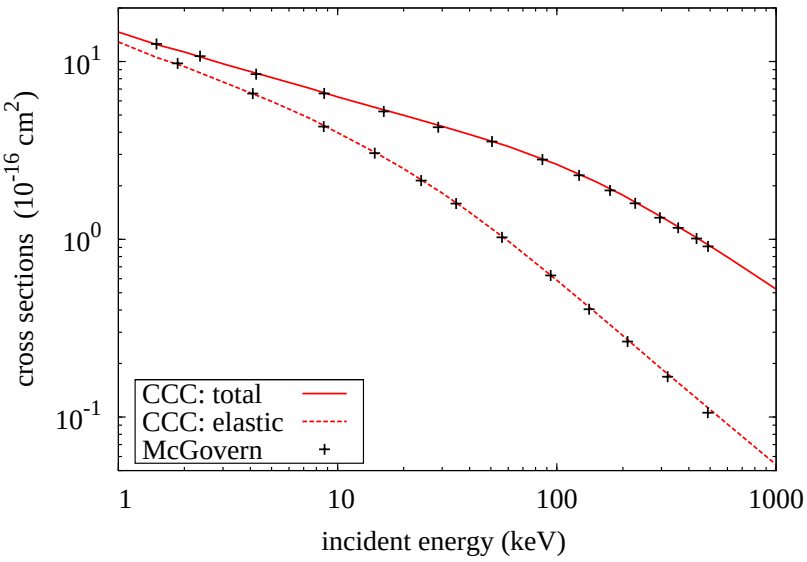

Figure 5.6: Elastic and total cross sections for antiproton-hydrogen scattering. Semiclassical impact-parameter close-coupling calculations are due to McGovern et al. [24].

Figure 5.7 shows the excitation cross sections into some low-lying sublevels

($n = 2, 3$). For comparison we also present here the results of McGovern et al. [24]. Here also a reasonably good agreement is observed in all considered cross sections. Excitation into the $2p$ sublevel is dominant in the total and comparable with the ionization cross section.

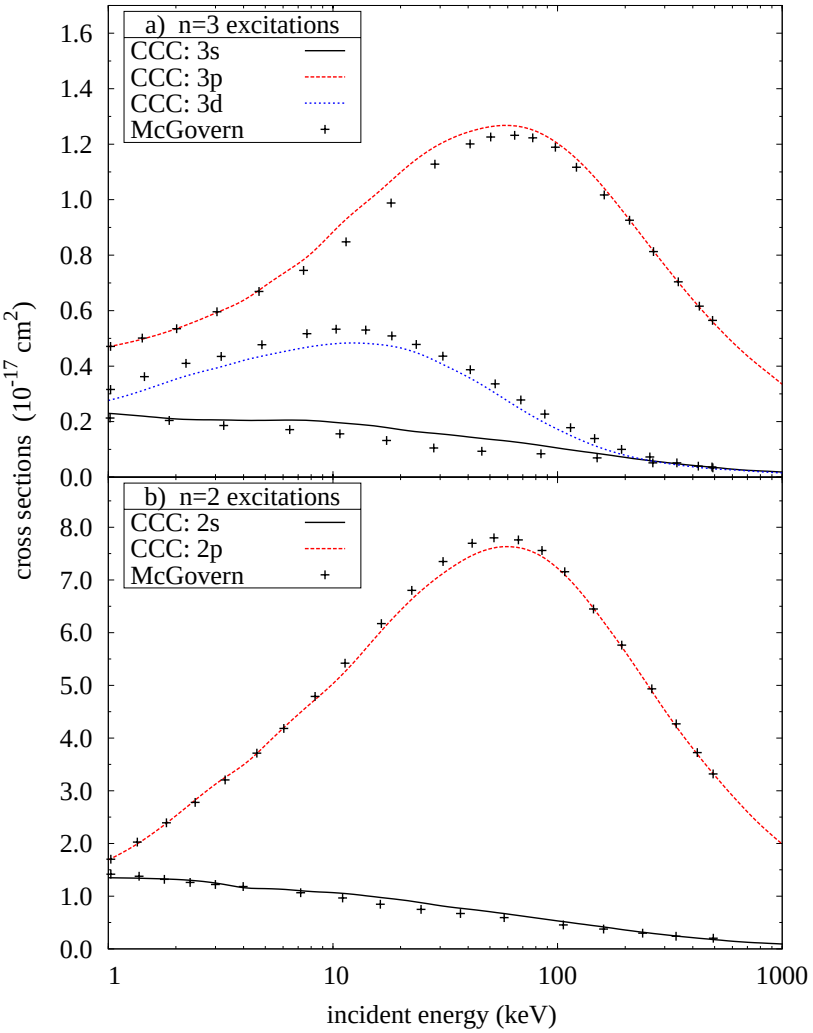

Figure 5.7: Excitation cross sections for antiproton-hydrogen scattering. Semi-classical impact-parameter close-coupling calculations are due to McGovern et al. [24].

Fig. 5.8 shows the impact parameter dependence of the weighted probabilities at three values of the incident energy. Fig. 5.8(a) displays the weighted

ionization probability bP_{ion}. Here all three curves are showing a similar trend, peaking at around $b \approx 1$ a.u. and then monotonically decreasing with increasing impact parameter. The rate of the fall off as well as the magnitude of the maximum are higher at lower incident energies. Fig. 5.8(b) displays the behavior of the weighted total probability bP_{tot}.

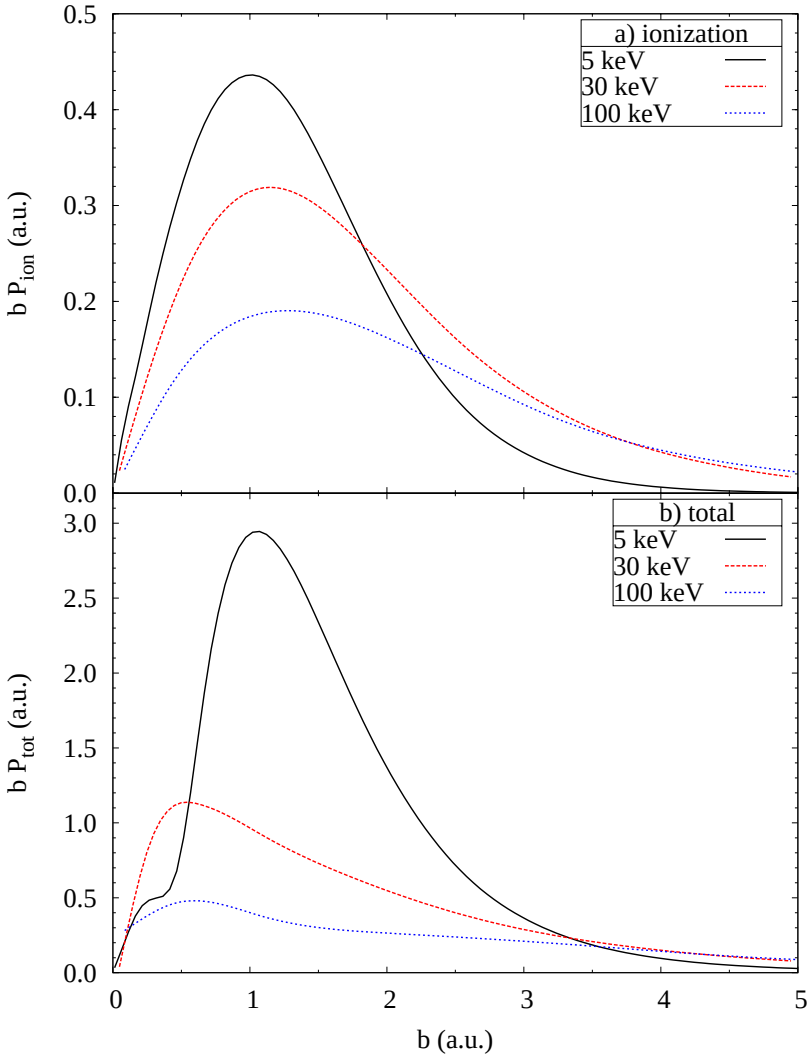

Figure 5.8: Impact-parameter dependencies of the weighted ionization and total probabilities at different incident energies of the incident antiproton colliding with atomic hydrogen.

One can note that the rate of the fall off of $bP_{\rm tot}$ is slower than that for ionization at all considered energies. In addition, the location of the maximum of the total weighted probability shifts to lower impact parameters with increasing projectile energy. An interesting feature is observed at 5 keV below $b = 0.5$ a.u. due to the oscillating character of the dominant elastic channel probability at lower energies. Although the figure is shown for the impact parameters ranging from 0 to 5 a.u., in calculations of the cross sections the range is taken as long as it is required to ensure the accuracy of the result. Typically, at the energies 5, 30 and 100 keV the cutoff points are at 7, 14 and 25 a.u., respectively.

While majority of the semiclassical methods do not take into account the Coulomb interaction between the antiproton and proton in the calculations, McGovern et al. [24] and Igarashi et al. [25] do include this interaction explicitly. However, as far as the integrated cross sections are concerned, this interaction should have no influence on the results of McGovern et al. [24] and Igarashi et al. [25]. A good agreement between their results and the results of Sahoo et al. [20] who neglected that interaction indeed supports this claim. This agreement is not surprising, since in the semi-classical treatment of ion-atom scattering the contribution of the heavy particle interaction can always be represented as a phase factor which does not contribute to the total and total ionization cross sections [71]. However, in general this is not the case. In particular in our case the treatment of the interaction between the heavy particles is critically important in the evaluation of the potential matrix elements. The fact that our fully quantum mechanical calculations yield results similar to the semi-classical ones is interesting and perhaps surprising.

5.4 Differential cross sections: Comparison with other theories

5.4.1 Details of calculations

In the previous chapter we derived analytical expressions to calculate various differential cross sections. Here we present our numerical results for triple, double and single differential ionization cross sections for antiproton-impact ionization of hydrogen. Before proceeding further we give some details of our calculations. During the calculations we always make sure that we obtain the same total ionization cross section by both summing over partial cross sections for positive-energy states (equation (4.80)) and integrating TDCS, $d^3\sigma/dE/d\Omega_e/d\Omega_p$ over all variables. This provides a check of the interpolation used in the calculations.

The pseudo-basis used for accurate calculations of integrated cross sections is not always capable of producing convergent results for differential cross sections. Usually higher l-symmetries need to be included for better description of differential ionization. Moreover, to study differential ionization at a particular electron ejection energy we need to provide a better discretization of the continuum around that interested energy. For these reasons for the calculations of differential cross sections we have utilized a larger basis which was obtained based on the convergence studies of the differential scattering results. Here also the Laguerre basis exponential fall-off is set to $\lambda_l = 1$. By fixing the basis parameter $n_{\max}$ at some sufficiently large value we studied the convergence with respect to $l_{\max}$, and found that antiproton scattering requires considerably larger $l_{\max}$ than in the case of electron scattering. We had to take into account target symmetries up to $l_{\max} = 9$, whereas in the case where the projectile is an electron $l_{\max} = 4$ was generally sufficient for similar convergence [149]. This is due to the fact that a heavy projectile like an antiproton more readily excites

the target atom to higher l-states than does a much lighter electron. Next, by setting $l_{\max} = 9$ and systematically increasing $n_{\max}$ we found that $n_{\max} = 20$ was large enough for acceptable convergence. To ensure that the employed basis was sufficiently large we were also guided by the analytical first Born (FBA) results obtained in the full wave treatment. Before performing full calculations we obtained agreement in the first Born mode. When considering cross sections at a fixed electron ejection energy we ensured a dense discretization of the continuum around that energy.

Since there is no experiment available on differential cross sections we compare some of our results with those of other theories such as CDW-EIS of Voitkiv and Ullrich [34] and the semiclassical CC of McGovern et al. [24]. Moreover, currently we restrict ourselves to the region of projectile energies higher than 30 keV where experimental data on total ionization cross sections are available [26] and well described by the CCC theory [40].

5.4.2 Triple differential cross section

In describing our results for TDCS in the collision plane we adopt the following conventions. We fix the direction of scattered antiprotons by giving either the projectile deviation angle θ_p (as in figures 5.9-5.11) or the value of the momentum transfer $\boldsymbol{p} = \boldsymbol{q}_i - \boldsymbol{q}_f$ (as in figure 5.12), while the electron ejection angle θ_e runs from $-180°$ to $180°$ relative to the direction of the momentum transfer. Since the coplanar geometry is considered the azimuthal coordinates of the ejected electron ϕ_e and the antiproton ϕ_p are set to 0.

In figure 5.9 we present our TDCS results for ejected electrons with 4 eV after the impact of 200 keV incident antiprotons on atomic hydrogen with a 0.2 mrad scattering angle.

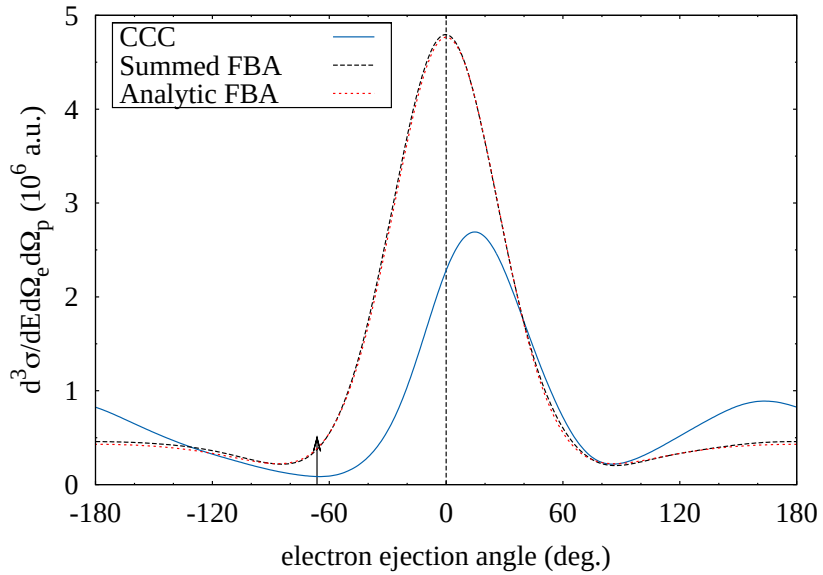

Figure 5.9: The triply differential cross section for antiproton-impact ionization of hydrogen in the scattering plane at 200 keV. The scattering angle of projectile θ_p is 0.2 mrad and the ejection energy of the electron E_e is 4 eV. The present first Born results are also presented together with the analytic first Born results. The arrow is pointing in the direction of the scattered antiproton. Electron ejection angle is the polar angle relative to the momentum transfer direction.

First, we demonstrate the excellent agreement between our expansion based first Born results and the analytic FBA. This gives us great confidence in the approach. It is seen from the figure that all displayed curves have two characteristic maxima. In the first Born approximation (curves denoted as present FBA and FBA) the peaks are observed exactly in the parallel (binary peak) and antiparallel (recoil peak) directions of the momentum transfer. However, the CCC results show their magnitudes and locations change. The binary peak of the CCC cross sections is reduced and the recoil peak is intensified, whereas they are both slightly rotated away from the scattered antiproton (the direction of the scattered antiproton is shown with an arrow in the figure). Intuitively one might expect that this is solely due to the post-collision interaction between the outgoing projectile and the ejected electron. However, the first Born approach,

which includes only the projectile-electron interaction does not produce those shifts. Our full calculations show that it is the interference of interactions of the target electron and proton with the outgoing antiproton that causes this effect. Therefore, an inclusion of the interaction between heavy particles appears to be equally important. A rather straightforward explanation for this could be that by pulling and decelerating the scattered antiproton the target proton effectively strengthens the final-state antiproton-electron interaction. This interaction leads to the polarization of the target electron cloud. As a result the electron density distribution is shifted away from the projectile path. The close-coupling formalism applied in the present work takes into account these effects.

The aforementioned effect was also seen earlier in the CDW-EIS calculations of Jones and Madison [35], Voitkiv and Ullrich [34] and in the semiclassical close-coupling calculations of McGovern et al. [24]. Jones and Madison [35] and Voitkiv and Ullrich [34] also applied their CDW-EIS approach to proton scattering on atomic hydrogen and observed the opposite effect. Due to the attractive nature of the proton-electron interaction there the beams of the ionized electrons were pulled by the outgoing protons. As a result both peaks were shifted towards the scattered projectile direction with the binary (recoil) peak increased (decreased) as opposed to the case where the projectile is an antiproton.

Now we investigate how these final-state interactions are important at various scattering angles of the projectile and the ejection energies of the electron. First we fix the ejection energy of the electron and systematically increase the scattering angle of the projectile. Figure 5.10 shows the effect of above interactions with the increasing scattering angle, while $E_{\mathrm{e}} = 4$ eV.

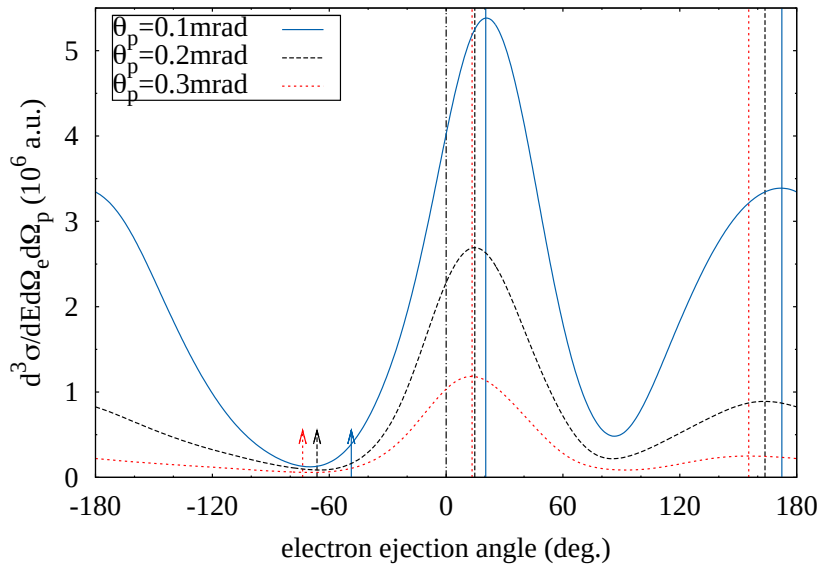

Figure 5.10: The same as for figure 5.9 but for various scattering angles.

Interestingly, as the scattering angle is increased, the location of the binary peak continuously shifts towards its location in the FBA. Compared with that of FBA, the magnitude of the binary peak is substantially less at all considered angles with the relative ratio being steadily decreased with the increasing scattering angle. As opposed to the binary peak the recoil peak slowly moves away from the location of the first Born recoil peak.

Next by fixing $\theta_p = 0.2$ mrad we examine the TDCS at different values of the ejection energy. The results are shown in figure 5.11. It is clearly seen that without any notable change in the location of the binary and recoil peaks the cross sections for electron ejection almost uniformly decrease at all angles as the ejection energy increases. This pattern indicates that emission of low energy electrons is the dominant ionization process, as might be expected.

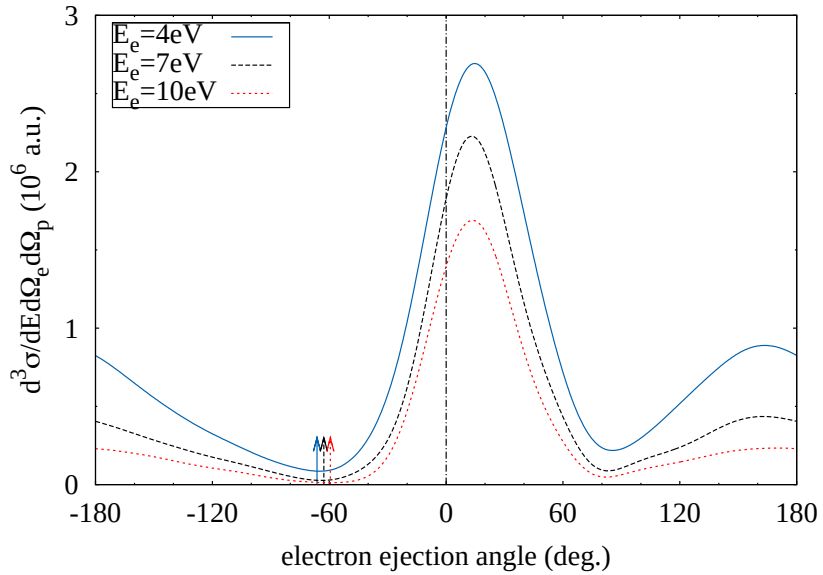

Figure 5.11: The same as figure 5.9 but for various ejection energies.

In figure 5.12 our results for the TDCS are compared with the results of other theories, namely CDW-EIS calculations of Voitkiv and Ullrich [34] and semiclassical close-coupling calculations of McGovern et al. [24]. We note that the results of other approaches are brought to the collision geometry that we have currently adopted. In addition, the semiclassical CC results of McGovern et al. [24] in the laboratory frame are converted to the TDCS in the relative coordinate system by multiplying by m_p/M_α, where m_p is the mass of antiproton. The CDW-EIS results of Voitkiv and Ullrich [34] for $d^5\sigma/d^2\boldsymbol{p}_\perp d^3\boldsymbol{\kappa}$ are different from the current $d^3\sigma/dEd\Omega_e d\Omega_p$ by the factor $k_f k_i \kappa$. Figure 5.12(a) illustrates the TDCS in the scattering plane where the perpendicular component of the momentum transfer $p_\perp = 0.7$ a.u., the antiproton is incident with $E_p = 30$ keV and the electron is ejected with $E_e = 5$ eV. Due to the relatively low projectile energy (this is close to the energy where the TICS has a maximum) here the effect of the final-state interactions is pronounced and the binary and recoil peaks shift considerably making the electron ejection suppressed in the direction of the

momentum transfer.

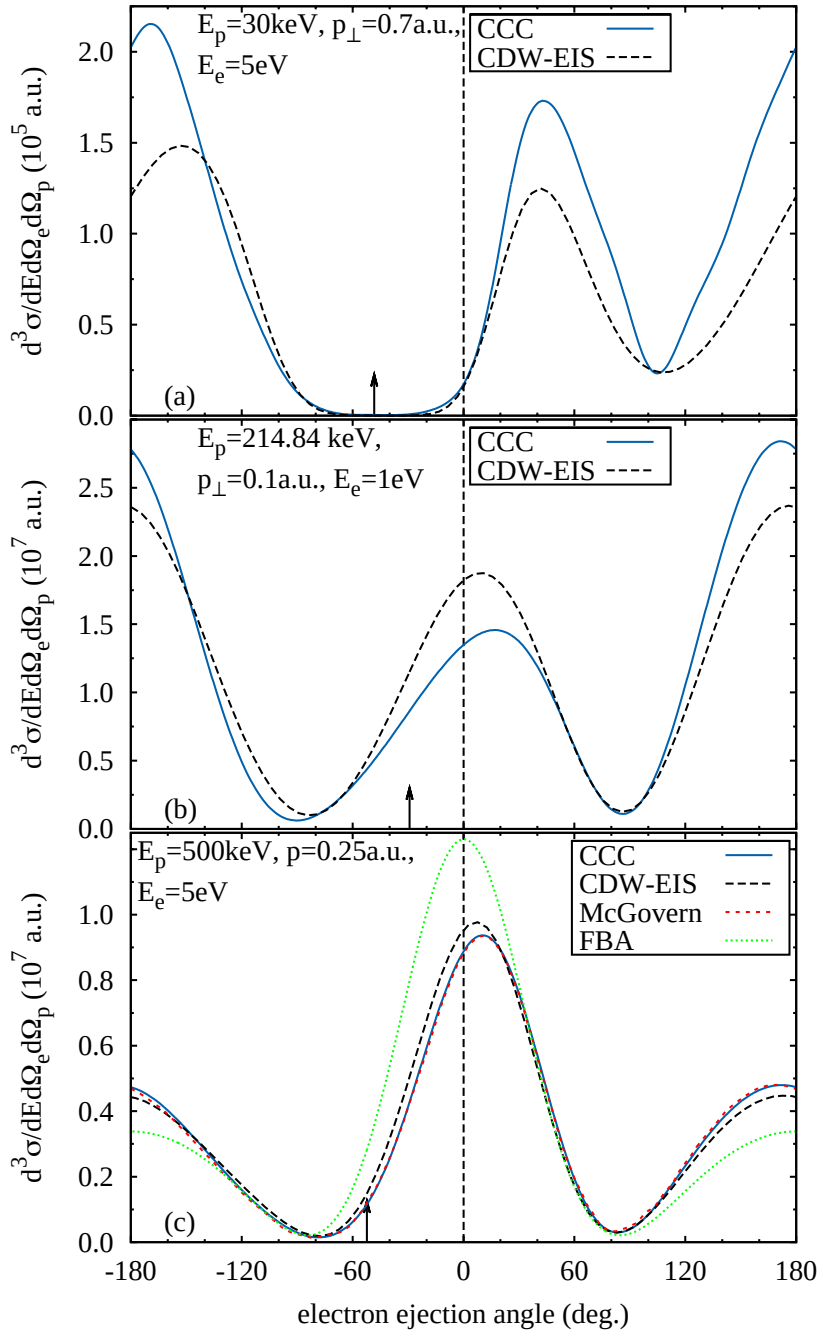

Figure 5.12: The triply differential cross sections at various scattering angles and energies of the projectile and ejected electron. Results of the CDW-EIS and semiclassical close-coupling approaches are due to [34, 150] and [24], respectively. Analytical first Born results are also presented at 500 keV.

The high energy CDW-EIS approach also predicts quantitatively the same shifts, though the magnitudes of the CDW-EIS peaks are significantly smaller than the present ones. For the considerably faster projectiles with the relative velocity $v_P = 3$ a.u. (this corresponds to the impact energy of $E_p = 214.84$ keV) the mentioned shifts are less pronounced (figure 5.12(b)). While there is also an overall good agreement in the locations of the peaks with the CDW-EIS results, the current CCC approach yields smaller binary and larger recoil peaks.

Finally, in figure 5.12(c) we consider the TDCS at the high impact energy of $E_p = 500$ keV, where the first Born approximation yields the correct TICS. As we can see in the figure the CCC results for the TDCS are still substantially different from the first Born results though the incident energy is sufficiently high. Compared with the FBA, the binary peak of the CCC cross section is reduced and the recoil peak is enhanced. However, the areas below the two curves are much the same, which explains indistinguishability of the FBA and the CCC TICS. Results of the present calculations are almost indistinguishable from the results of the semiclassical CC calculations of McGovern et al. [24], and only just distinguishable from those of the CDW-EIS theory. In line with expectations, the difference between the present CCC and the high-energy CDW-EIS results decreases with increasing collision energy.

In addition to the coplanar TDCS one can consider out-of-plane kinematics, where the electron ejected with momentum $\boldsymbol{\kappa}$ is observed in directions that do not lie in the scattering plane formed by the incident and scattered projectile momenta, $\boldsymbol{q}_i$ and $\boldsymbol{q}_f$, respectively. Such kinematically complete differential ionization experiments on antiproton-hydrogen collisions are not yet presently available but they are planned for the near future [146, 151]. Figure 5.13 displays our theoretical predictions for the out-of-plane TDCS for the electrons ejected with $E_e = 2$ eV and the antiproton with an impact energy $E_p = 30$, 50, 200 and

500 keV scattered to the angle $\theta_p = 0.2$ mrad. In these figures the antiproton is incident in the z direction and scattered on the negative x side.

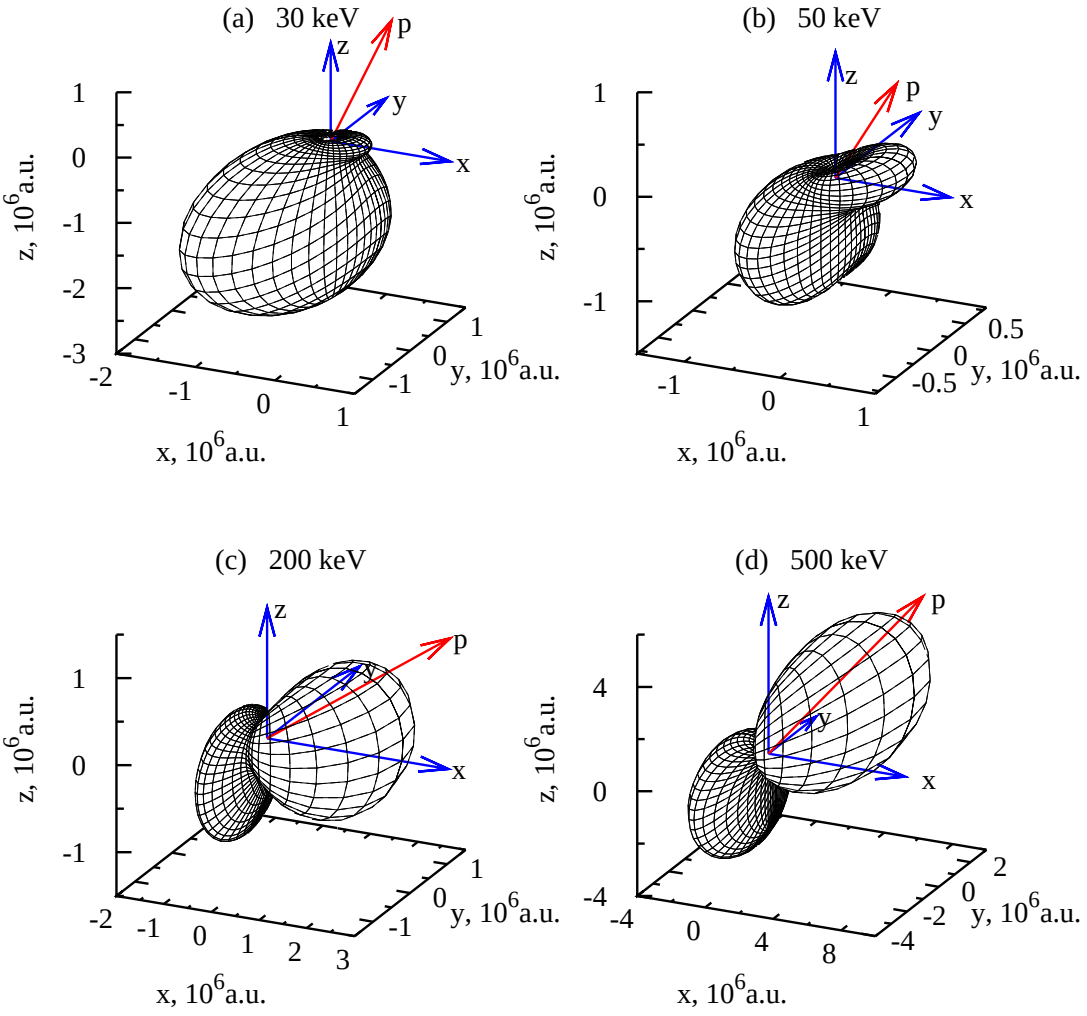

Figure 5.13: Three-dimensional plot of the triply differential cross section for antiproton-impact ionization of atomic hydrogen for an ejected electron of 2 eV (a, b and c) and 5 eV (d) in the scattering plane defined by $\theta_p = 0.2$ mrad (a, b and c) and $p = 0.25$ a.u. (d).

Whereas in the first Born approximation (not shown) the angular distribution of the ejected electrons is rotationally symmetric around the momentum transfer $\boldsymbol{p}$, in the CCC approach it deviates from the rotational symmetry. The deviation is more pronounced at lower energy of 30 (a) and 50 (b) keV than it is

at 200 (c) and 500 (d) keV. It is also worthwhile mentioning that at 30 and 50 keV the binary peak is negligibly small compared to the dominant recoil peak because of the strong repulsion of the ejected electron from the scattered antiproton. The opposite picture is observed at the higher energies (c and d), where the electron ejection is dominant in the direction of the momentum transfer.

5.4.3 Double and single differential cross sections

Figure 5.14 shows the double differential cross section, $d^2\sigma/dE/d\Omega_e$, for the ejected electron energy of $E_e = 5$ eV and various energies of the incident antiproton as a function of the electron ejection angle. Similar results obtained in the semiclassical CC approach of McGovern et al. [24] are also presented for comparison.

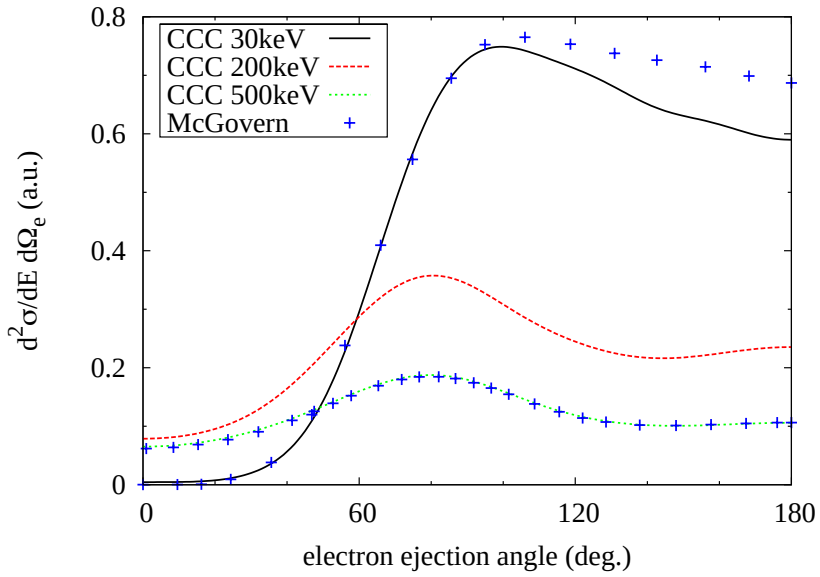

Figure 5.14: $d\sigma/dE/d\Omega_e$ for antiproton impact ionization of hydrogen at 30, 200 and 500 keV for an ejected electron of 5 eV. Semiclassical results of McGovern et al. [24] are also presented for comparison.

Since this cross section is formed as a result of integration of the TDCS

over the scattering angles of the projectile, results in figure 5.14 resemble some features of figures 5.12(a), 5.12(c) and 5.13(a) where the results of the TDCS are displayed. As expected from the patterns of figures 5.12(a) and 5.13(a) at an impact energy of 30 keV the electron emission is negligible at small ejection angles. As we go to the higher ejection angles the cross section increases until it reaches its maximum just below 100° and then slowly declines down to 0.6 a.u. at 180°. At the higher energies of 200 and 500 keV cross sections are relatively larger at small ejection angles. The pronounced peaks at around 80° and the shallow peaks at 180° are the integral results of the binary and recoil peaks of the TDCS, respectively (figures 5.13(c) and 5.13(d)). The agreement with McGovern et al. [24], particularly at 500 keV, is remarkable.

In figure 5.15 we show the same cross section $d^2\sigma/dE/d\Omega_e$ at projectile energies of 30 and 200 keV, but now as a function of the ejected electron energy as well. At both projectile energies we have a pattern of strong backward repulsion of low energy ejected electrons. This effect is more pronounced at 30 keV than at 200 keV. In both cases as the ejection energy goes up the peak in the backward direction slowly disappears and the other peak emerges at around 80°. The nature of the latter peak is related to the binary ejection.

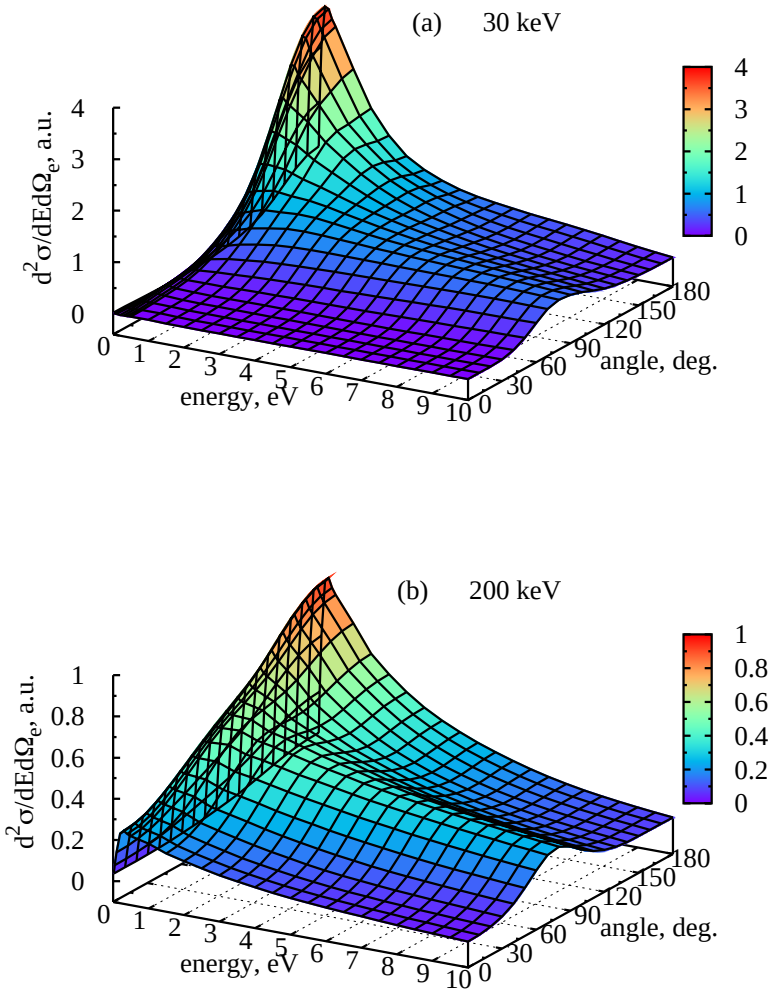

Figure 5.15: $d\sigma/dE/d\Omega_e$ at incident energies of antiproton 30 and 200 keV.

Figure 5.16 shows our results for the single differential cross section in the ejection angle of the electron $d\sigma/d\Omega_e$ in comparison with other calculations. At all considered energies the cross section is lowest in the forward direction, displays a maximum just above 60°, has a minimum around 120°, and peaks at the backward direction. Interestingly, the locations of extremum points of $d\sigma/d\Omega_e$ seem to be energy independent.

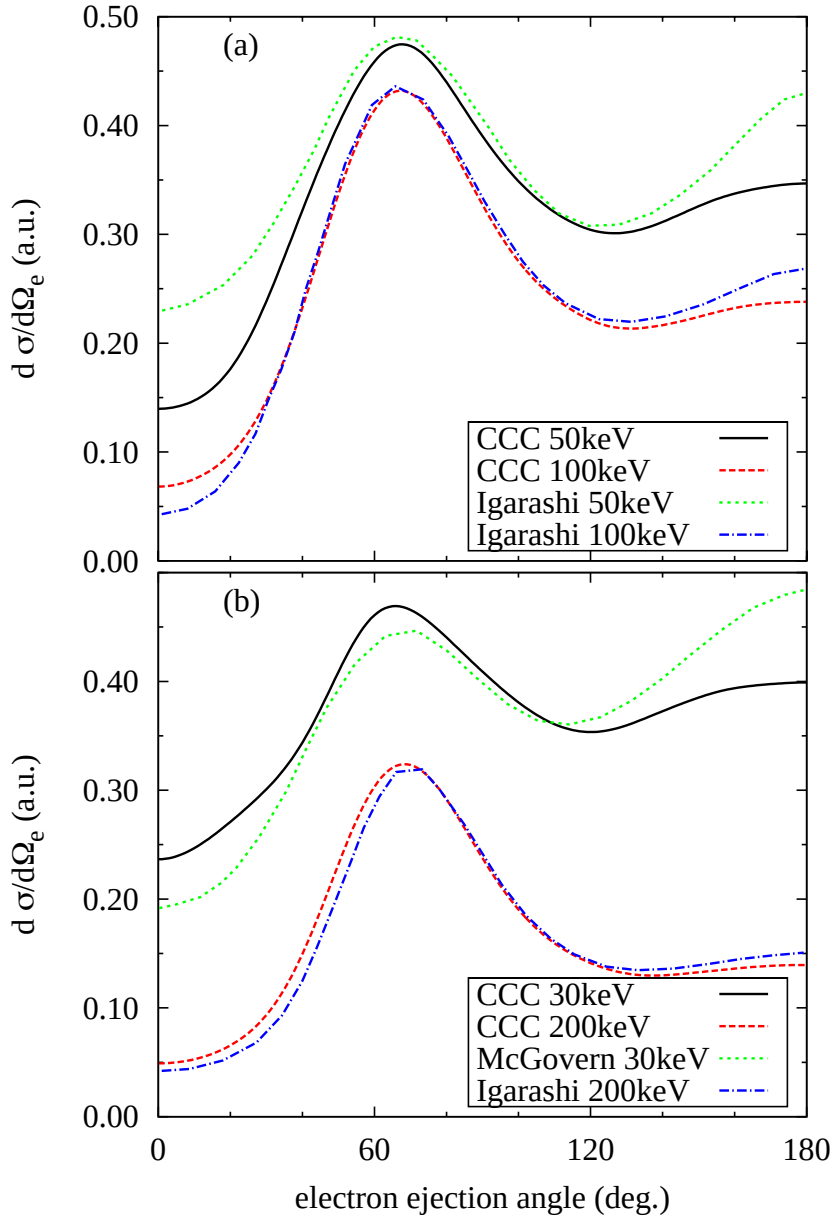

Figure 5.16: The singly differential cross section in the electron ejection angle for $\bar{p} + H(1s)$ scattering at incident energies of antiproton 30-200 keV. Results of semiclassical close-coupling approaches are due to Igarashi et al. [25] and McGovern et al. [24].

There is reasonably good agreement between the present calculations and the semiclassical coupled channel approach of Igarashi et al. [25] at higher energies,

100 and 200 keV. However, at 30 keV the present cross sections are somewhat larger in the forward, and smaller in the backward, directions compared to the results of McGovern et al. [24]. At 50 keV our predictions are somewhat smaller than the results of Igarashi et al. [25] both in forward and backward directions.

Finally, in figure 5.17 we show our results for the SDCS in the energy of the ejected electron calculated using the summation and integration methods discussed in the previous section.

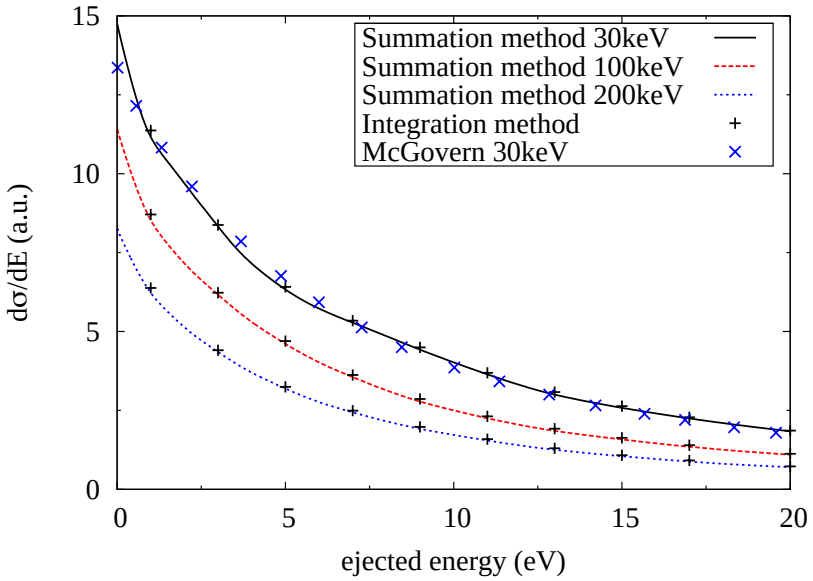

Figure 5.17: Single differential cross sections in the ejection energy of the electron at various projectile energies. Results of the semiclassical close-coupling approach are due to McGovern et al. [24].

Besides showing the energy distribution of ejected electrons, this figure also provides a testing ground for the present approach. As the summation and integration methods are independent in nature, the agreement achieved between the results they yield confirms that the numerical techniques used in the current work are internally consistent. At all considered projectile energies cross sections monotonically decrease with the increasing ejected energy. As the rate of fall is

increasing with the impact energy we can say that the ejection of slow electrons is more probable in collisions with low energy projectiles. We also emphasize that at 30 keV our results are in good agreement with the calculations of McGovern et al. [30].

5.5 Chapter summary

Integrated cross sections for various processes occurring in antiproton collisions with atomic hydrogen have been presented. The grand total, excitation and ionization cross sections have been calculated in the energy range from 1 keV to 1 MeV. The total cross section for ionization is in a good agreement with experimental measurements where available. Overall there is a good agreement between present fully quantum-mechanical integral-equation calculations and semiclassical coupled channel calculations based on the differential-equation formalism. We find that at lower energies the off-shell effects are significant. When the latter are neglected cross sections are too small at the lower energies, being somewhat similar to those obtained in perturbation methods due to weak coupling between channels.

Owing to the fully quantal treatment of the problem we have been also able to calculate various differential ionization cross sections including the fully differential one. The present results are compared with the results of semiclassical and CDW-EIS approaches. Reasonably good agreement with other calculations is found in various differential cross sections, with discrepancies becoming more apparent as the projectile energy decreases. The role of postcollisional interactions is found to be more important at lower scattering angles. Studies of cross sections with respect to the energy of the ejected electron establish the fact that the ejection of low energy electrons is the dominant ionization process.

Chapter 6

Antiproton scattering on the ground state of helium

Experimental investigations of antiproton collisions with helium is more feasible than those for atomic hydrogen. Total [36–38] and differential [39] ionization cross section measurements exist to help test theoretical approaches to the problem. In addition antiproton scattering on the He target represents the simplest system for investigating electron-electron correlation effects of the target. It is therefore important to investigate this collision system. In this chapter we will present our theoretical results on antiproton-impact single ionization of helium in the ground state. Since the target contains more than one electron there have been extensive discussions in the past about the possible effects of electron-electron correlations on the dynamics of the scattering process. In order to demonstrate the importance of these effects we will compare our results obtained in both frozen-core and multi-core approximations of the target structure. The comparison with other theoretical calculations which use various other models for describing the He structure will also be provided. Various differential cross sections calculated in the frozen-core approximation will be presented. Comparison with experiment and other theories will be made where available.

6.1 Total cross sections for helium single ionization by antiproton impact

We present our numerical results for the grand total as well as various differential single ionization cross sections. Figure 6.1 shows the total cross section for the single ionization of helium by antiproton with the incident energy ranging from 1 keV to 1 MeV. Experimentally this process has been studied on three occasions. Most recently the group in CERN [36] conducted an experiment with antiprotons at impact energies as low as 3.42 keV. These measurements exhibit a quite slow fall of the cross section with the decreasing impact energy. Two points of this set of data at about 20 and 25 keV overlap with the earlier experiment by Hvelplund et al. [38] which in turn is in overall agreement with the pioneering experiment by Andersen et al. [37]. The curves represent our frozen-core CCC results as well as the results of the semiclassical calculations by Igarashi et al. [43], McGovern et al. [24], Lee et al. [45] utilising a similar treatment of the target. Here we refer to the presented calculations with a single acronym FC, since they all start off by diagonalizing the helium Hamiltonian in a suitable two electron basis with the assumption that the inner electron is always the He^+ 1s orbital. The only difference between these methods in terms of the target structure is that different representations of the radial part of the target wave function are used. Lee et al. [45] used Slater-type orbitals (STOs), Igarashi et al. [43] – the Sturmian functions and the Laguerre functions are utilized by McGovern et al. [24]. The crosses show the one-active-electron (OAE) calculations of Pindzola et al. [48] with the Hartree local exchange potential. These results are considerably larger than the other FC calculations as well as the experiments. They concluded that the electron correlation effects of the target, not included in the OAE calculations, play a significant role. The other calculations are in quite good agreement with each other and the experiment over most of the energy range.

Next we turn our attention to MC results.

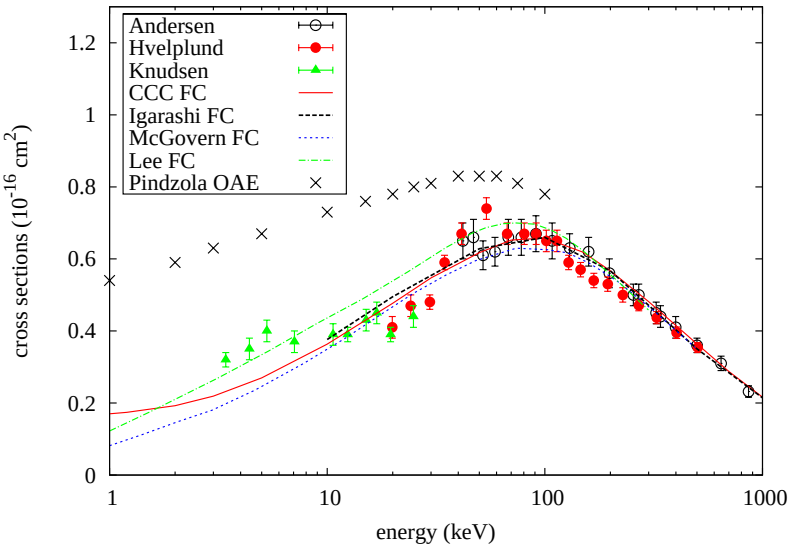

Figure 6.1: Total single ionization cross section for antiproton-helium scattering. Experimental data by Knudsen et al. [36] (▲), Hvelplund et al. [38] (●) and Andersen et al. [37] (○). Various frozen-core (FC) semiclassical close-coupling calculations are due to Igarashi et al. [43], McGovern et al. [24], and Lee et al. [45]. The one-active-electron semiclassical close-coupling calculations are due to Pindzola et al. [48]. The present frozen-core calculations are denoted by CCC FC.

Figure 6.2 compares the experimental data with the present (which are given in numerical form in the appendix in Table C.2) and other calculations which allow multiple configurations (MC) for the core electron. Whereas we allow the inner electron to take all excited states with maximum principal quantum number $n_{\max} \leq 4$, Igarashi et al. [43] limits the number of excited core states to $n_{\max} = 3$. In addition to the discrete doubly excited states, the calculations by Foster et al. [47], Guan and Bartschat [16] and Pindzola et al. [48] also include double ionization states. Apart from the results of Guan and Bartschat [16], which are systematically lower, there is good agreement between the various MC calculations over the entire energy range. What is particularly interesting is

the comparison with the FC result, given only for the CCC theory. At energies above 100 keV the MC results are slightly lower than the FC ones. However, at lower energies the MC results are substantially larger. Following a similar study for electron scattering [94], we might have expected that an increase in the ionization threshold would result in a systematic drop of the total ionization cross section. Perhaps this is still the case at energies above 100 keV, but we are unable to find a definitive argument why the MC-calculated cross sections should be above the FC ones at low energies. We do note that unlike the case where the projectile is an electron, the velocity of the antiproton at these energies is much lower than the orbiting electron. Consequently the comparison of the two projectiles is more appropriate at higher energies.

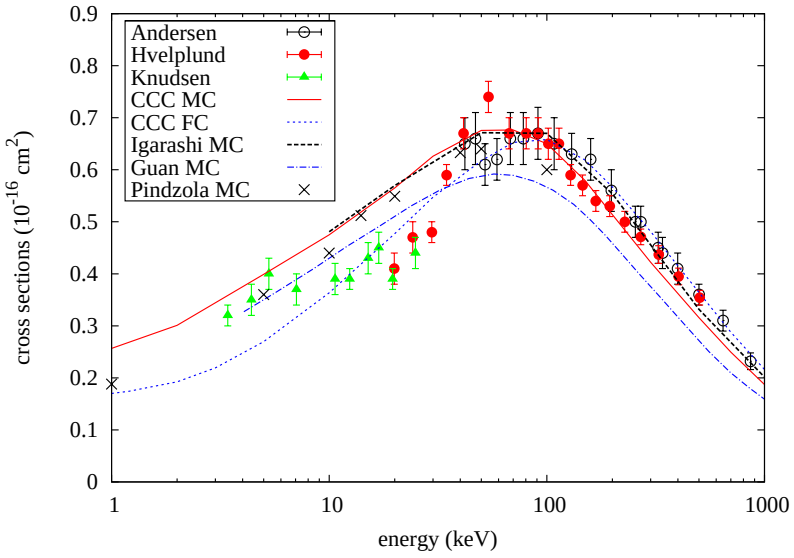

Figure 6.2: Total single ionization cross section for antiproton-helium scattering. Experimental data by Knudsen et al. [36] (▲), Hvelplund et al. [38] (●) and Andersen et al. [37] (○). Various multiconfigurational (MC) semiclassical close-coupling calculations are due to Igarashi et al. [43], Guan and Bartschat [16], and Pindzola et al. [48]. The present multiconfigurational calculations are denoted by CCC MC. The CCC FC results are also presented.

6.2 Differential cross sections for single ionization of helium by antiproton impact

As already mentioned in Chapter 4 by sequentially integrating the fully differential ionization cross section, Eq. (4.74), over angular variables of the scattered antiproton and the ejected electron we can find various double and/or single differential ionization cross sections. Carrying out kinematically complete experiments is a complicated task due to the difficulties related with the production of a stable high intensity antiproton beam. However, the recent development of recoil-ion and ejected electron momentum spectroscopy makes accurate measurements of differential cross sections in the momenta of these particles possible. In fact, the recoil ion carries as much information on the three-body ionization dynamics as the projectile and the ejected electron. Such a pioneering experiment [39] on antiproton impact ionization of He has already been reported at 945 keV measuring the single differential cross section as a functions of the longitudinal recoil-ion and the ejected electron momenta. These quantities can be obtained from the double differential ionization cross section $d^2\sigma(q_f, q_i, \boldsymbol{\kappa})/dEd\Omega_e$ if we impose the following dynamic constraints required by the energy and momentum conservation:

$$p_{r\|} = p_{\|} - \kappa_{\|} = \frac{\epsilon_f - \epsilon_0}{v} - \kappa\cos\theta_e, \tag{6.1}$$

where $p_{r\|}$ and $\kappa_{\|}$ are, respectively, the longitudinal momenta for the recoil ion and the ionized electron, and $p_{\|}$ is the longitudinal projectile momentum transfer. With this we can write

$$\frac{d\sigma}{d\kappa_{\|}} = \int_{\kappa_{\|}^2/2}^{\infty} \frac{1}{\kappa}\frac{d^2\sigma}{dEd\Omega_e}dE, \tag{6.2}$$

and

$$\frac{d\sigma}{dp_{r\|}} = \int_{\epsilon^-}^{\epsilon^+} \frac{1}{\kappa}\frac{d^2\sigma}{dEd\Omega_e}dE. \tag{6.3}$$

The integration limits of (6.3) can be obtained from (6.1) or relationship

$$\kappa^{\pm} = v\cos\theta_e \pm \sqrt{v^2\cos^2\theta_e + 2(p_{r\|}v - |\epsilon_0|)} \tag{6.4}$$

using $\epsilon^{\pm} = (\kappa^{\pm})^2/2$.

Figure 6.3 shows the ejected-electron longitudinal momentum distribution in single ionization of helium by antiproton impact at 945 keV. We compare our FC results with the experimental data of Khayyat et al. [39] and other calculations. Apart from the CTMC calculations, there is a reasonably good agreement between the various theories and experiment. The CCC results are only slightly better than the Born approximation. The difference from the Born results is still significant despite the relatively high energy being considered.

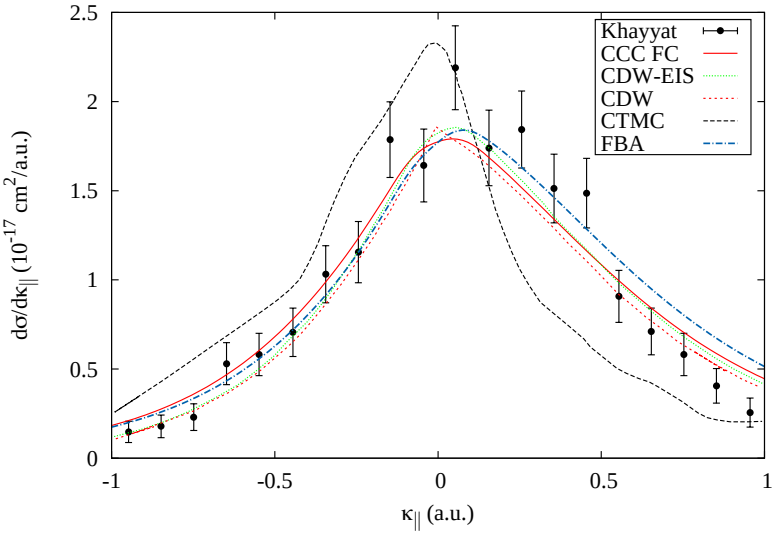

Figure 6.3: Ejected-electron longitudinal momentum distribution for single ionization of helium by 945 keV antiproton impact. Experimental data (•) and CDW and CTMC calculations are due to Khayyat et al. [39]. CDW-EIS calculations are due to Fainstein and Rodriguez [152]. The present frozen-core calculations are denoted by CCC FC. First Born results are also shown.

The corresponding recoil-ion longitudinal momentum distribution is given in the next Fig. 6.4. Once more only the CTMC approach clearly fails to describe

the experiment. Perhaps the CDW results show a systematic discrepancy at the positive momentum values. We note however that the considered impact energy is so large that even the simplest first Born approximation (FBA) is not significantly different from the present results and other more sophisticated perturbation methods. Similar measurements, but at lower impact energies, would be helpful in testing the theoretical approaches to fully differential ionization by antiproton impact.

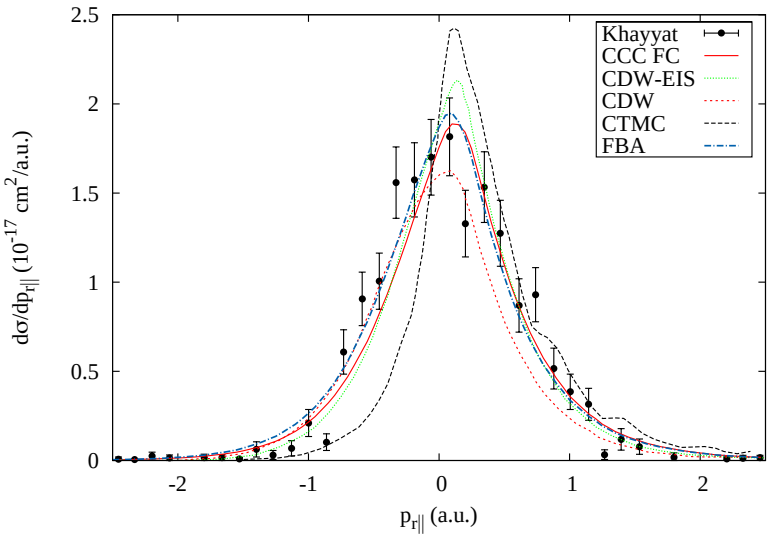

Figure 6.4: Recoil-ion longitudinal momentum distribution for single ionization of helium by 945 keV antiproton impact. Experimental data (•) and CDW and CTMC calculations are due to Khayyat et al. [39]. CDW-EIS calculations are due to Fainstein and Rodriguez [152]. The present frozen-core calculations are denoted by CCC FC. First Born results are also shown.

To demonstrate how the Born and CCC results differ at lower energies, we present in figure 6.5 similar results at energies 100 and 300 keV. In line with our expectations the differences between the CCC FC and the first Born distributions increase as the impact energy decreases. Interestingly, as we go down in impact energy the results exhibit a two-maxima structure which is more

pronounced at lower energies. We note that the magnitude of the longitudinal momentum distribution gets larger with the decreasing incident energy.

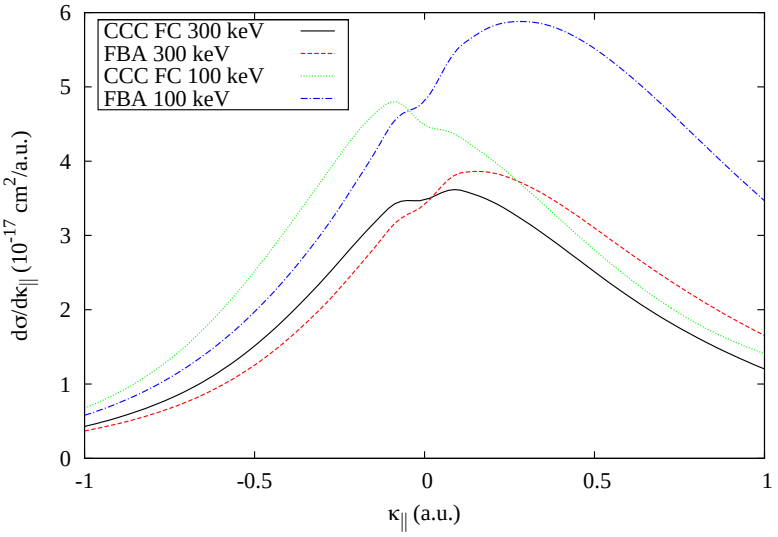

Figure 6.5: Ejected electron longitudinal momentum distribution for single ionization of helium by antiproton impact at various incident energies. Relevant first Born results are also presented for comparison.

Finally we report that in addition to the longitudinal momentum distributions, by carrying out a fully quantum mechanical CCC approach we can give any differential cross section for the single ionization of He by antiproton impact. This was shown recently in the case of antiproton-hydrogen scattering [102]. As an example we give in figure 6.6 the three-dimensional picture of the fully differential cross section for the 100 keV antiproton impact single ionization of He with the ejected electron energy of 5 eV and a momentum transfer of $\boldsymbol{p} = 0.6$ a.u.. In this figure the antiproton is incident in the z direction and scattered in the negative x direction. Whereas the Born approach (not shown) produces the rotationally symmetric angular distribution of the ejected electrons around the momentum transfer $\boldsymbol{p}$, in the CCC FC approach, this distribution strongly deviates from the rotational symmetry. At this impact energy the post-collision

interaction becomes significant. Due to the strong repulsion of the ejected electron from the scattered antiproton the binary peak is smaller than the recoil peak.

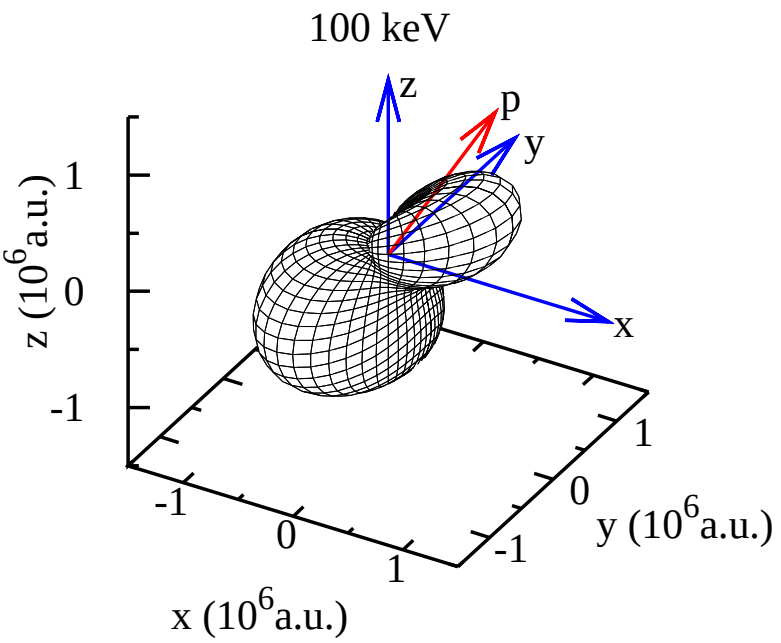

Figure 6.6: Three-dimensional plot of the triply differential cross section for antiproton-impact single ionization of helium at 100 keV. The scattering plane defined by $\boldsymbol{p} = 0.6$ a.u. and the ejection energy of the electron is 5 eV. The arrow is pointing in the direction of the momentum transfer.

6.3 Chapter summary

Antiproton induced single ionization of helium has been studied theoretically. To demonstrate the role of electron correlations in the target the frozen-core and multi-core calculations for the integrated cross section have been performed. Results have been compared with available experimental data and calculations by other groups. Though both the frozen-core and multi-core calculations yield generally good agreement with experiment for the total ionization cross sections, the MC ones are substantially higher at the lower energies than the frozen-core ones. This fact contradicts with findings in case of electron scattering on the the same target. However, the comparison of the two projectiles might be not appropriate since at the same energy the velocity of the antiproton is much lower than the orbiting electron. Good agreement between the present fully quantum-mechanical calculations and the semiclassical ones at energies considered in this thesis indicates that for calculations of integrated cross sections the widely used straight-line approximation for relative motion of the antiproton and residual helium ion is reliable. The same cannot be said with confidence when differential cross sections are concerned. Calculated longitudinal ejected electron and recoil-ion momentum distributions for the single ionization of helium are in good agreement with the experiment and other perturbative calculations. However, the agreement with other first order calculations becomes less satisfactory at lower energies where the post-collision interaction between the scattered antiproton and the ejected electron becomes significant.

Chapter 7

Conclusions

Based on the inconclusive status of low-energy antiproton collision studies and also motivated by the future-planned kinematically complete experiments for antiproton-induced ionization of various atoms, four main objectives were specified for this thesis. These were a (i) development of the fully quantum-mechanical method to antiproton-atom collisions, (ii) rigorous testing of the developed method, (iii) performing extensive comparison between the obtained fully quantum-mechanical and the previously reported semiclassical results for integrated cross sections for various processes occurring during the collision. Furthermore, owing to the fully quantum-mechanical nature of the method it was required to test it for the ability to provide (iv) various differential cross sections including the fully differential cross section.

In order to develop the fully quantum-mechanical approach to the antiproton-atom scattering problem we have followed the basic concepts of the convergent close-coupling (CCC) method which has been highly successful in dealing with light projectiles, such as electrons and positrons. Based on the original CCC formalism the total wave function has been expanded in terms of square-integrable Laguerre pseudostates of the target. Using this expansion the time-independent Schrödinger equation for the total wave function, which explicitly includes in-

teractions among all involved particles, has been transformed into the coupled-channel Lippmann-Schwinger (LS) integral equations in momentum space. Since in the case of heavy projectiles the well known technique of partial-wave decomposition of LS equations becomes inefficient, two new numerical methods have been developed to solve these equations. In the first, direct-integration method, the LS equations are converted into a matrix equation. The obtained set of linear equations is solved using standard computer packages, such as LAPACK [153] or SCALAPACK [154]. To demonstrate the performance of the direct-integration method in practice we have considered the problem of proton and antiproton scattering on atomic hydrogen. To start with we have constructed the total scattering wave function using only the ground states of atomic hydrogen in the direct and rearrangement channels. For antiproton-hydrogen collisions we have calculated integrated and differential cross sections for the elastic scattering channel whereas for the proton projectile similar results have been obtained also for the electron transfer process. The contribution of off-shell effects is found to be significant. From comparison of obtained results with experiment we conclude that even for the accurate description of the electron-capture process it is essential to include ionization channels. Our calculations within the simple two-state model show that implementation of the direct integration method to the multi-channel problem is presently not feasible due to large memory requirements.

For the full treatment of ion-atom collisions including all major channels we have developed an approach where the coupled-channel LS equations in momentum space are transformed into the mathematically equivalent impact-parameter space. The emerging set of one-dimensional integral equations in the impact-parameter representation, after conversion into a matrix equation, is solved in the same way as it is done in the direct-integration method using standard linear

algebra routines. In order to numerically test the code for the impact-parameter formalism we have performed one state (only the elastic scattering channel is considered) calculations for the angular differential cross section and compared the results with those obtained by the direct-integration method which does not use any approximation. The perfect agreement at all scattering angles suggested that the impact-parameter transformation method can indeed give reliable results. Using this method we have considered the scattering of antiprotons with atomic hydrogen and helium. However, the formalism is derived in a form that can easily be generalised to include rearrangement channels and is applicable for both antiprotons and protons as projectiles. Also, the method can be applied to more complex targets with one active electron. The only requirement is to generate pseudostates which accurately describe the electronic structure of the target. For the hydrogen target, the pseudostates have been obtained from diagonalization of the target Hamiltonian on the basis of one-electron orbitals made of Laguerre functions. To obtain the He pseudostates we have used the configuration-interaction approach which accurately accounts for the electron-electron correlation effects.

Various integrated and differential cross sections have been calculated for processes taking place in antiproton collisions with atomic hydrogen and helium. In this thesis we have considered projectile energies ranging from 1 keV to 1 MeV. The calculations have converged faster for higher impact energies than for lower energies. The present fully quantum-mechanical results for antiproton-impact total ionization of hydrogen are in excellent agreement with experiment. For antiproton-induced total ionization of a single electron of helium we have performed two types of calculations – the frozen-core (FC), where we assumed that the inner electron of the target was always in the $He^+(1s)$ orbital, and the multi-configurational, where we relaxed the FC approximation allowing the

inner electron to occupy also a few low-lying orbitals. Both the FC and MC calculations yield generally good agreement with the experimental data. Interestingly, more accurate MC results, which account for the electron correlations of the target, are substantially higher than the FC ones at low impact energies. Various differential cross sections for antiproton-impact ionization of both targets have been calculated and compared with the results of semiclassical and continuum-distorted-wave eikonal-initial-state (CDW-EIS) approaches over a wide incident energy range. We conclude that the discrepancy between the present results and the first Born calculations gets systematically larger as the energy decreases. Also, it is found that at lower energies the contribution of postcollisional interactions to the differential ionization cross section become significant. Owing to the fully quantum-mechanical treatment of the problem we believe that the presently obtained results for differential cross sections are reliable.

Finally, it is important to note that for both targets there is reasonable agreement between the present integrated cross sections calculated using the fully quantum-mechanical approach and those calculated using the semiclassical models. Thus, it can be concluded that for calculations of integrated cross sections the straight-line approximation which is usually used by semiclassical theories to describe the relative motion of the antiproton and the target nuclei is reliable at energies considered in this thesis.

Appendix A

Derivation of helium radial pseudostates

The CCC approach uses target wave-functions that are square-integrable. They produce sufficiently accurate low-lying bound states and discretized positive energy states to resemble the continuum. Because of two-electron correlations, obtaining the He structure is a complicated process with no analytical solution. Below a configuration interaction (CI) approximation to describing the He structure is presented.

In the nonrelativistic approach the Hamiltonian $H_{\rm T}$ of the helium atom can be written as

$$H_{\rm T} = \sum_{i=1}^{2} \left(\frac{1}{2}\nabla_i^2 + \frac{Z}{r_i} \right) + \frac{1}{|\mathbf{r}_1 - \mathbf{r}_2|}. \tag{A.1}$$

As the spin-orbit interactions are neglected in the nonrelativistic Hamiltonian $H_{\rm T}$, it conserves the parity π and the total orbital l and spin s angular momenta. Therefore it is convenient to use the LS-coupling scheme in which the helium wave functions Ψ_α are characterized by the orbital angular momentum l, spin s, and parity π. For brevity of notations we use index α to denote the full set of quantum numbers (n, l, s, π). The He wavefunctions are obtained from the

solution of the Schrödinger equation

$$H_{\mathrm{T}}\,\Psi_\alpha = \epsilon\,\Psi_\alpha. \tag{A.2}$$

An analytical solution of (A.2) does not exist and therefore several approximations have been used to solve it numerically. One such approach is the configuration interaction (CI) method. In the CI approach it is assumed that the helium wave function can be represented as

$$\Psi_\alpha = \sum_{i=1}^{N} C_i^\alpha \Phi_i^{ls\pi}, \tag{A.3}$$

where $\Phi_i^{ls\pi}$ are antisymmetrized two-electron functions (configurations), C_i^α are the CI coefficients and N is the number of configurations.

The target states and energies are obtained by solving the generalized eigenvalue problem for a given CI basis $\Phi_i^{ls\pi}$

$$\sum_{i=1}^{N} \left(\langle \Phi_j^{ls\pi} | H_{\mathrm{T}} | \Phi_i^{ls\pi} \rangle - \epsilon \langle \Phi_j^{ls\pi} | \Phi_i^{ls\pi} \rangle \right) C_i^\alpha = 0. \tag{A.4}$$

Note that the latter equation is written in its general form which does not require the CI basis to be an orthogonal basis. By solving the eigenvalue problem (A.4) we obtain N partial solutions which correspond to N helium target states. These states may be written as

$$\Psi_\alpha = \sum_{i=1}^{N} C_i^\alpha \Phi_i^{ls\pi}, \tag{A.5}$$

and satisfy

$$\langle \Psi_\alpha | H_{\mathrm{T}} | \Psi_{\alpha'} \rangle = \epsilon_\alpha \delta_{\alpha\alpha'}. \tag{A.6}$$

Here the indices α and α' denote the helium states for the given combination (l, s, π).

Each configuration $\Phi_i^{ls\pi}$ is constructed from antisymmetric combinations of one-electron functions coupled to yield total orbital angular momentum l, total

spin s and parity π by writing

$$\Phi_i^{lms\nu\pi} = \frac{1}{\sqrt{2(1+\delta_{ab})}} \sum_{m_a m_b \sigma_1 \sigma_2} C^{lm}_{l_1 m_1 l_2 m_2} C^{s\nu}_{\frac{1}{2}\sigma_1 \frac{1}{2}\sigma_2} \left[\phi_a(x_1)\phi_b(x_2) - \phi_a(x_2)\phi_b(x_1)\right], \tag{A.7}$$

where $C^{j_3 m_3}_{j_1 m_1 j_2 m_2}$ is a Clebsch-Gordan coefficient and x denotes spatial and spin coordinates. The one-electron orbital $\phi_{a(b)}(x_i)$ is a product of a radial function, a spherical harmonic, and a spin function, i.e.

$$\phi_{a(b)}(x_i) = \phi_{a(b)}(\mathbf{r}_i)\chi_{\frac{1}{2}\sigma_i} = \frac{1}{r_i} R_{k_a l_i}(r_i) Y_{l_i m_i}(\widehat{\mathbf{r}}_i)\chi_{\frac{1}{2}\sigma_i}. \tag{A.8}$$

The parity of the configuration (A.7) is defined by

$$\pi = (-1)^{l_a + l_b}. \tag{A.9}$$

It is convenient to separate the spin functions in (A.7) and recouple the orbital angular momenta to obtain

$$\begin{aligned} \Phi_i^{lms\nu\pi} =& \chi_{s\nu}(12) \frac{1}{\sqrt{2(1+\delta_{ab})}} \left(1 + (-1)^s (-1)^{l_a + l_b - l} P_{ab}\right) \\ & \times \sum_{m_a m_b} C^{lm}_{l_a m_a \, l_b m_b} \phi_a(\mathbf{r}_1)\phi_b(\mathbf{r}_2), \end{aligned} \tag{A.10}$$

where the operator P_{ab} interchanges the indices a and b, and the two-electron spin function is defined by

$$\chi_{s\nu}(12) = \sum_{\sigma_1 \sigma_2} C^{s\nu}_{\frac{1}{2}\sigma_1 \frac{1}{2}\sigma_2} \chi_{\frac{1}{2}\sigma_1}(1)\chi_{\frac{1}{2}\sigma_2}(2). \tag{A.11}$$

The orbitals ϕ_α and ϕ_β form a configuration $\Phi_i^{ls\pi}$ that is included in the CI expansion (A.3) if the following selection rules are satisfied

$$\begin{aligned} |l_\alpha - l_\beta| &\leq l \leq l_\alpha + l_\beta, \\ \pi &= (-1)^{l_\alpha + l_\beta}, \\ (-1)^{l+s} &= 1 \text{ if } \varphi_\alpha = \varphi_\beta. \end{aligned} \tag{A.12}$$

Using Eq. (A.10) we can write matrix elements of $H_{\rm T}$ in the following way

$$\begin{aligned}\langle\Phi_j^{ls\pi}|H_{\rm T}|\Phi_i^{ls\pi}\rangle &= \frac{1}{2\sqrt{(1+\delta_{\alpha\beta})(1+\delta_{\gamma\delta})}}\left(1+(-1)^s(-1)^{l_\alpha+l_\beta-l}P_{\alpha\beta}\right)\\ &\times\left(1+(-1)^s(-1)^{l_\gamma+l_\delta-l}P_{\gamma\delta}\right)\left[2V_1+V_{12}\right],\end{aligned} \tag{A.13}$$

where antisymmetry of the configurations $\Phi_j^{ls\pi}$ has been used. The one-electron matrix elements V_1 can easily be reduced to

$$V_1=\langle\phi_\beta|\phi_\delta\rangle\delta_{l_\alpha l_\gamma}\int dr_1 R_\alpha(r_1)[-\frac{1}{2}(\frac{d^2}{dr_1^2}-\frac{l_\alpha(l_\alpha+1)}{r_1^2})-\frac{Z}{r_1}]R_\gamma(r_1), \tag{A.14}$$

where the overlap integral between the one-electron orbitals is given by

$$\langle\phi_\beta|\phi_\delta\rangle=\delta_{l_\beta l_\delta}\int dr\ R_\beta(r)R_\delta(r). \tag{A.15}$$

Calculating the two-electron matrix elements V_{12} is a little more challenging. To calculate two-electron matrix elements we first use the multipole expansion of the electron-electron potential

$$\frac{1}{|\mathbf{r}_1-\mathbf{r}_2|}=4\pi\sum_{\lambda,\mu}\frac{1}{2\lambda+1}\frac{r_<^\lambda}{r_>^{\lambda+1}}Y_{\lambda\mu}(\hat{\boldsymbol{r}}_1)Y^*_{\lambda\mu}(\hat{\boldsymbol{r}}_2)). \tag{A.16}$$

Using (A.16) and after some angular algebra we get

$$V_{12}=\sum_\lambda(-1)^{l_\beta+l_\gamma+l}\sqrt{(2l_\gamma+1)(2l_\delta+1)}C^{l_\alpha 0}_{l_\gamma 0\,\lambda 0}C^{l_\beta 0}_{l_\delta 0\,\lambda 0}\left\{\begin{array}{ccc} l_\alpha & l_\beta & l\\ l_\delta & l_\gamma & \lambda\end{array}\right\}\mathcal{R}_\lambda(\alpha,\beta,\gamma,\delta), \tag{A.17}$$

where the radial integral is given by

$$\mathcal{R}_\lambda(\alpha,\beta,\gamma,\delta)=\int\int dr_1dr_2\,\frac{r_<^\lambda}{r_>^{\lambda+1}}R_\alpha(r_1)R_\beta(r_2)R_\gamma(r_1)R_\delta(r_2). \tag{A.18}$$

The range of allowed values of λ is determined by the triangle rule for Clebsch-Gordan coefficients in (A.17).

The matrix element V_{12} is symmetric over simultaneous interchange of indices α with β and δ with γ. This property is used to speed up the calculations.

In order to calculate the radial integrals in (A.18) and (A.14) we must choose the radial functions $R_\alpha(r)$. We take the radial part of the single-particle functions to be the Laguerre basis

$$R_{kl}(r) = \left(\frac{\lambda_l(k-1)!}{(2l+1+k)!}\right)^{1/2} (\lambda_l r)^{l+1} \exp(-\lambda_l r/2) L_{k-1}^{2l+2}(\lambda_l r), \quad \text{(A.19)}$$

where the $L_{k-1}^{2l+2}(\lambda_l r)$ are the associated Laguerre polynomials, and k ranges from 1 to the basis size N_l. For a given λ_l, the Laguerre functions $R_{kl}(r)$ form an orthonormal basis which leads to an orthonormal CI basis $\Phi_i^{ls\pi}$.

The two-electron radial integrals (A.18) are evaluated numerically. In the calculation of the one-electron matrix elements (A.14) the differentiation is first taken analytically according to the following relation

$$\begin{aligned}\frac{d^2}{dr^2}\phi_{kl}(r) &= \left(\frac{\lambda_l(k-1)!}{(2l+1+k)!}\right)^{1/2} \lambda^2(\lambda_l r)^l \exp(-\lambda_l r/2) L_{k-2}^{2l+3}(\lambda_l r) \\ &\quad + \left(\frac{l(l+1)}{r^2} - \frac{\lambda(k+l)}{r} + \frac{\lambda^2}{4}\right)\phi_{kl}, \end{aligned} \quad \text{(A.20)}$$

and the integral is then evaluated numerically.

Appendix B

Proof of Eq. (4.62)

Here we prove that the overlap Eq. (4.60) between the radial Coulomb wave with momentum κ and a pseudostate of energy ϵ_{nl} and momentum κ_{nl} is identically zero whenever $\kappa = \kappa_{n'l}$ where $n' \neq n$.

For this purpose we use the known analytic expansion for the radial Coulomb wave given by Yamani and Reinhardt [137]

$$U_l(\kappa, r) = \sum_{m=0}^{\infty} B_m^l(\kappa) P_m^l(x) \varphi_{ml}(r) \tag{B.1}$$

where the P_m^l are Pollaczek polynomials in the variable x simply related to the momentum κ and the $\varphi_{ml}(r)$ are Laguerre functions that are similar to $\xi_{ml}(r)$ of Eq. (4.32) except that the Lagerre polynomials in the definition are replaced by $L_m^{2l+1}(r)$. The details of deriving (B.1) are given in [137]. The $\varphi_{ml}(r)$ are not orthogonal but are closely related to the $\xi_{ml}(r)$ since $L_m^{2l+1}(r) = L_m^{2l+2}(r) - L_{m-1}^{2l+2}(r)$. If the basis φ_{ml}, $n = 0, 1, ..., \infty$ is truncated to $m = 0, 1, .., N$ the solution of the Schrödinger equation generates pseudostates $R_{nl}(r)$ with energies ϵ_{ml}, $m = 1, .., N$. Yamani and Reinhardt showed that the eigenvalues

for energy were given as the N roots of the Polynomial equation

$$P_N^l(x = x(\epsilon_{ml})) = 0, m = 1, ..., N. \tag{B.2}$$

Further if we write

$$U_{nl}(r) = \sum_{m=0}^{N-1} B_m^l(\kappa_{nl}) P_m^l(x_{nl}) \varphi_{ml}(r) \tag{B.3}$$

then apart from an overall normalisation constant we have $R_{nl} \propto U_{nl}$. Due to the non-orthogonality of the φ_{ml} it is not transparent that our required result for $f_{nl}(\kappa)$ given in Eq. (4.60) can be proven from the forms (B.1) to (B.3). Therefore we use information gathered thus far and apply it to the analytic expansion for the radial Coulomb wave in term of the orthogonal Laguerre function $\xi_{nl}(r)$. Stelbovics [136] showed that one may write

$$U_l(r) = \sum_{m=0}^{\infty} \overline{B}_m^l(\kappa) \overline{P}_m^l(x) \xi_{ml}(r) \tag{B.4}$$

where the $\overline{P}_m^l(x)$ are kernel Pollaczek polynomial and related in a straightforward way to the $P_m^l(x)$. Their form is given in [136] but is not required here. All that we have to note is that if we again truncate the basis set to $\xi_{m-l}, m = 0, 1, .., N-1$ we can write

$$U_{nl}(r) \propto \sum_{m=0}^{N-1} \overline{B}_m^l(\kappa_{nl}) \overline{P}_m^l(x_{nl}) \xi_{ml}(r) \tag{B.5}$$

where the ϵ_{nl} are still given by the solution of Eq. (B.2). The equivalence of the forms (B.3) to (B.5) is due to the fact that the same space is spanned by either of the sets of N Laguerre functions. Now the required result follows since from Eq. (4.60) we may write

$$f_{nl}(\kappa) \propto \frac{2\kappa^2}{\pi} \left| \sum_{m=0}^{N-1} \overline{B}_m^l(\kappa) \overline{P}_m^l(x) \overline{B}_m^l(\kappa_{nl}) \overline{P}_m^l(x_{nl}) \right|^2 \tag{B.6}$$

If we choose $\kappa = \kappa_{n'l} \neq \kappa_{nl}$ then we immediately have $f_{nl}(\kappa_{n'l}) = 0$, $n \neq n'$ from the orthogonality of the pseudo states U_{nl} expressed in the form (B.5).

Appendix C

Tabular data

Table C.1: Total ionization cross sections for antiproton collisions with atomic hydrogen in units of 10^{-16}cm^2 which are shown in Figs. 5.4 and 5.5, respectively. The present Born (calculated using the expansion method) and full results as well as the results of Bates and Griffing [12] are given for comparison.

Energy (keV)	Bates [12]	Present Born	Present full
1	0.01	0.01	1.11
2	0.08	0.08	1.24
3	0.23	0.21	1.29
5	0.61	0.58	1.35
10	1.46	1.41	1.39
20	2.11	2.06	1.39
30	2.15	2.10	1.35
40	2.03	1.99	1.29
60	1.73	1.69	1.18
100	1.27	1.25	0.98
200	0.77	0.75	0.66
300	0.55	0.54	0.50
400	0.44	0.42	0.40
500	0.36	0.35	0.34
600	0.31	0.30	0.29
800	0.24	0.23	0.23
1000	0.20	0.19	0.19

Table C.2: Present frozen-core (FC) and multiconfigurational (MC) results of total single ionization cross sections for antiproton-helium collisions in units of 10^{-16}cm^2 that are shown in Figs. 6.1 and 6.2, respectively.

Energy (keV)	FC	MC
1	0.1700	0.2567
1.2	0.1741	
1.5	0.1823	
2	0.1924	0.3009
3	0.2192	
5	0.2697	0.3991
10	0.3635	0.4751
20	0.4771	0.5651
30	0.5473	0.6261
50	0.6174	0.6756
70	0.6525	0.6764
100	0.6580	0.6502
150	0.6187	0.5791
200	0.5669	0.5137
300	0.4812	0.4221
500	0.3642	0.3158
700	0.2877	0.2494
1000	0.2162	0.1872

List of Figures

List of Tables

Bibliography

[1] E. Rutherford, Philos. Mag. **6**, 21 (1911).

[2] R. Ahlrichs, O. Dumbrajs, H. Pilkuhn, and H. G. Schlaile, Z. Phys. A **306**, 297 (1982).

[3] D. R. Schultz, P. S. Krstic, C. O. Reinhold, and J. C. Wells, Phys. Rev. Lett. **76**, 2882 (1996).

[4] T. Kirchner and H. Knudsen, J. Phys. B **44**, 122001 (2011).

[5] T. N. Rescigno, M. Baertschy, W. A. Isaacs, and C. W. McCurdy, Science **286**, 2474 (1999).

[6] M. Baertschy, T. N. Rescigno, and C. W. McCurdy, Phys. Rev. A **64**, 022709 (2001).

[7] I. Bray, Phys. Rev. Lett. **89**, 273201 (2002).

[8] J. S. Cohen, Phys. Rev. A **56**, 3583 (1997).

[9] K. Sakimoto, J. Phys. B **33**, 5165 (2000).

[10] K. Sakimoto, Phys. Rev. A **65**, 012706 (2001).

[11] D. R. Schultz, Phys. Rev. A **40**, 2330 (1989).

[12] D. R. Bates and G. W. Griffing, Proc. Phys. Soc. (London) **67**, 663 (1954).

[13] P. D. Fainstein, V. H. Ponce, and R. D. Rivarola, J. Phys. B **24**, 3091 (1991).

[14] D. S. F. Crothers and M. McCartney, Comp. Phys. Comm. **72**, 288 (1992).

[15] J. C. Wells, D. R. Schultz, P. Gavras, and M. S. Pindzola, Phys. Rev. A **54**, 593 (1996).

[16] X. Guan and K. Bartschat, Phys. Rev. Lett. **103**, 213201 (2009).

[17] G. Schiwietz, Phys. Rev. A **42**, 296 (1990).

[18] K. A. Hall, J. F. Reading, and A. L. Ford, J. Phys. B **29**, 6123 (1996).

[19] M. H. Martir, A. L. Ford, J. F. Reading, and R. L. Becker, J. Phys. B **15**, 1729 (1982).

[20] S. Sahoo, S. C. Mukherjee, and H. R. J. Walters, J. Phys. B **37**, 3227 (2004).

[21] J. Azuma, N. Toshima, K. Hino, and A. Igarashi, Phys. Rev. A **64**, 062704 (2001).

[22] N. Toshima, Phys. Rev. A **64**, 024701 (2001).

[23] B. Pons, Phys. Rev. Lett. **84**, 4569 (2000).

[24] M. McGovern, D. Assafrão, J. R. Mohallem, C. T. Whelan, and H. R. J. Walters, Phys. Rev. A **79**, 042707 (2009).

[25] A. Igarashi, S. Nakazaki, and A. Ohsaki, Phys. Rev. A **61**, 062712 (2000).

[26] H. Knudsen, U. Mikkelsen, K. Paludan, K. Kirsebom, S. P. Møller, E. Uggerhøj, J. Slevin, M. Charlton, and E. Morenzoni, Phys. Rev. Lett. **74**, 4627 (1995).

[27] L. Sarkadi, Phys. Rev. A **82**, 052710 (2010).

[28] A. C. Laforge, K. N. Egodapitiya, J. S. Alexander, A. Hasan, M. F. Ciappina, M. A. Khakoo, and M. Schulz, Phys. Rev. Lett. **103**, 053201 (2009).

[29] M. Schulz, A. C. Laforge, K. N. Egodapitiya, J. S. Alexander, A. Hasan, M. F. Ciappina, A. C. Roy, R. Dey, A. Samolov, and A. L. Godunov, Phys. Rev. A **81**, 052705 (2010).

[30] M. McGovern, D. Assafrão, J. R. Mohallem, C. T. Whelan, and H. R. J. Walters, Phys. Rev. A **81**, 032708 (2010).

[31] E. Y. Sidky and C. D. Lin, J. Phys. B **31**, 2949 (1998).

[32] B. Pons, Phys. Rev. A **63**, 012704 (2000).

[33] J. Berakdar, J. S. Briggs, and H. Klar, Z. Phys. D **24**, 351 (1992).

[34] A. B. Voitkiv and J. Ullrich, Phys. Rev. A **67**, 062703 (2003).

[35] S. Jones and D. H. Madison, Phys. Rev. A **65**, 052727 (2002).

[36] H. Knudsen, H.-P. E. Kristiansen, H. D. Thomsen, U. I. Uggerhøj, T. Ichioka, S. P. Møller, C. A. Hunniford, R. W. McCullough, M. Charlton, N. Kuroda, et al., Phys. Rev. Lett. **101**, 043201 (2008).

[37] L. H. Andersen, P. Hvelplund, H. Knudsen, S. P. Møller, J. O. P. Pedersen, S. Tang-Petersen, E. Uggerhøj, K. Elsener, and E. Morenzoni, Phys. Rev. A **41**, 6536 (1990).

[38] P. Hvelplund, H. Knudsen, U. Mikkelsen, E. Morenzoni, S. P. Møller, E. Uggerhøj, and T. Worm, Journal of Physics B: Atomic, Molecular and Optical Physics **27**, 925 (1994).

[39] K. Khayyat, T. Weber, R. Doorner, M. Achler, V. Mergel, L. Spielberger, O. Jagutzki, U. Meyer, J. Ullrich, R. Moshammer, et al., J. Phys. B **32**, L73 (1999).

[40] I. B. Abdurakhmanov, A. S. Kadyrov, I. Bray, and A. T. Stelbovics, J. Phys. B **44**, 075204 (2011).

[41] G. Schiwietz, U. Wille, R. D. Muio, P. D. Fainstein, and P. L. Grande, J. Phys. B **29**, 307 (1996).

[42] L. A. Wehrman, A. L. Ford, and J. F. Reading, J. Phys. B **29**, 5831 (1996).

[43] A. Igarashi, A. Ohsaki, and S. Nakazaki, Phys. Rev. A **62**, 052722 (2000).

[44] S. Sahoo, S. Mukherjee, and H. Walters, Nucl. Instr. and Meth. B **233**, 318 (2005).

[45] T. G. Lee, H. C. Tseng, and C. D. Lin, Phys. Rev. A **61**, 062713 (2000).

[46] F. Martin and A. Salin, Phys. Rev. A **54**, 3990 (1996).

[47] M. Foster, J. Colgan, and M. S. Pindzola, Phys. Rev. Lett. **100**, 033201 (2008).

[48] M. S. Pindzola, T. G. Lee, and J. Colgan, J. Phys. B **44**, 205204 (2011).

[49] A. Igarashi, A. Ohsaki, and S. Nakazaki, Phys. Rev. A **64**, 042717 (2001).

[50] J. S. Cohen, Phys. Rev. A **36**, 2024 (1987).

[51] R. E. Olson, K. H. Berkner, W. G. Graham, R. V. Pyle, A. S. Schlachter, and J. W. Stearns, Phys. Rev. Lett. **41**, 163 (1978).

[52] R. E. Olson and A. Salop, Phys. Rev. A **16**, 531 (1977).

[53] D. S. F. Crothers and J. F. McCain, J. Phys. B **16**, 3229 (1983).

[54] A. Igarashi and T. Shirai, Phys. Rev. A **50**, 4945 (1994).

[55] V. Maruhn-Rezwani, N. Grün, and W. Scheid, Phys. Rev. Lett. **43**, 512 (1979).

[56] K. C. Kulander, K. R. S. Devi, and S. E. Koonin, Phys. Rev. A **25**, 2968 (1982).

[57] C. Bottcher, Phys. Rev. Lett. **48**, 85 (1982).

[58] P. Gavras, M. S. Pindzola, D. R. Schultz, and J. C. Wells, Phys. Rev. A **52**, 3868 (1995).

[59] J. C. Wells, V. E. Oberacker, M. R. Strayer, and A. S. Umar, Phys. Rev. A **53**, 1498 (1996).

[60] K. Sakimoto, J. Phys. B **33**, 3149 (2000).

[61] J. C. Light, H. I. P., and L. J. V., J. Chem. Phys. **82**, 1400 (1984).

[62] L. Bacic and J. C. Light, J. Chem. Phys. **85**, 4594 (1986).

[63] D. T. Colbert and W. H. Miller, J. Chem. Phys. **96**, 1982 (1992).

[64] F. Aguillon, M. Sizun, V. Sidis, G. Billing, and N. Markovich, J. Chem. Phys. **104**, 4530 (1996).

[65] F. Aguillon and M. Sizun, J. Chem. Phys. **106**, 9551 (1997).

[66] K. Sakimoto, J. Chem. Phys. **63**, 419 (1981).

[67] K. Sakimoto, J. Chem. Phys. **236**, 123 (1998).

[68] K. Sakimoto, J. Chem. Phys. **110**, 11233 (1999).

[69] K. Sakimoto, J. Chem. Phys. **112**, 5044 (2000).

[70] K. Sakimoto, Phys. Rev. A **70**, 064501 (2004).

[71] B. H. Bransden and M. R. C. McDowell, *Charge Exchange and the Theory of Ion-Atom Collisions* (Clarendon, Oxford, 1992).

[72] A. L. Ford, J. F. Reading, and K. A. Hall, J. Phys. B **26**, 4537 (1993).

[73] A. S. Kadyrov and I. Bray, J. Phys. B **33**, L635 (2000).

[74] A. S. Kadyrov and I. Bray, Nucl. Instr. and Meth. B **171**, 119 (2000).

[75] A. S. Kadyrov and I. Bray, Phys. Rev. A **66**, 012710 (2002).

[76] R. Utamuratov, A. S. Kadyrov, D. V. Fursa, I. Bray, and A. T. Stelbovics, J. Phys. B **43**, 125203 (2010).

[77] I. Bray and A. T. Stelbovics, Phys. Rev. A **46**, 6995 (1992).

[78] S. G. Mikhlin, *Variational Methods in Mathematical Physics* (Pergamon, Oxford, 1964).

[79] I. H. Sloan and E. J. Moore, J. Phys. B (Proc. Phys. Soc.) **1**, 414 (1968).

[80] A. S. Kadyrov, A. M. Mukhamedzhanov, A. T. Stelbovics, I. Bray, and F. Pirlepesov, Phys. Rev. A **68**, 022703 (2003).

[81] L. Tomio and S. K. Adhikari, Phys. Rev. C **22**, 28 (1980).

[82] L. Tomio and S. K. Adhikari, Phys. Rev. C **24**, 43 (1981).

[83] S. K. Adhikari, Phys. Rev. C **19**, 1729 (1979).

[84] S. Tani, Phys. Rev. **139**, B1011 (1965).

[85] W. Glöckle, *The Quantum Mechanical Few-Body Problem* (Springer-Verlag, Berlin, 1983).

[86] I. Bray, D. V. Fursa, and A. T. Stelbovics, J. Phys. B **36**, 2211 (2003).

[87] D. V. Fursa, I. Bray, R. Panajotović, D. Šević, V.Pejčev, D. M. Filipović, and B. P. Marinković, Phys. Rev. A **72**, 012706 (2005).

[88] P. L. Bartlett, J. F. Williams, I. Bray, A. G. Mikosza, and A. T. Stelbovics, Phys. Rev. A **74**, 022714 (pages 7) (2006).

[89] D. V. Fursa and I. Bray, Phys. Rev. Lett. **100**, 113201 (2008).

[90] K. Bartschat, D. V. Fursa, and I. Bray, J. Phys. B **43**, 125202 (2010).

[91] K. Bartschat, A. S. Kheifets, D. V. Fursa, and I. Bray, J. Phys. B **43**, 165205 (2010).

[92] C. J. Bostock, D. V. Fursa, and I. Bray, Phys. Rev. A **82**, 022713 (2010).

[93] M. C. Zammit, D. V. Fursa, and I. Bray, Phys. Rev. A **82**, 052705 (2010).

[94] I. Bray and D. V. Fursa, J. Phys. B **44**, 061001 (2011).

[95] C. J. Bostock, D. V. Fursa, and I. Bray, Phys. Rev. A **83**, 052710 (2011).

[96] J. S. Savage, D. V. Fursa, and I. Bray, Phys. Rev. A **83**, 062709 (2011).

[97] C. J. Bostock, M. J. Berrington, D. V. Fursa, and I. Bray, Phys. Rev. Lett. **107**, 093202 (2011).

[98] B. Bransden and C. Joachain, *Physics of atoms and molecules*, Pearson Education (Prentice Hall, 2003).

[99] A. S. Kadyrov, I. Bray, A. T. Stelbovics, and B. Saha, J. Phys. B **38**, 509 (2005).

[100] A. S. Kadyrov, I. Bray, and A. T. Stelbovics, Phys. Rev. A **73**, 012710 (pages 5) (2006).

[101] A. S. Kadyrov, I. B. Abdurakhmanov, I. Bray, and A. T. Stelbovics, Phys. Rev. A **80**, 022704 (2009).

[102] I. B. Abdurakhmanov, A. S. Kadyrov, I. Bray, and A. T. Stelbovics, J. Phys. B **44**, 165203 (2011).

[103] I. Bray and A. T. Stelbovics, Phys. Rev. Lett. **70**, 746 (1993).

[104] J. R. Oppenheimer, Phys. Rev. **31**, 349 (1928).

[105] H. C. Brinkman and H. A. Kramers, Proc. Acad. Sci. Amsterdam **33**, 973 (1930).

[106] J. D. Jackson and H. Schiff, Phys. Rev. **89**, 359 (1953).

[107] G. V. Avakov, L. D. Blokhintsev, O. Dias, and A. M. Mukhamedzhanov, J. Phys. B **27**, 3067 (1994).

[108] J. H. Newman, J. D. Cogan, D. L. Ziegler, D. E. Nitz, R. D. Rundel, K. A. Smith, and R. F. Stebbings, Phys. Rev. A **25**, 2976 (1982).

[109] M. W. Gealy and B. Van Zyl, Phys. Rev. A **36**, 3091 (1987).

[110] G. W. McClure, Phys. Rev. **148**, 47 (1966).

[111] J. E. Bayfield, Phys. Rev. **185**, 105 (1969).

[112] A. B. Wittkower, G. Ryding, and H. B. Gilbody, Proc. Phys. Soc. (London) **89**, 541 (1966).

[113] P. Hvelpland and A. Andersen, Phys. Scr. **26**, 375 (1982).

[114] M. F. Ferreira da Silva and J. M. P. Serrão, J. Phys. B **36**, 2357 (2003).

[115] P. J. Martin, D. M. Blankenship, T. J. Kvale, E. Redd, J. L. Peacher, and J. T. Park, Phys. Rev. A **23**, 3357 (1981).

[116] D. Belkic, R. Gayet, and A. Salin, Phys. Rep. **56**, 279 (1979).

[117] R. Blankenbecler and M. L. Goldberger, Phys. Rev. **126**, 766 (1962).

[118] T. Adachi and T. Kotani, Prog. Theor. Phys. **39**, 430 (1968).

[119] T. Adachi and T. Kotani, Prog. Theor. Phys. **39**, 785 (1968).

[120] A. N. Kamal and L. K. Chavda, Phys. Rev. D **5**, 994 (1972).

[121] R. Utamuratov, A. S. Kadyrov, D. V. Fursa, and I. Bray, J. Phys. B **43**, 031001 (2010).

[122] D. V. Fursa and I. Bray, Phys. Rev. A **52**, 1279 (1995).

[123] G. V. Avakov, A. R. Ashurov, L. D. Blokhintsev, A. M. Mukhamedzhanov, and M. V. Poletayeva, J. Phys. B **23**, 2309S (1990).

[124] G. V. Avakov, A. R. Ashurov, L. D. Blokhintsev, A. S. Kadyrov, A. M. Mukhamedzhanov, and M. V. Poletayeva, J. Phys. B **23**, 4151 (1990).

[125] A. S. Kadyrov, I. B. Abdurakhmanov, R. Utamuratov, A. V. Lugovskoy, D. V. Fursa, I. Bray, and A. T. Stelbovics, J. Phys.: Conf. Series **262**, 012028 (2011).

[126] G. Drake and W. C. Martin, Can. J. Phys. **76**, 679 (1998).

[127] W. Lichten, D. Shiner, and Z.-X. Zhou, Phys. Rev. A **43**, 1663 (1991).

[128] D.-H. Yang, P. McNicholl, and H. Metcalf, Phys. Rev. A **33**, 1725 (1986).

[129] L. Hlousek, S. A. Lee, and W. M. Fairbank, Phys. Rev. Lett. **50**, 328 (1983).

[130] C. J. Sansonetti, J. D. Gillaspy, and C. L. Cromer, Phys. Rev. Lett. **65**, 2539 (1990).

[131] C. J. Sansonetti and J. D. Gillaspy, Phys. Rev. A **45**, R1 (1992).

[132] D. Shiner, R. Dixson, and P. Zhao, Phys. Rev. Lett. **72**, 1802 (1994).

[133] F. S. Pavone, F. Marin, P. De Natale, M. Inguscio, and F. Biraben, Phys. Rev. Lett. **73**, 42 (1994).

[134] C. Dorrer, F. Nez, B. de Beauvoir, L. Julien, and F. Biraben, Phys. Rev. Lett. **78**, 3658 (1997).

[135] D. A. Varshalovich, A. N. Moskalev, and V. K. Khersonskii, *Quantum theory of angular momentum* (World Scientific Pub., Philadelphia, 1988), 1st ed.

[136] A. T. Stelbovics, J. Phys. B **22**, L159 (1989).

[137] H. A. Yamani and W. P. Reinhardt, Phys. Rev. A **11**, 1144 (1975).

[138] A. S. Kadyrov, I. Bray, A. M. Mukhamedzhanov, and A. T. Stelbovics, Phys. Rev. Lett. **101**, 230405 (2008).

[139] C. R. Garibotti and J. E. Miraglia, Phys. Rev. A **21**, 572 (1980).

[140] E. O. Alt and A. M. Mukhamedzhanov, Phys. Rev. A **47**, 2004 (1993).

[141] A. M. Mukhamedzhanov, A. S. Kadyrov, and F. Pirlepesov, Phys. Rev. A **73**, 012713 (2006).

[142] I. Bray and D. V. Fursa, Phys. Rev. A **54**, 2991 (1996).

[143] A. S. Kadyrov, I. Bray, A. M. Mukhamedzhanov, and A. T. Stelbovics, Ann. Phys. **324**, 1516 (2009).

[144] P. L. Bartlett, I. Bray, S. Jones, A. T. Stelbovics, A. S. Kadyrov, K. Bartschat, G. ver Steeg, M. P. Scott, and P. G. Burke, Phys. Rev. A **68**, 020702(R) (2003).

[145] B. H. Bransden and A. T. Stelbovics, J. Phys. B **17**, 1877 (1984).

[146] H. Knudsen, J. Phys. Conference Series **194**, 012040 (2009).

[147] *Low-energy antiproton and ion research*, www.oeaw.ac.at/smi/FLAIR.

[148] *Facility for Antiproton and Ion Research*, www.gsi.de/FAIR.

[149] I. Bray, D. A. Konovalov, I. E. McCarthy, and A. T. Stelbovics, Phys. Rev. A **50**, R2818 (1994).

[150] A. B. Voitkiv (2011), private communication.

[151] C. P. Welsch, M. Grieser, A. Dorn, R. Moshammer, and J. Ullrich, AIP Conf. Proc. **796**, 266 (2005).

[152] P. D. Fainstein and V. D. Rodriguez, J. Phys. B **33**, 4637 (2000).

[153] E. Anderson, Z. Bai, C. Bischof, J. Demmel, J. Dongarra, J. D. Croz, A. Greenbaum, S. Hammarling, A. McKenney, S. Ostrouchov, et al., *LAPACK Users's guide* (Society for Industrial and Applied Mathematics, 1992).

[154] L. S. Blackford, J. Choi, A. Cleary, E. D'Azeuedo, J. Demmel, I. Dhillon, S. Hammarling, G. Henry, A. Petitet, K. Stanley, et al., *ScaLAPACK user's guide* (Society for Industrial and Applied Mathematics, 1997).